ABSTRACT

Geochemical Controls on Production in the Barnett Shale, Fort Worth Basin

Jana L. Klentzman, M.S.

Thesis Chairperson: Steve Dworkin, Ph.D.

The Newark East field (Barnett Shale) in the Fort Worth Basin, Texas currently has the largest daily production of any gas field in Texas. Major controls on production in the basin include: the quantity and character of organic matter, the thermal maturity history, and the mineralogy of the Barnett Shale. This study uses Rock Eval to investigate the quantity and character of the organic matter and general thermal maturity, vitrinite reflectance, $\delta^{13}C$ of produced methane and methane abundance to evaluate thermal maturity in more detail, and x-ray diffraction (XRD) to determine mineralogy. Based on these analyses, it is apparent that the best production from the Barnett Shale is typically found in maturation areas from 1.65 to 2.10%Ro with high organic carbon content, high quartz content, low calcite content and low dolomite content.

Geochemical Controls on Production in the Barnett Shale, Fort Worth Basin

by

Jana L. Klentzman, B.S.

A Thesis

Approved by the Department of Geology

_____

Steven G. Driese, Ph.D., Chairperson

Submitted to the Graduate Faculty of
Baylor University in Partial Fulfillment of the
Requirements for the Degree
of
Master of Science

Approved by the Thesis Committee

_____

Stephen I. Dworkin, Ph.D., Chairperson

_____

Stacy C. Atchley, Ph.D.

_____

C. Kevin Chambliss, Ph.D.

Accepted by the Graduate School
August 2009

_____

J. Larry Lyon, Ph.D., Dean

Page bearing signatures is kept on file in the Graduate School.

TABLE OF CONTENTS

LIST OF FIGURES

LIST OF TABLES

ACKNOWLEDGMENTS

This study was sponsored by EnCana Corporation and greatly benefited from the use of Baylor Universities XRD Laboratory and the Applied Petroleum Studies Laboratory. I want to thank Dr. Dworkin for providing me the incredible opportunity to complete my masters education at Baylor as one of his students and also Josh Talbert without whom the project would not have been possible. I also want to thank Josh Talbert, Dr. Mark Tobey and Natalie Givens of EnCana Corporation for their teachings and guidance throughout the course of this project. I owe so much of this to my family whose encouragement and financial and emotional support made this process much more enjoyable.

CHAPTER ONE

Introduction

The Fort Worth Basin of north-central Texas (Figure 1A) has been producing hydrocarbons since the early 1900s. Within the Fort Worth Basin, the Barnett Shale was recognized as the source rock for overlying Ordovician to Permian conventional reservoirs (Ball and Perry, 2006; Pollastro et al., 2007) prior to the 1980's. After the successful application of water fractures (a combination of water, friction reducer, bactericide, scale inhibitor, and low sand concentration) and the discovery that true gas in place is nearly four times what was previously believed, the Barnett Shale became a major target for unconventional natural gas production (Bowker, 2007). An unconventional, continuous petroleum system is defined as an accumulation of hydrocarbons found in low-permeability rocks that depend on fracture permeability, either natural or as a result of completion practices, for production. Unconventional reservoirs contain large amounts of hydrocarbons but have low gas recovery factors (Schmoker, 1995 in Jarvie et al., 2007). Unconventional shale gas has become an important resource for many countries and accounted for more than 14% of produced gas in the United States by the end of 2004 (Energy Information Administration, 2006 in Jarvie et al., 2007). The estimated total mean volume of undiscovered recoverable

gas within the Fort Worth Basin is about 26 tcf in two Barnett Shale gas assessment units (Pollastro et al., 2004 and 2007).

This study focuses on petrologic and geochemical aspects of the Barnett Shale and how they influence production. Specifically the abundance and character of organic matter (measured using Rock Eval), the thermal maturity history (derived from Hydrogen Index, vitrinite reflectance data, $\delta^{13}C$ of produced methane data and methane abundance data), and the mineralogy (quantified using x-ray diffraction) are used to investigate controls on production. The major objectives of this study are to: 1) locate areas of high total organic carbon, 2) build a thermal maturity map of the basin, 3) find the optimal maturity range for hydrocarbon production, 4) map the distribution of mineral abundance within the basin that influence production and 5) determine the geographic area(s) of optimal exploration potential.

Geologic Setting and Stratigraphy

During the Paleozoic Ouachita orogeny, Barnett Shale strata were deposited in a narrow inland seaway on the leading southern edge of the Oklahoma aulacogen Figure 1A). This took place on the Laurasian paleocontinent during collision with Gondwana (Walper, 1982 and Thompson, 1988 in Montgomery et al., 2005; Loucks and Ruppel, 2007). The Fort Worth basin axis trends roughly parallel to the Ouachita structural front that bounds the basin to the east (Montgomery et al., 2005). The Barnett Shale is bound to the north by the Red River Arch, to the northeast by the

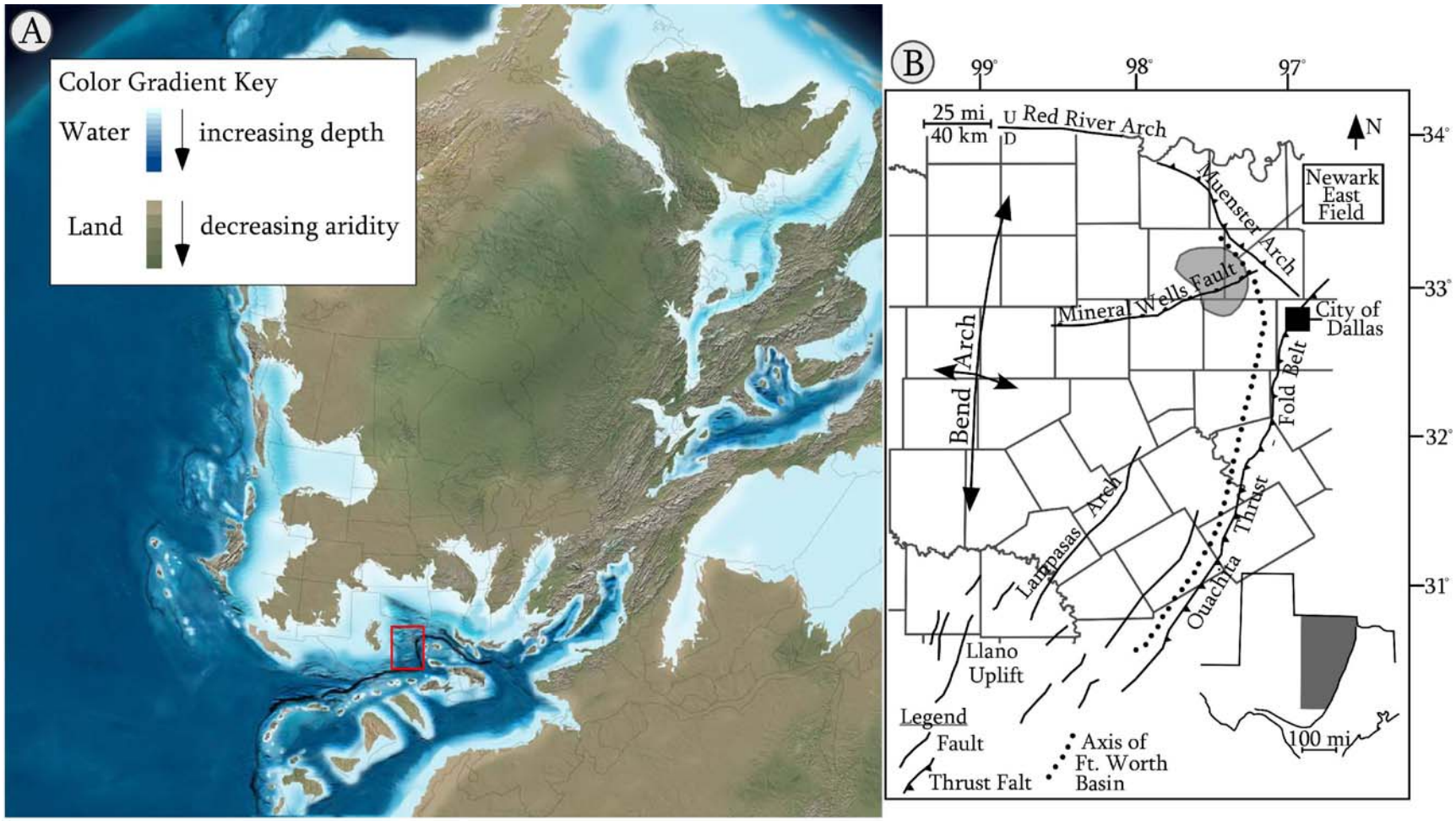

Figure 1. A. Paleogeography during Barnett Shale deposition (Blakey,2006); red box outlines the Fort Worth Basin. B) Fort Worth Basin with major present day structural features shown (Montgomery et al, 2005)

Muenster arch, to the south by the Llano uplift and Lampasas arch, and by the Bend arch to the west (Figure 1B).

Figure 2 is a generalized stratigraphic column of the Fort Worth Basin (Zhao et al., 2007). The Mississippian Barnett Shale unconformably overlies the Ordovician Ellenberger and Viola formations. Viola Formation limestone provides a basal seal that isolates the Barnett Shale from the underlying water-bearing Ellenberger Formation (Marble 2004, 2006 in Jarvie et al., 2007). West of the Viola Limestone erosional limit, where Barnett Shale strata lie directly above the Ellenberger Formation, wells can be successfully completed. However if the well is perforated too close to the Ellenberger Formation contact, the well will produce saline water. To the west and southwest of the basin margins, shallow carbonates of the early Mississippian Chappel Formation separate the Barnett Shale from the underlying Ellenberger Formation (Loucks and Ruppel, 2007). The Barnett Shale is conformably overlain by the Pennsylvanian Marble Falls Limestone. Due to erosion the Barnett Shale is absent over the Muenster arch, a Pennsylvanian horst block.

Accommodation within the interior seaway was probably the result of both eustatic sea level rise and crustal downwarping associated with the Ouachita orogeny (Loucks and Ruppel, 2007). The sediment accumulated between water depths of 600 feet to greater than 1000 feet below both storm wave base and the oxygen minimum zone (Gutshick and Sandberg, 1983 in Loucks and Ruppel, 2007). The Barnett Shale is

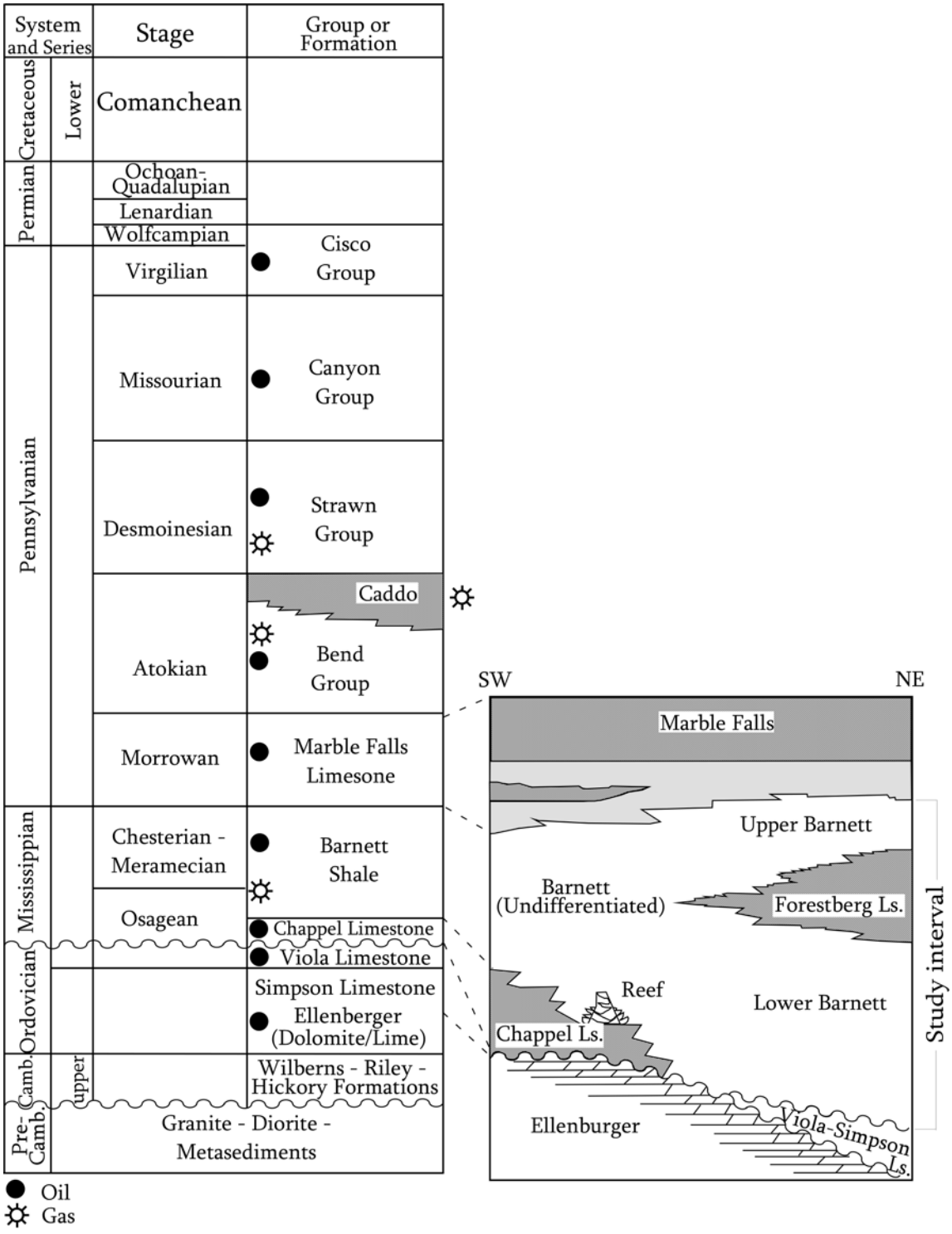

Figure 2: Generalized stratigraphic column of the Fort Worth Basin showing the types of hydrocarbons produced (modified from Zhao et al., 2007).

believed to have been deposited during a second-order sea-level highstand (Osagean to Chesterian, 320-345 Ma) (Ross and Ross, 1987 in Loucks and Ruppel, 2007). Interbedded carbonates within the Barnett Shale are interpreted as hemipelagic plumes or density flows sourced from the coeval Chappel Limestone shelf (Bowker, 2007). The main source area contributing siliciclastics to the Barnett Shale was the Caballos Arkansas island chain to the south. Silt-sized or smaller sediment composed of quartz, feldspars and clay minerals were transported as plumes or density flows into the basin; however the main source of quartz is radiolarian tests and other siliceous skeletal material (Loucks and Ruppel, 2007). The Barnett Shale is a subtly heterogeneous mudrock that has been divided in to five lithofacies: 1) black shale, 2) lime grainstone, 3) calcareous black shale, 4) dolomitic black shale, and 5) phosphatic black shale (Henk et al., 2000; Henk, 2005; Hickey and Henk, 2006; all in Jarvie et al., 2007; Loucks and Ruppel, 2007). All lithofacies yield gamma-ray response greater than 100 API. The highest gamma ray activity is associated with the phosphatic black shale and is most likely due to high thorium content (Gas Research Institute, 1991).

The Barnett Shale is greater than 1000 feet thick near the Muenster arch and less than 50 feet thick where the Barnett Shale thins over the Bend Arch (Zhao et al., 2007; Hill et al., 2007). The Barnett Shale is commonly subdivided into two layers (termed the upper Barnett and the lower Barnett) in the eastern part of the basin where the Forestberg Limestone is present. The upper Barnett is commonly 60 to 70 feet thick when it is differentiated from the lower Barnett.

High heat flow, related to Ouachita thrusting and faulting, has heavily influenced the overall thermal maturity of the Fort Worth basin (Pollastro et al., 2003). Different burial histories in various parts of the basin also play a major role in influencing the thermal maturity and consequently the gas and oil production of the Barnett Shale (Bowker, 2002, 2003 in Montgomery et al., 2007). Two burial history curves for the northern and the southern parts of the basin, demonstrate the regional differences between burial and uplift history that have caused the southern portion of the Barnett Shale to be much more thermally mature than the northern portion (Figure 3) (Jarvie, 2004). A thorough understanding of the thermal maturity of the basin is essential to understanding gas production from the Barnett Shale because the gas is primarily thermogenic in origin. This is apparently why the northern portion of the basin produces both oil and gas where as the southern portion of the basin is known to only produce gas.

Methods

The Barnett Shale was subdivided lithologically into eight zones by abrupt gamma ray excursoins that are regionally correlatable (Figure 4) (provided by EnCana Corporation circa June 2008). These zones have been identified by EnCana geoscientists familiar with log characteristics of the Barnett Shale. Cuttings samples from the top of each zone were analyzed for their organic matter abundance and mineralogy. A smaller subset of these samples was analyzed for vitrinite reflectance.

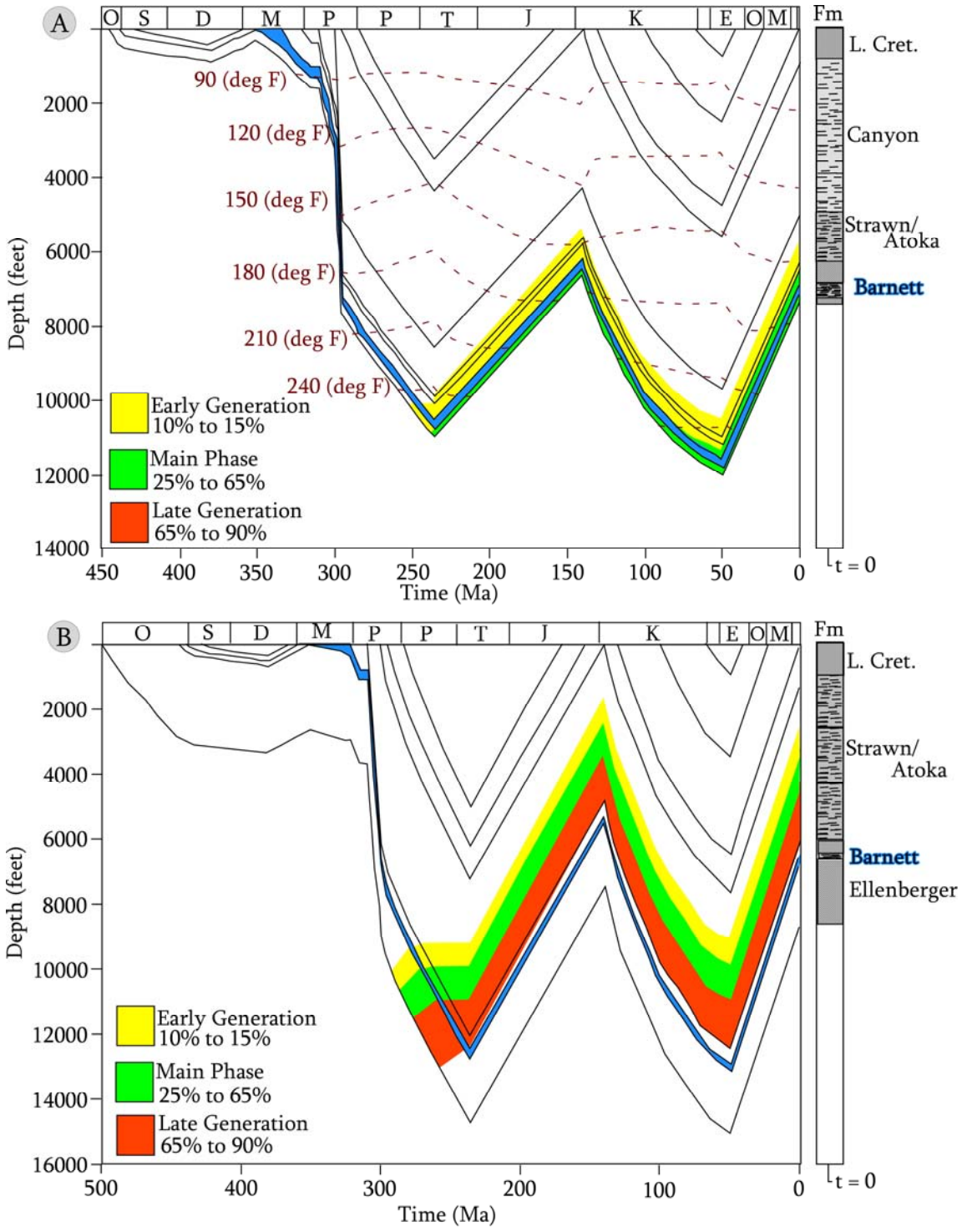

Figure 3: Barnett burial history maps (Jarvie, 2004): A) northern Barnett Shale burial history, B) southern Barnett Shale burial history. Note the deepest depth the northern Barnett Shale was buried, was approximately -11,000 feet whereas the southern portion of the Barnett Shale wsa buried to approximately -13,000 feet.

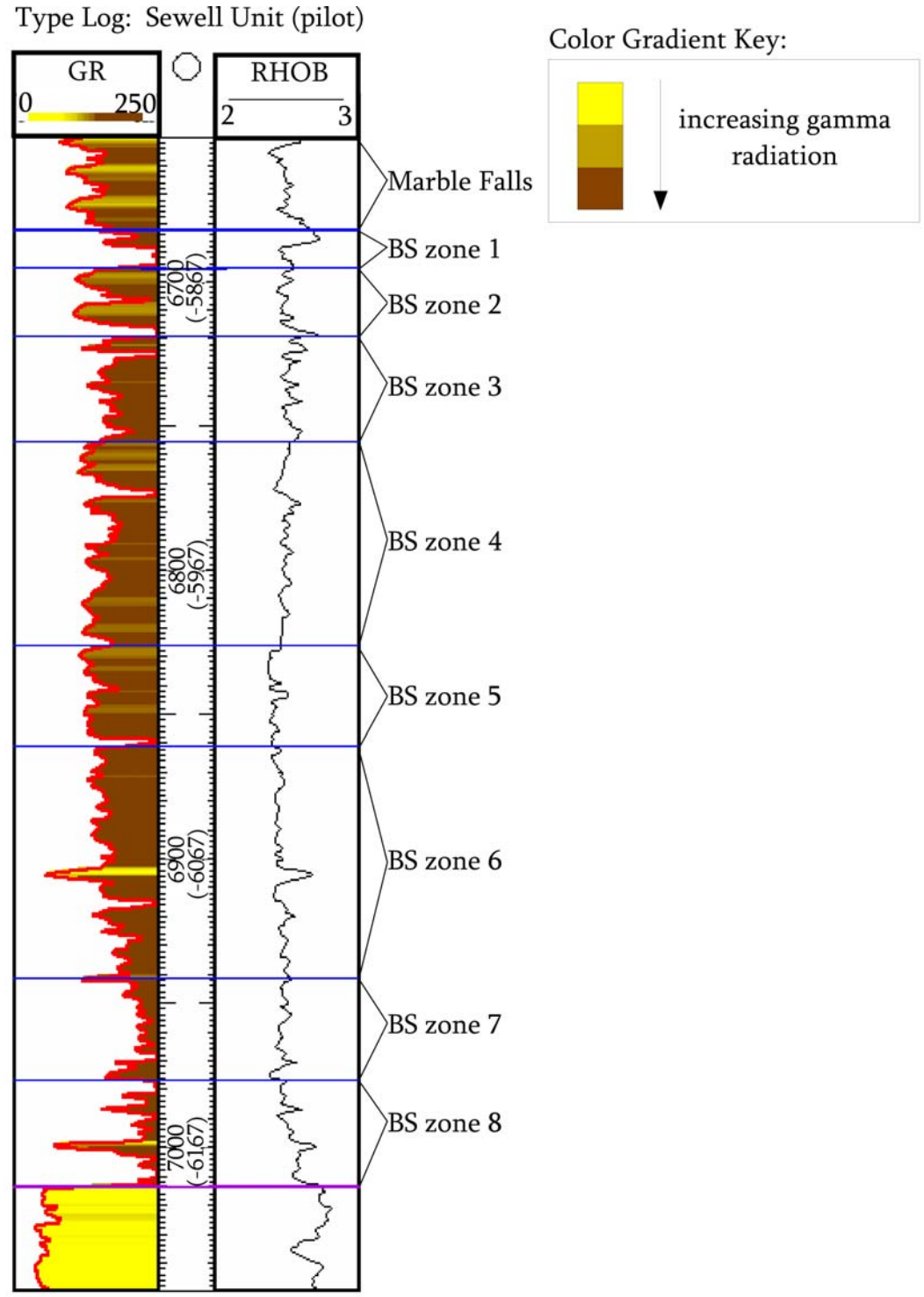

Figure 4: Barnett Shale type log. This figure demonstrates the regionally correlatable gamma ray excursions that are used to identify zones 1 through 8 in the Barnett Shale.

Organic Matter Abundance and Character

232 samples of cuttings from 44 EnCana wells were analyzed for the abundance and character of organic matter by Humble Geochemical Services using Rock Eval pyrolysis. Rock Eval is an open system programmed pyrolysis technique in which the bulk pyrolysis products are quantified (Tobey, 2007) (Table 1) (Figure 5). Because the Barnett Shale is over mature in most areas of the basin, many of the parameters produced by Rock Eval are not useful or interpretable. However, Total Organic Carbon (TOC) concentrations and the Hydrogen Index (HI; S2/TOC) did prove to be useful. TOC data is used to find the most organic rich areas and to identify areas of high secondary porosity that form within the remaining organic matter. HI data can be used to identify the general thermal maturity of the study area rather than its usual use of identifying the kerogen type. HI data is not useful as a kerogen type indicator because the basin is over mature in many regions and this causes the S2 peak (Figure 5) to become very small or non-existent because there is little or no residual kerogen to yield hydrocarbons (Tobey, 2007). However, because the kerogen type in the Barnett Shale has been determined to be Type II throughout the basin (and would normally have HI values ranging from 300-600), the HI data can instead be used to interpret thermal maturity (Jarvie, 2004, Hill et al., 2007; personal communication with Mark Tobey, 2008) (Table 2). This is because as an area becomes more thermally mature, hydrocarbons are produced until there is no remaining generative potential in the organic matter. Because the S2 peak records the residual

Table 1: Rock Eval pyrolysis products and their descriptions (Tobey, 2007).

	Pyrolysis Products	Description		Limitations
1)	S1	free oil and gas in the rock		sample contamination due to drilling processes
2)	S2	amount of hydrocarbon the residual kerogen can yield		NA for dry gas mature and post mature source rocks
	Residual hydrocarbon (HC) generative potential based on S2:			
	S2 = 0.0-2.5		poor HC generative potential	
	S2 = 2.5-5.0		fair HC generative potential	
	S2 = 5.0-10.0		good HC generative potential	
	S2 = 10.0-20.0		very good HC generative potential	
	S2 > 20.0		excellent HC generative potential	
3)	S3	the oxygen content of the kerogen		can be misleading if instrument not regularly calibrated
4)	S4	the dead (will not convert to HC) organic carbon in rock		
5)	Tmax	the temperature at which S2 is greatest		NA for dry gas mature and post mature source rocks
	Thermal maturity guidelines based on Tmax:			
	Tmax < 435	0.20 - 0.60 Ro (%)	immature	
	Tmax 435 - 445	0.60 - 0.65 Ro (%)	early oil-mature	
	Tmax 445 - 450	0.65 - 0.90 Ro (%)	peak oil-mature	
	Tmax 450 - 470	0.90 - 1.35 Ro (%)	late oil/wet gas mature	
	Tmax > 470	> 1.35 Ro (%)	dry gas mature	
6)	TOC	total organic carbon calculated from the Rock Eval process		
	Source rock potential based on TOC:			
	TOC = 0.00 - 0.50 wt %:		poor source potential	
	TOC = 0.50 - 1.00 wt %:		fair source potential	
	TOC = 1.00 - 2.00 wt %:		good source potential	
	TOC = 2.00 - 4.00 wt %:		very good source potential	
	TOC > 4.00 wt %:		excellent source potential	
7)	Oil Index	100x(S1/TOC); oil mature rocks yield a large S1 peak		if oil index exceeds 100 contamination may be an issue
8)	Hydrogen Index	100x(S2/TOC); Residual kerogen type		NA for dry gas mature and post mature source rocks
	Residual kerogen type based on Hydrogen Index (HI):			
	HI > 600	Type I Kerogen	oil-prone	
	HI 300 - 600	Type II Kerogen	oil-prone	
	HI 200 - 300	Type II/III Kerogen	mixed oil and gas prone	
	HI 50 - 200	Type III Kerogen	gas prone	
	HI < 50	Type IV Kerogen	no generative potential	
9)	Oxygen Index	100x(S3/TOC); assess residual kerogen type		S2 is a more reliable tool for this assessment
10)	Production Index	S1/(S1+S2); a ballpark maturation indicator		NA for dry gas mature and post mature source rocks

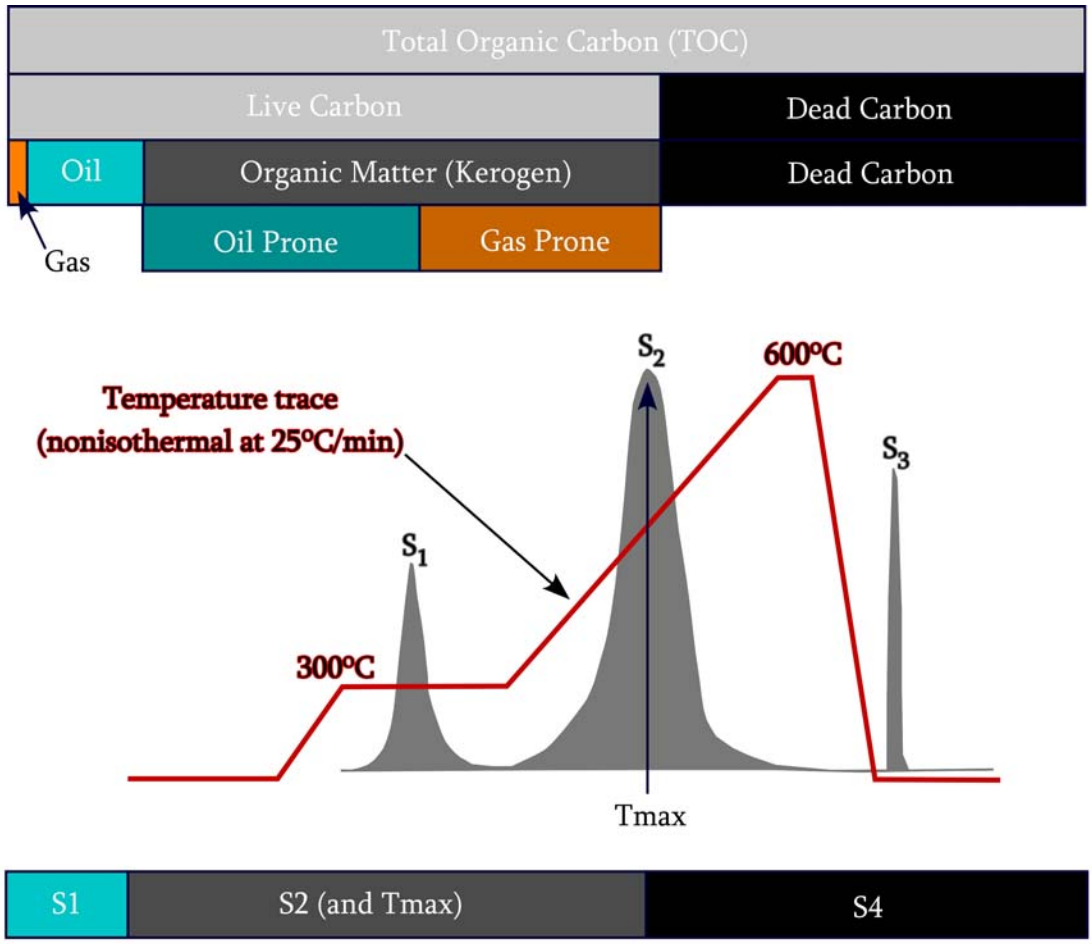

Figure 5: Rock Eval diagram after Jarvie, 2004. The S1 peak is a measure of the oil and gas present with in the rock sample. The S2 peak is a measure of the remaining kerogen that is converted to hydrocarbons during higher temperatures of the pyrolysis process. The S3 peak is a measure of CO_2 that occurs during pyrolysis.

Table 2: Kerogen types and their descriptions (Tobey, 2007).

Kerogen Type	Definition	Contents	Elemental Ratios	Production Potential
Type I Kerogen	lacustrine oil prone source rocks	amorphous organic matter, alginite, cyanobacteria, freshwater algae and land plant remains	H/C > 1.25 O/C < 0.15	mainly oil, some gas
Type II Kerogen	marine oil prone source rocks	marine algae and terrestrial plant material; exinite, cutinite, resinite, liptinite	H/C < 1.25 O/C = 0.03 to 0.18	produces gas and oil
Type III Kerogen	gas prone source rocks	terrestrial plant matter; cellulose, lignin, terpenes, and phenolic	H/C < 1.00 O/C = 0.03 to 0.3	produces methane gas or coal
Type IV Kerogen	residue, no production potential	decomposed orgainc matter in the form of polycyclic aromatic hydrocarbons	H/C < 0.5	NA

hydrocarbon generative potential of a sample, it can be used as a thermal maturity indicator for an over mature source rock. Therefore, the most mature areas correspond to small HI values (due to small S2 peaks) and the least mature areas correspond to large HI values (due to large S2 peaks).

Vitrinite Reflectance

128 samples of cuttings from 21 wells were analyzed by Dr. Charles Landis for thermal maturity using vitrinite reflectance analysis. Vitrinite reflectance is a measure of the percentage of light reflected from the vitrinite maceral and is reported as Ro (%) units. Though the measurement of vitrinite reflectance is objective, the selection of what to measure it on (the autochthonous vitrinite) is subjective and dependent upon the experience of the organic petrographer. All samples include both recycled vitrinite and autochthonous vitrinite; taking multiple samples in one well (a profile) allows the organic petrographer to more easily identify the autochthonous vitrinite for measurement (Tobey, 2007). Vitrinite reflectance is a measure of integrated time-temperature history.

Ten "spot checks" (that consist of 4 depth varied samples from a single well), and 11 "profiles" (that consist of 8 depth varied samples from a single well) were conducted. Cutting samples for vitrinite reflectance were chosen to span a large depth range and a wide spacial distribution in order to asses the different thermal maturities throughout the basin. The whole rock method was used so that the

organic matter could be observed in the rock which aids in the identification of the autochthonous vitrinite population (Senftle and Landis, 1991).

$\delta^{13}C$ of Produced Methane

The carbon isotopic composition of 259 samples of methane gas produced from Barnett Shale wells was analyzed by Geomark laboratories or in the field by Pencor. This data set is supplemented by analyses from the study of Hill et al. (2007). The reported precision of all analyses is better than 0.1‰.

Mineralogy

The presence and abundance of minerals in the Barnett Shale was determined for 232 samples of shale cuttings from 44 EnCana wells. Cutting samples were washed in deionized water, cleaned of extraneous drilling material and ground to a fine powder using a SFM-1 Desk-Top Planetary Ball Mill. Random powder mounts were then made and analyzed at Baylor University using a Seimens 5000 x-ray diffractometer (Klug et. al. 1974).

In order to evaluate the XRD results in terms of mineral abundance, calibration curves were constructed for the minerals of interest. This is based on the principle that the height or area of a diffraction peak is proportional to the abundance of the mineral that produced the peak (Pecharsky and Zavalij, 2005). Therefore, for each mineral of interest, the peak area of a characteristic peak was measured using Jade software (Figure 6).

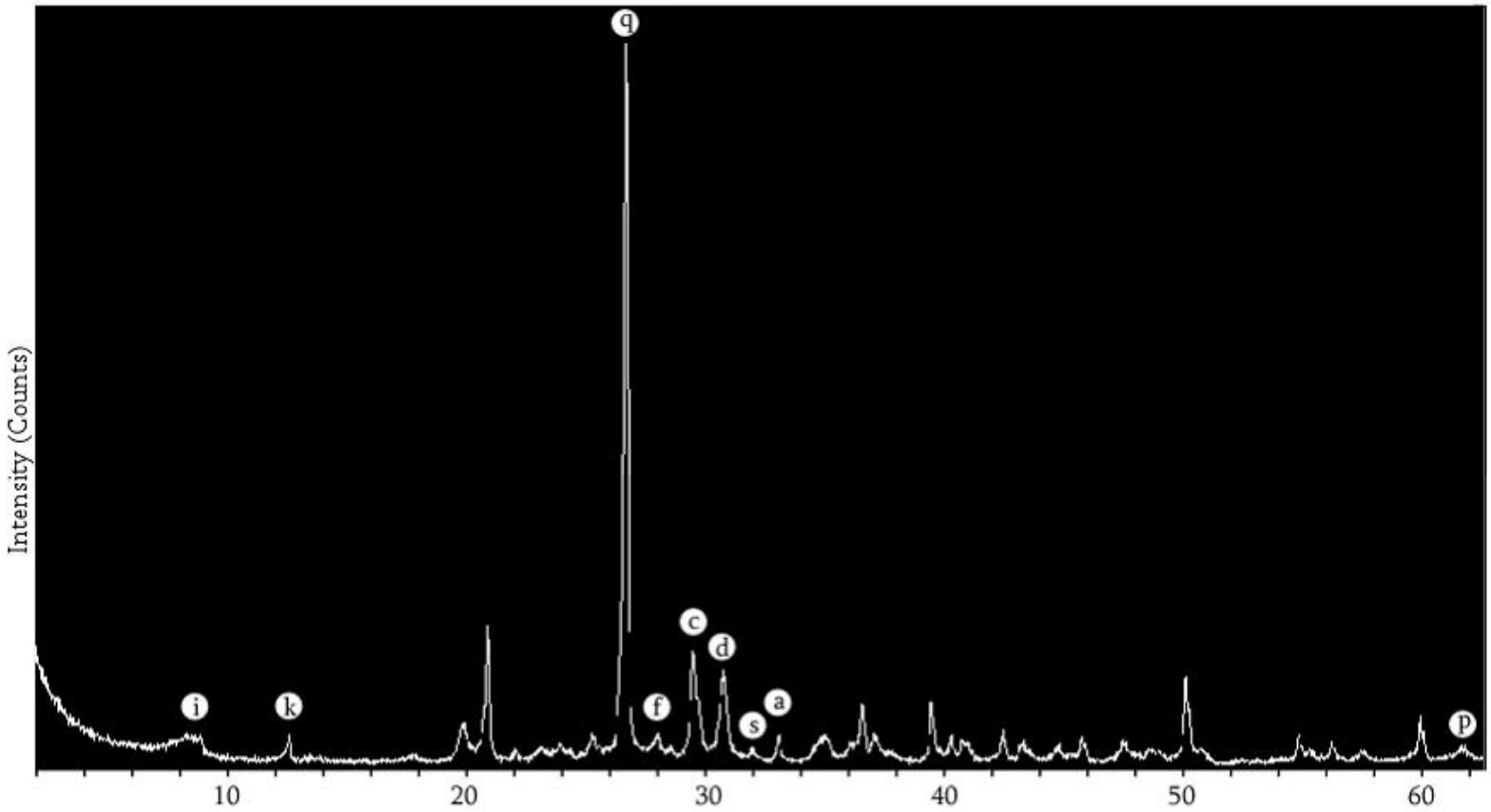

Figure 6: XRD diffractogram for sample J36-1 showing characteristic peaks used in this study. From left to right: i) illite, 2 theta = 9.07, d-spacing = 9.7; k) kaolinite, 2 theta = 12.6, d-spacing = 7.01; q) quartz, 2 theta = 26.7, d-spacing = 3.33; f) plagioclase feldspar, 2 theta = 27.9, d-spacing = 3.18; c) calcite, 2 theta = 29.5, d-spacing = 3.01; d) dolomite, 2 theta = 31.03, d-spacing = 2.88; s) siderite, 2 theta = 32.16, d-spacing = 2.79;a) apatite, 2 theta = 33.1, d-spacing = 2.7; p) pyrite, 2 theta = 56.4, d-spacing = 1.62.

XRD calibration curves were constructed by preparing 22 rock powders that contained varying proportions of the following minerals: apatite, calcite, dolomite, plagioclase feldspar, pyrite, quartz, siderite, illite, smectite and kaolinite (Appendix A). Each of these powders was x-rayed five times and the area of the primary peak for each of the nine minerals of interest was averaged. The averaged peak areas were then used to create calibration curves (figures 7-9) that compare peak area to mineral abundance. The calibration curves were then used to calculate the abundance of each mineral following a normalization of the data. The precision of XRD analysis is usually better than 5% (Table 3) based on replicate analyses (n=5) of the in house standards. Plagioclase, siderite and kaolinite often have poorer precision because of their very abundance (less than 2% mineral abundance). It appears that precision decays rapidly when mineral abundance is less than 2 weight %.

The calibration curves worked well for all minerals except apatite. Apatite values produced from the calibration curves were anomalously high (when comparing to published data), approximately 10% on average. The Barnett Shale commonly has an average apatite abundance of 3.3% (Loucks and Ruppel, 2007). It is believed that the overestimation of apatite was most likely caused by another material being introduced into the wellbore during the drilling process as the in house standards did not exhibit this problem. As a result, apatite was not quantified and mineral abundances have been normalized without apatite.

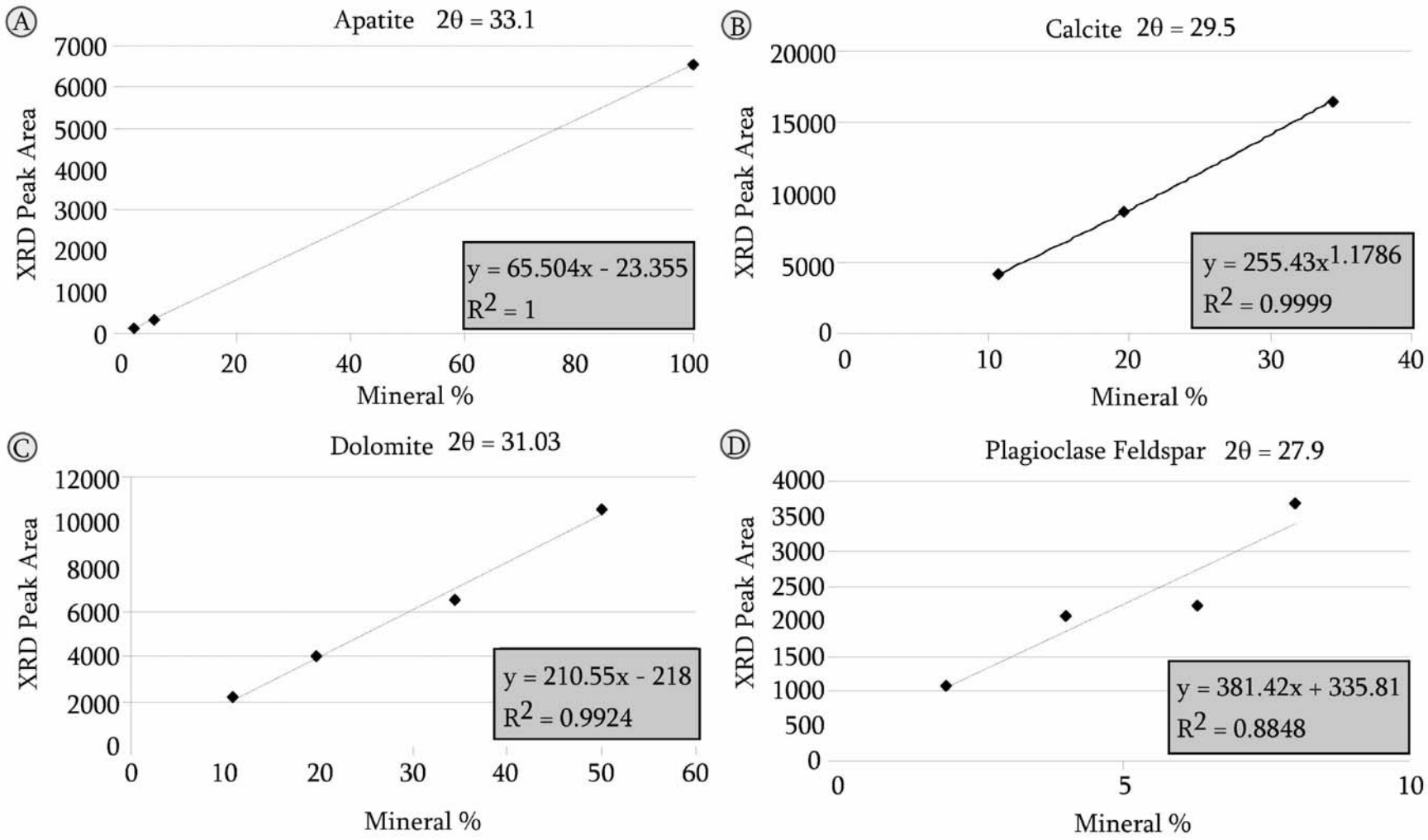

Figure 7: XRD calibration curves. A) apatite, B) calcite, C) dolomite, D) plagioclase feldspar.

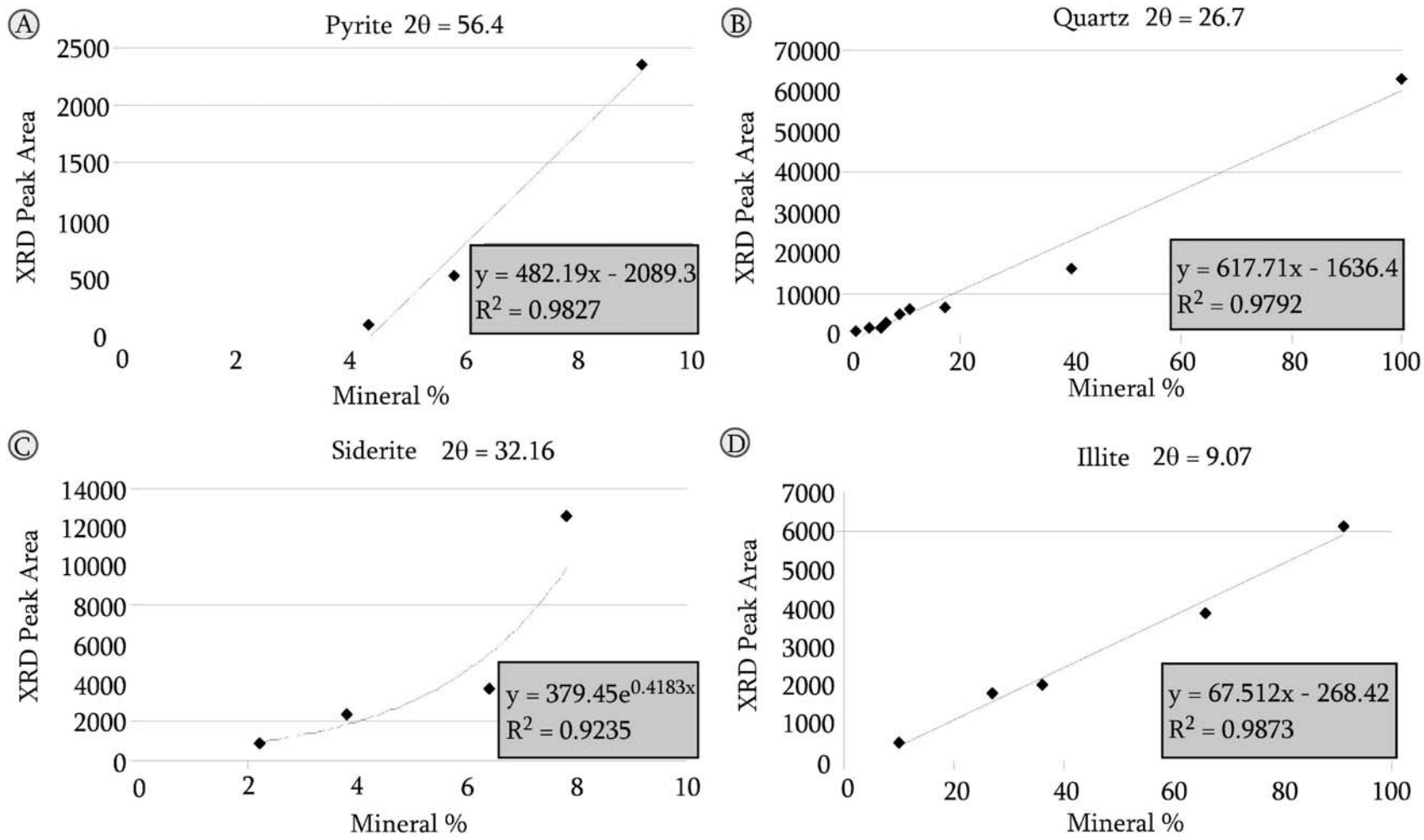

Figure 8: XRD calibration curves. A) pyrite, B) quartz, C) siderite, D) illite.

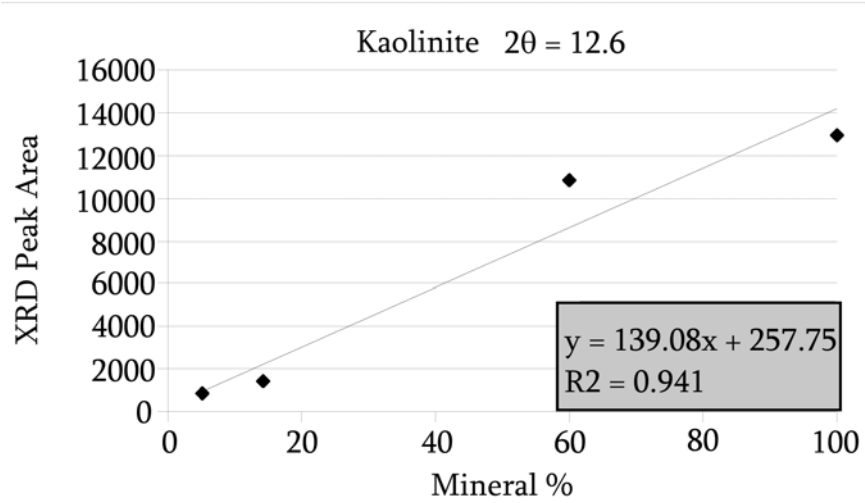

Figure 9: Kaolinite XRD calibration curve.

Table 3: The relative standard deviation for each mineral (after mineral % was calculated using calibration curves) within a randomly chosen sample and standard.

Mineral	Sample J17-1	Standard J2
Apatite	0.1	4.8
Calcite	0.1	0.8
Dolomite	5.6	2.2
Plagioclase	15.1	2.5
Pyrite	0.3	2.6
Quartz	1.9	0.8
Siderite	105.5	3.3
Illite	3.7	5.4
Kaolinite	484.6	4.5

Map Building

All data were uploaded into PETRA® version 3.1.9.1, which is a geological interpretation software program, in order to build contour maps that incorporate production data for every relevant geochemical parameter in the study.

CHAPTER TWO

Organic Carbon Content of the Barnett Shale

Results

Total organic carbon (TOC) abundance in the Barnett Shale is important for two reasons: 1) it is the source of hydrocarbons and thus areas of high TOC are likely to be more productive, and 2) methane can be adsorbed into the remaining organic matter within micropores that develop during diagenesis. Thus organic matter in the Barnett Shale both creates and stores hydrocarbons.

TOC values within the Barnett range between 0.36 to 9.66% and average about 3.1% (Appendix B). The amount of organic matter present before thermal maturation can be calculated using the Barnett Shale Model© (TOCp/0.64 = TOCo; p = present, o = original) (Jarvie, 2004). From this equation, the original organic carbon content of the Barnett Shale ranges from 1.0 to 15.1% and averaged about 4.8%.

Like many unconventional reservoirs, the Barnett Shale has little primary porosity. Porosity ranges from 3.8 to 6% (Hill et al., 2007; Jarvie et al., 2007; Zhao et al., 2007). The only significant secondary porosity in the Barnett Shale is by methane adsorption to the remaining organic matter and clay surfaces (Gas Research Iinstitute, 1991). Within the Barnett Shale, the amount of hydrocarbons stored by adsorption to

the remaining organic matter may account for up to 45% of the total gas in place (GIP) in the Mitchell 2 T.P. Sims well (Hill et al., 2007).

Distribution of TOC in the Barnett Shale zones

TOC distribution in the eight stratigraphic zones of the Barnett Shale (refer to type log Figure 4) varies little (Figure 10). However, zone 7 has the highest average TOC values at 3.8%. Unfortunately, Zone 7 is never intentionally produced from because it is heavily cemented with apatite and therefore does not artificially fracture well during stimulation. The inability of zone 7 to fracture when stimulated reduces the surface area available to produce hydrocarbons. This zone does, however, serve as a fracture barrier between the Barnett Shale's stratigraphically younger zones and the water bearing Ellenberger. Zone 4 has the second highest average organic carbon at 3.4%. Zones 2, 3, 5, 6 and 8 do not differ much and have average TOC values between 3.0 and 3.2%. Zone 1 has the lowest average organic carbon value at 2.5%.

Spatial Distribution of TOC

Figures 11 and 12 are contour maps of the abundance of organic carbon in each zone of the Barnett Shale. These maps show the spatial distribution of the abundance of organic carbon in the subsurface; each sample location represents one sample collected from the top 10 feet of cuttings from the mapped zone. All maps show that the highest concentration of organic matter in the Barnett Shale is located

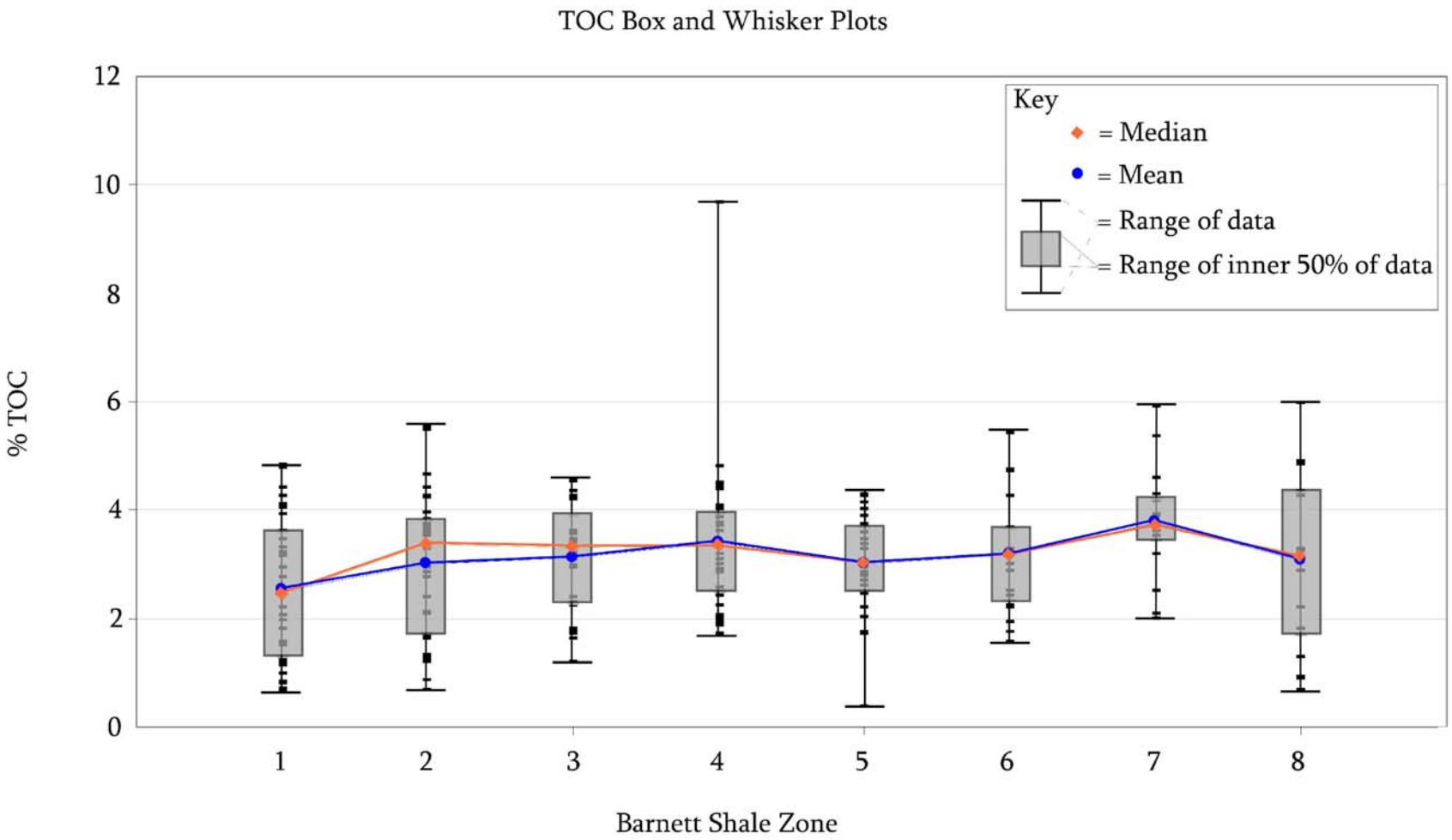

Figure 10: Total Organic Carbon Box and Whisker Plots.

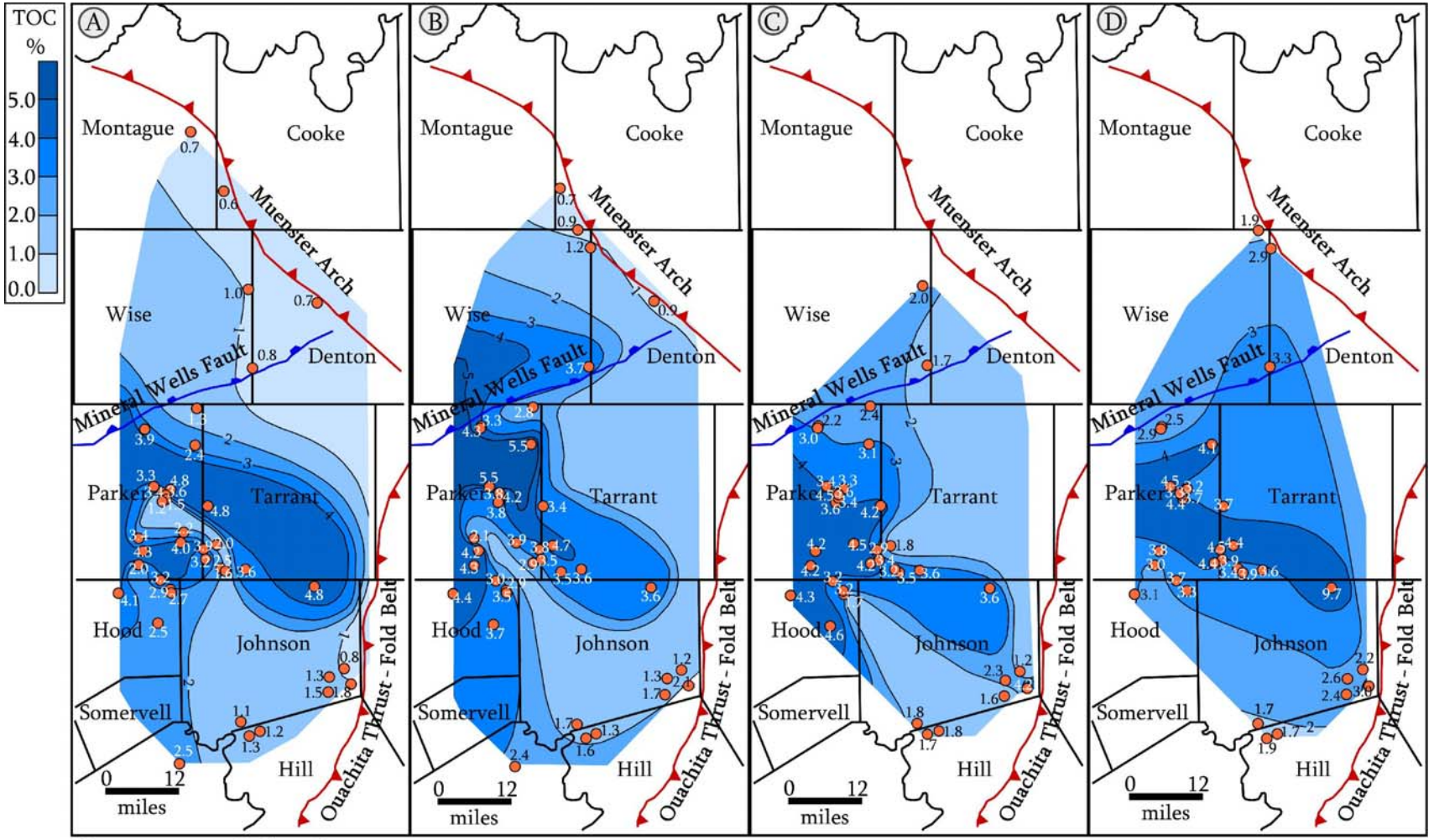

Figure 11: TOC content maps. A) Barnett Shale zone 1, B) Barnett Shale zone 2, C) Barnett Shale zone 3, D) Barnett Shale zone 4.

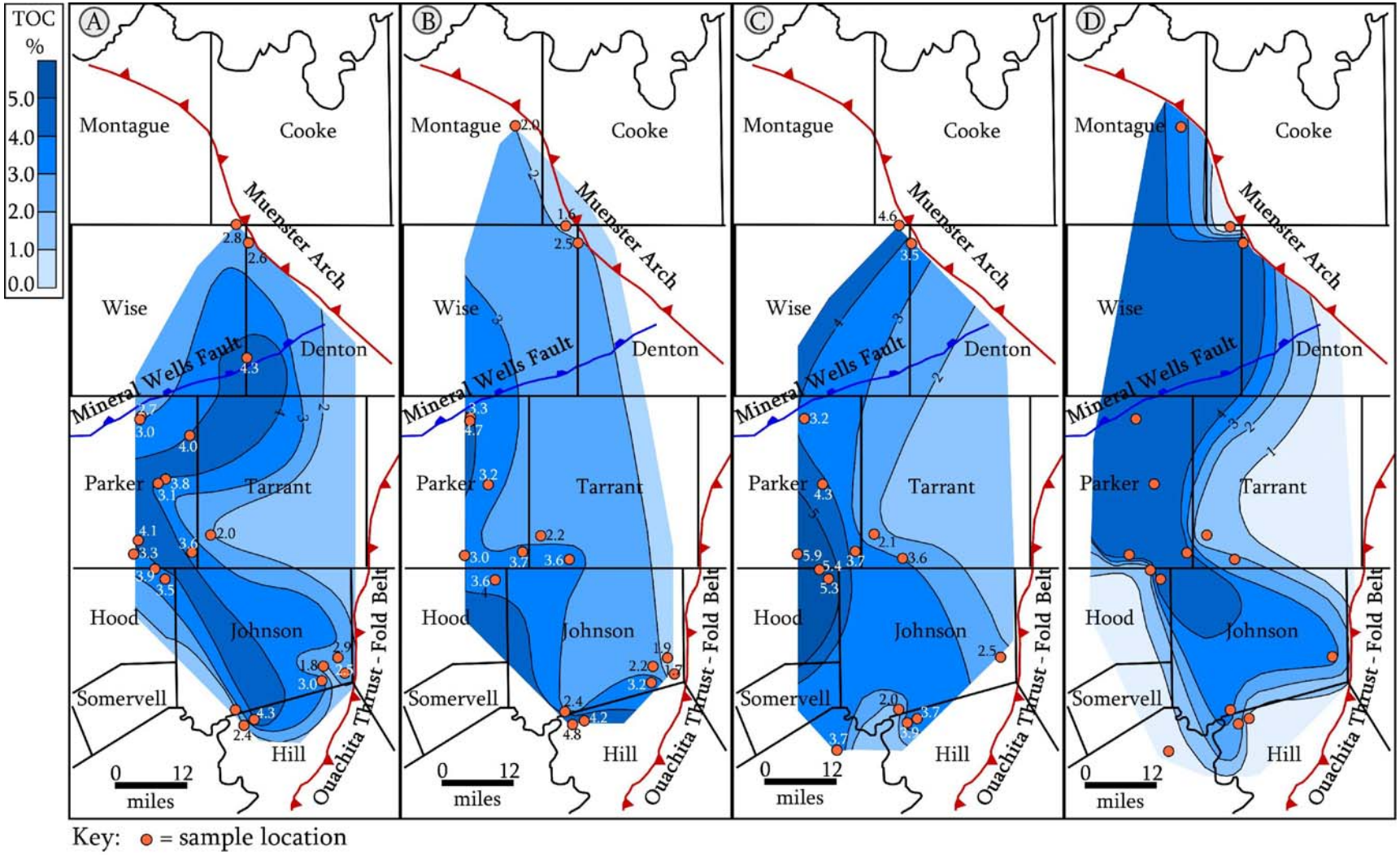

Figure 12: TOC content maps. A) Barnett Shale zone 5, B) Barnett Shale zone 6, C) Barnett Shale zone 7, D) Barnett Shale zone 8.

in the western portion of the study area, in Parker County and less often Wise County.

Barnett Shale zone 1. Zone 1 has the highest organic carbon concentrations located in east central Parker County, southeast Parker County, portions of southwest Tarrant County and north Johnson County.

Barnett Shale zone 2. Zone 2 has the highest organic carbon concentrations located in southeast Wise County, northeast Parker County, south central Parker County, southwest Tarrant County, northeast Hood County and north Johnson County.

Barnett Shale zone 3. Zone 3 has the highest organic carbon concentrations located in Parker County, northeast Hood County, southwest Tarrant County and north Johnson County.

Barnett Shale zone 4. Zone 4 has the highest organic carbon concentrations located in southeast Wise County, southwest Denton County, Parker County, Tarrant County, northeast Hood County and north Johnson County.

Barnett Shale zone 5. Zone 5 has three areas of high organic carbon concentration. One organic rich area is located throughout Parker County another area is located in southeast Wise County, southwest Denton County and northwest

Tarrant County, and the other high organic carbon area is located throughout central Johnson County to north Hill County.

Barnett Shale zone 6. Zone 6 has its highest organic carbon concentrations confined to the western and southern regions of the study area in Parker, Hood, west Johnson and north Hill counties.

Barnett Shale zone 7. Zone 7 has the highest organic carbon concentrations located in northeastern Wise, Parker and Hood Counties.

Barnett Shale zone 8. Zone 8 has the highest organic carbon concentrations positioned in eastern Montague, northeastern Wise, Parker, northeastern Hood and Johnson Counties.

Discussion

Zones with higher TOC most likely represent time periods during Barnett deposition where conditions met one or more of the following: 1) an increased oxygen minimum zone (OMZ) that resulted in less destruction of organic matter, 2) enhanced organic matter production, or 3) time periods when the Barnett was sediment starved resulting in a higher proportion of organic matter within sediment. The changing spatial distribution of elevated organic matter abundance through time was most likely caused by one or more of the following: 1) shifts in oceanic productivity (algal blooms), 2) changes in ocean circulation patterns that could have

carried oxygen rich seawater to various locations, resulting in oxidation and destruction of organic matter, and 3) changes in the delivery system and/or the abundance of terrestrial organic matter to the basin via the Chappell Shelf and/or the Caballos Arkansas island chain.

CHAPTER THREE

Thermal Maturity of the Barnett Shale

The thermal maturity of the Barnett Shale has been found to be one of the major controls on recoverable hydrocarbons. Therefore, one of the main goals of this study is to document the thermal maturity of the Barnett Shale in different parts of the basin and to compare it to the production of hydrocarbons. Three methods are used in this study to assess the thermal maturity of various geographic regions of the Fort Worth Basin: 1) The Hydrogen Index (HI) of the organic matter, 2) vitrinite reflectance and 3) the carbon isotopic composition of produced methane. Vitrinite reflectance has traditionally been the most reliable and widely used indicator of thermal maturity. Because generating vitrinite reflectance data is time consuming and costly, a limited number of vitrinite reflectance analyses are typically collected. Using the HI and the carbon isotopic composition of methane vastly increases spatial coverage of the Fort Worth Basin and results in a much better understanding of the thermal history of the basin.

Results and Discussion

Hydrogen Index

The Barnett Shale has HI values ranging from 0 to 188 while averaging about 38 (Appendix B). As discussed in Chapter One, this range of HI values would

typically be interpreted as indicative of Type III or Type IV kerogen. However, previous studies have shown that the original kerogen in the Barnett Shale was Type II and that thermal decomposition has severely altered the character of the remaining orgainic matter (Jarvie, 2004, Hill et al., 2007). Therefore, HI in this study is used to interpret the thermal maturity of the basin. The most mature areas correspond to small HI values and the least mature areas correspond to large HI values. Figures 13 and 14 demonstrate spatial distribution of the HI in the eight zones of the Barnett Shale; refer to Figure 4 as a type log for the Barnett Shale.

Barnett Shale zone 1. Barnett Shale zone 1 has HI values ranging from 1 to 68 and averaging 31, it shows the least mature areas to be in the western portion of the study area located in west Montague County, west Wise County, west-central Parker County and northwest Hood County. Thermal maturity increases with proximity to the Muenster Arch and Ouachita Thrust and Fold Belt.

Barnett Shale zone 2. Barnett Shale zone 2 has HI values ranging from 3 to 75 and averaging 32, it shows the least mature areas to be located in Montague County, west Wise County, an area in northeast Wise/ northwest Denton Counties, west-central Parker County, south Parker County and Hood County. South of the Mineral Wells Fault, thermal maturity increases with proximity to the Ouachita Thrust and Fold Belt. There is also an area of higher thermal maturity north of the Mineral

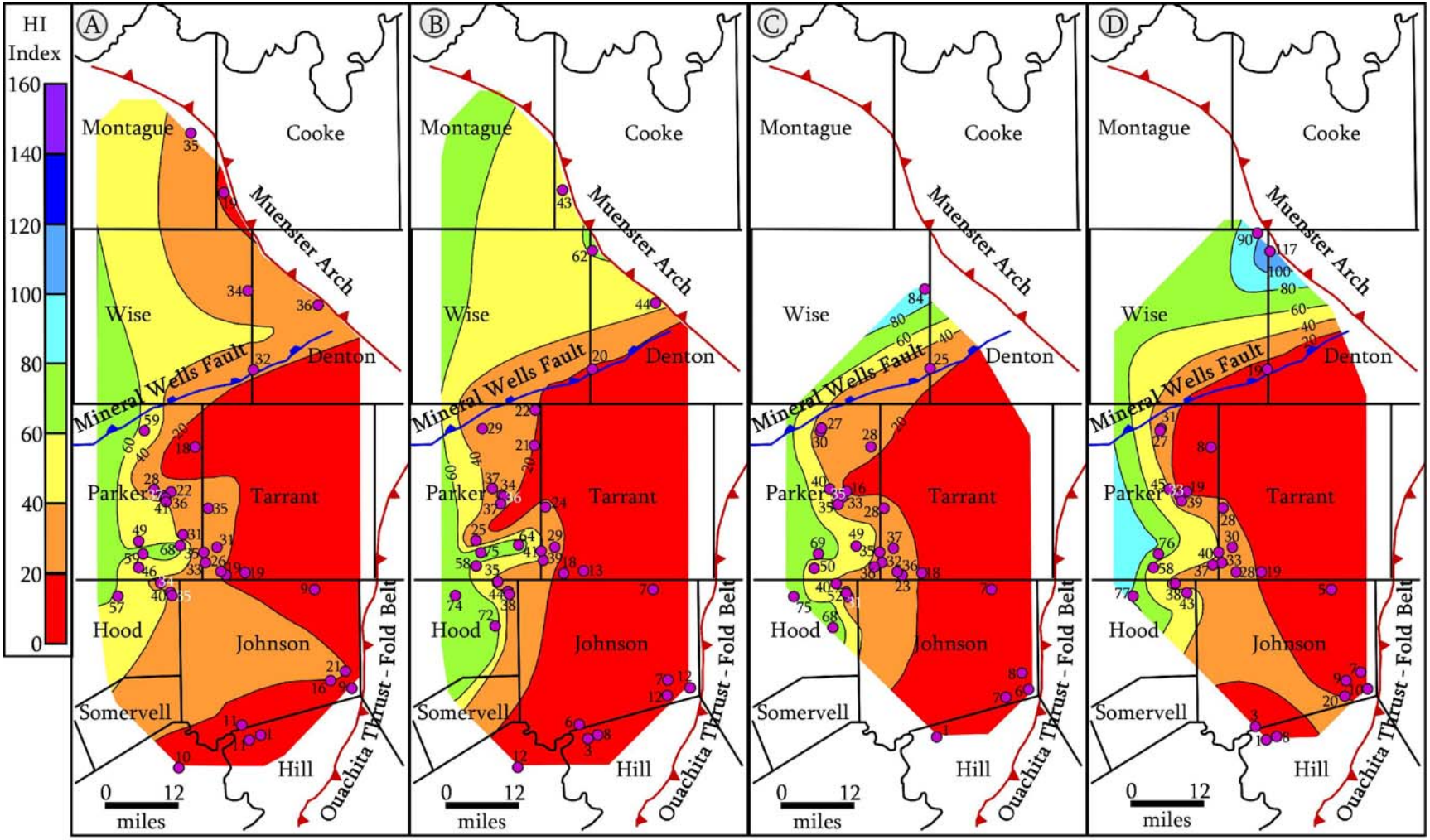

Figure 13: Hydrogen Index maps, warmer colors indicate a more thermally mature area. A) Barnett Shale zone 1, B) Barnett Shale zone 2, C) Barnett Shale zone 3, D) Barnett Shale zone 4.

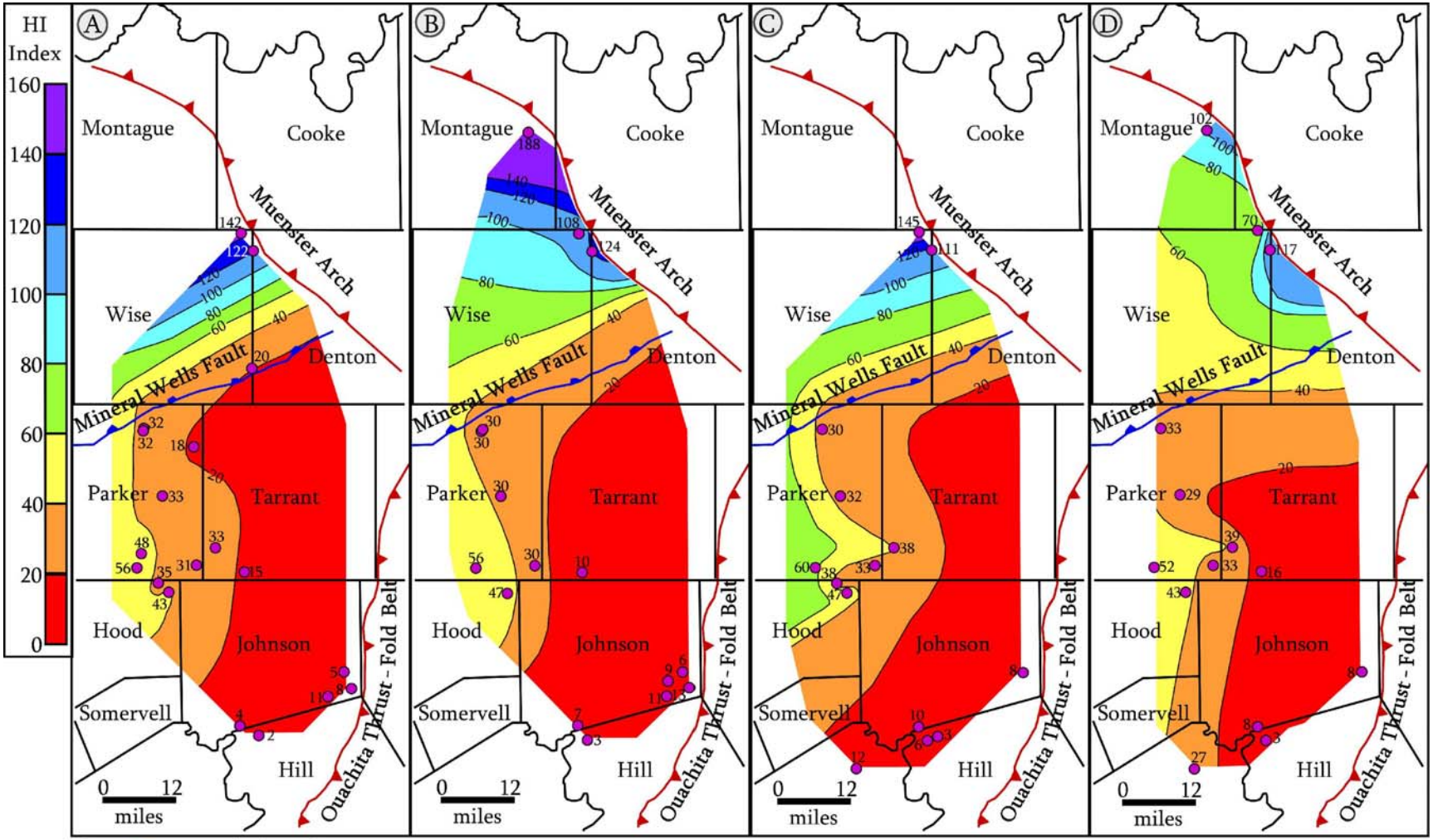

Figure 14: Hydrogen Index maps, warmer colors indicate a more thermally mature area. A) Barnett Shale zone 5, B) Barnett Shale zone 6, C) Barnett Shale zone 7, D) Barnett Shale zone 8.

Wells Fault located in southeast Montague/ southwest Cooke Counties, east Wise County, and central Denton County.

Barnett Shale zones 3 through 7. Barnett Shale zone 3 has HI values ranging from 1 to 84 and averaging 34. Barnett Shale zone 4 has HI values ranging from 1 to 117 and averaging 33. Barnett Shale zone 5 has HI values ranging from 2 to 142 and averaging 36. Barnett Shale zone 6 has HI values ranging from 3 to 188 and averaging 44. Barnett Shale zone 7 has HI values ranging from 3 to 145 and averaging 41. Barnett Shale zones 3 through 7 show the least mature areas to be located north of the Mineral Wells Fault and in east-central Parker County, south Parker County, and north Hood County. The thermal maturity increases with proximity to the Ouachita Thrust and Fold Belt and in south Johnson County and north Hill County.

Barnett Shale zone 8. Barnett Shale zone 8 has HI values ranging from 3 to 117 and averaging 41, it shows the least mature areas to be located in Montague County, Cooke County, northwest Wise County, northeast Denton County and south-central Parker County. The thermal maturity increases with proximity to the Ouachita Thrust and Fold Belt and in south Johnson County and north Hill County.

Vitrinite Reflectance

Barnett Shale vitrinite reflectance values range from 0.83 to 2.37 Ro (%) and average about 1.55 Ro (%) (Appendix C). Because the northern and the southern

parts of the Fort Worth Basin have undergone different burial histories (Figure 3), the thermal maturity of these two geographic areas differ and should be recorded by vitrinite reflectance. When vitrinite reflectance values from cuttings are plotted against present day burial depth (creating a depth-maturity profile), the northern and southern areas can be differentiated from each other (Figure 15). In general, wells to the north of the Mineral Wells fault have vitrinite reflectance values that range between 0.83 to 1.28 Ro (%) and average 1.05 Ro (%) whereas to the south of the fault vitrinite reflectance varies between 1.28 to 2.37 Ro (%) and average 1.78 Ro (%).

To test the hypothesis that different burial histories are the cause of this wide range of vitrinite reflectance values at similar depths across the basin, the estimated maximum burial depth of samples from the northern and southern areas (grossly derived from the burial history curves in Figure 3) have been plotted against present day vitrinite reflectance (Figure 16). This was completed by adding 4000 feet to the depths of the wells north of the Mineral Wells Fault and 6000 feet to the depths of the wells south of the Mineral Wells Fault. This figure clearly shows that the southern part of the basin has been buried the deepest, and as a result, has the highest vitrinite reflectance. Since the beginning of the Eocene, the Barnett Shale in both the northern and southern parts of the basin has experienced uplift resulting in similar present day burial depths but widely varying thermal maturities at about the same depths.

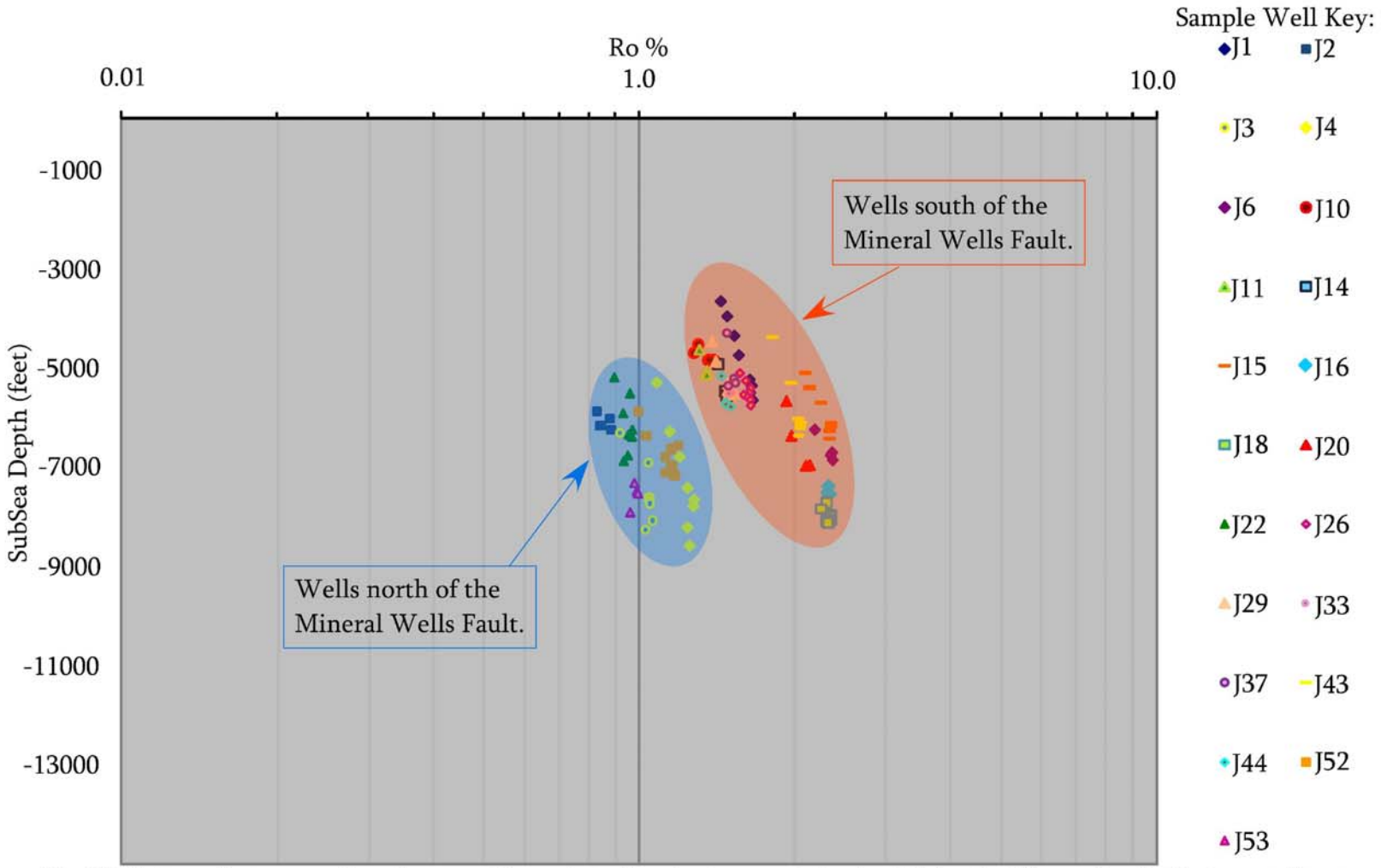

Figure 15: Vitrinite reflectance values from cuttings plotted against present day burial depth. The wells plot in two easily seen groups. The least mature group represents the northern study area of the Fort Worth Basin whereas the more mature group represents the southern study area of the basin.

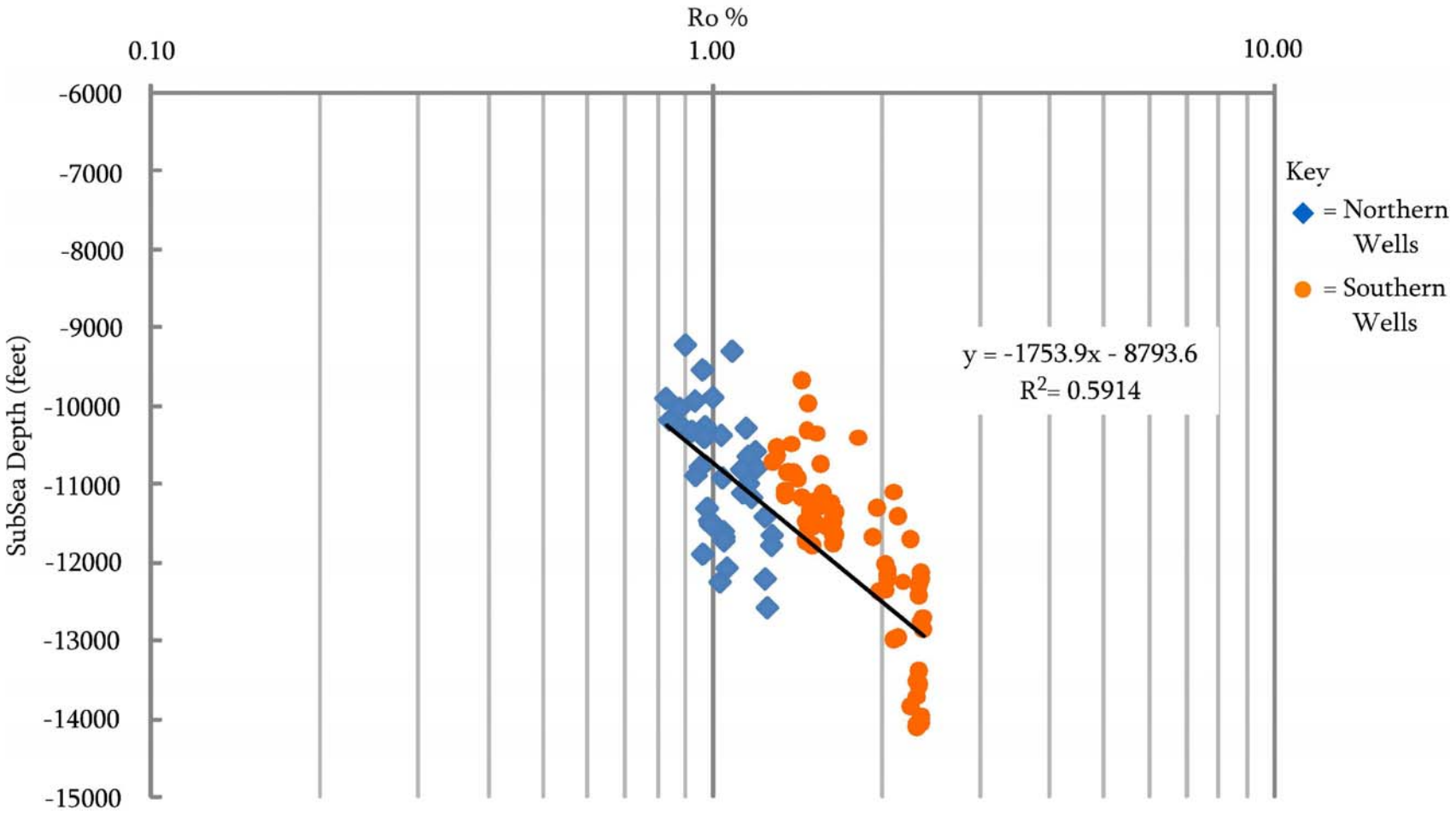

Figure 16: Estimated maximum burial depth graph (grossly derived from the burial history curves in Figure 3). 4000 feet was added to the depths of the northern wells (wells located north of the Mineral Wells Fault), and 6000 feet was added to all of the depths of the southern wells (wells south of the Mineral Wells Fault).

Within the northern and southern parts of the basin, smaller geographic regions with distinct burial and thermal histories can be identified based on depth-maturity profiles. These geographic areas are named Thermal Maturity Regimes and have been delineated by grouping wells that are in close geographic proximity to each other that generate similar depth-maturity profiles. The boundaries of the six Thermal Maturity Regimes have been found utilizing this method (Figure 17) and their spatial extent is shown on Figure 18.

Within the northern part of the Fort Worth Basin, two Thermal Maturity Regimes have been identified that have depth-maturity profiles that are parallel but slightly offset from one another (Figure 17). Thermal Maturity Regimes with parallel depth-maturity profiles are indicative of geographic areas that have similar geothermal gradients but different burial histories (Tobey, 2007). In this case, Regime 1 was buried less deeply than Regime 2.

There is a large geographic area in the northern part of the basin, mostly in Wise County, for which there are no vitrinite reflectance measurements. Nonetheless, in order to build a thermal maturity map for the entire basin this area must be accounted for. To remedy this problem, a proposed depth-maturity profile has been created. The development of this proposed depth-maturity profile is based on the knowledge gained from Figure 15, which indicates that the general thermal maturity of the Fort Worth Basin is subdivided into two groupings (the northern and southern areas) which is geographically separated by the Mineral Wells Fault. Thus,

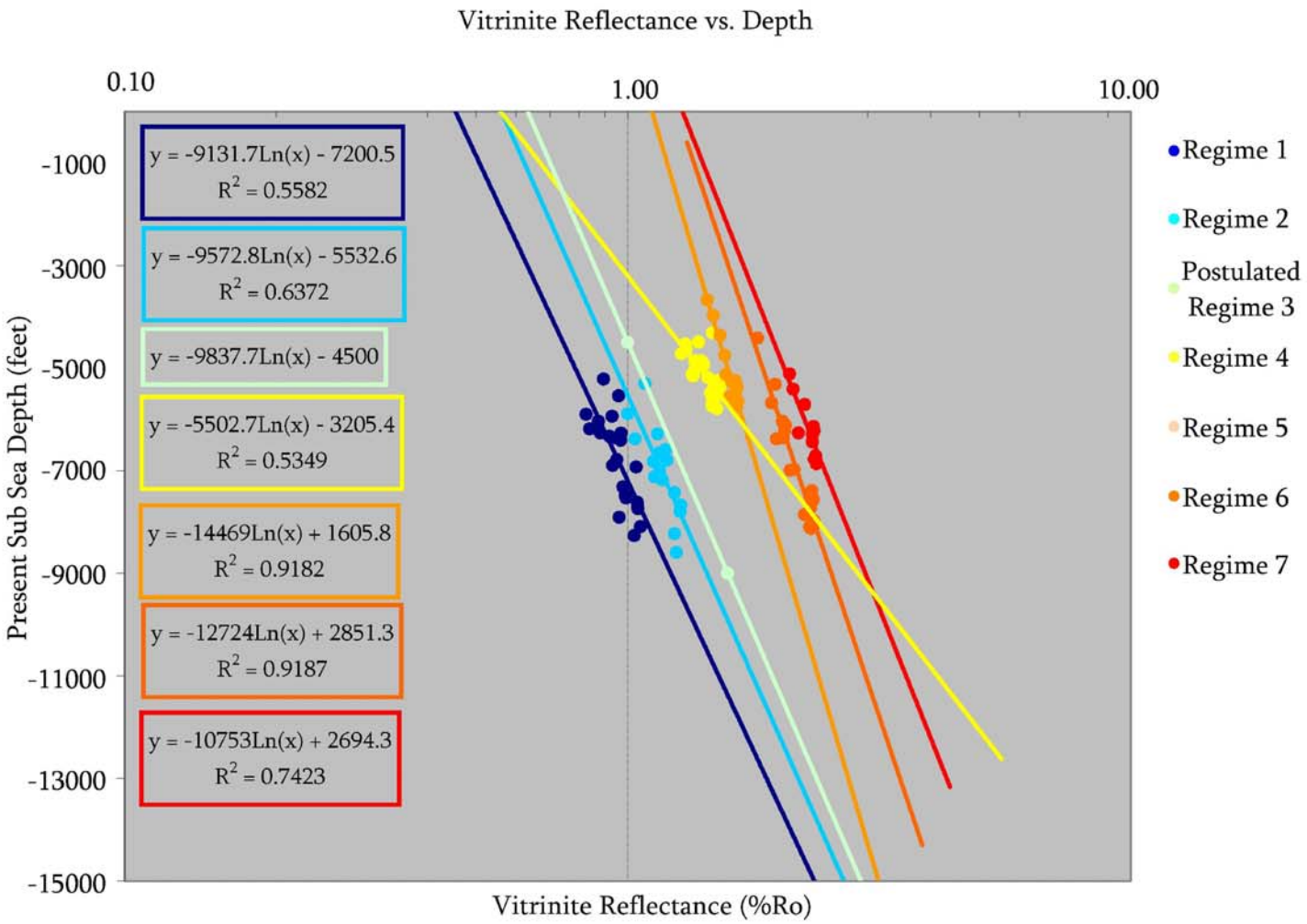

Figure: 17: Vitrinite reflectance (%Ro) versus sub sea depth. Each depth-maturity profile defines a geograpic region of similar burial history (maturity regime).

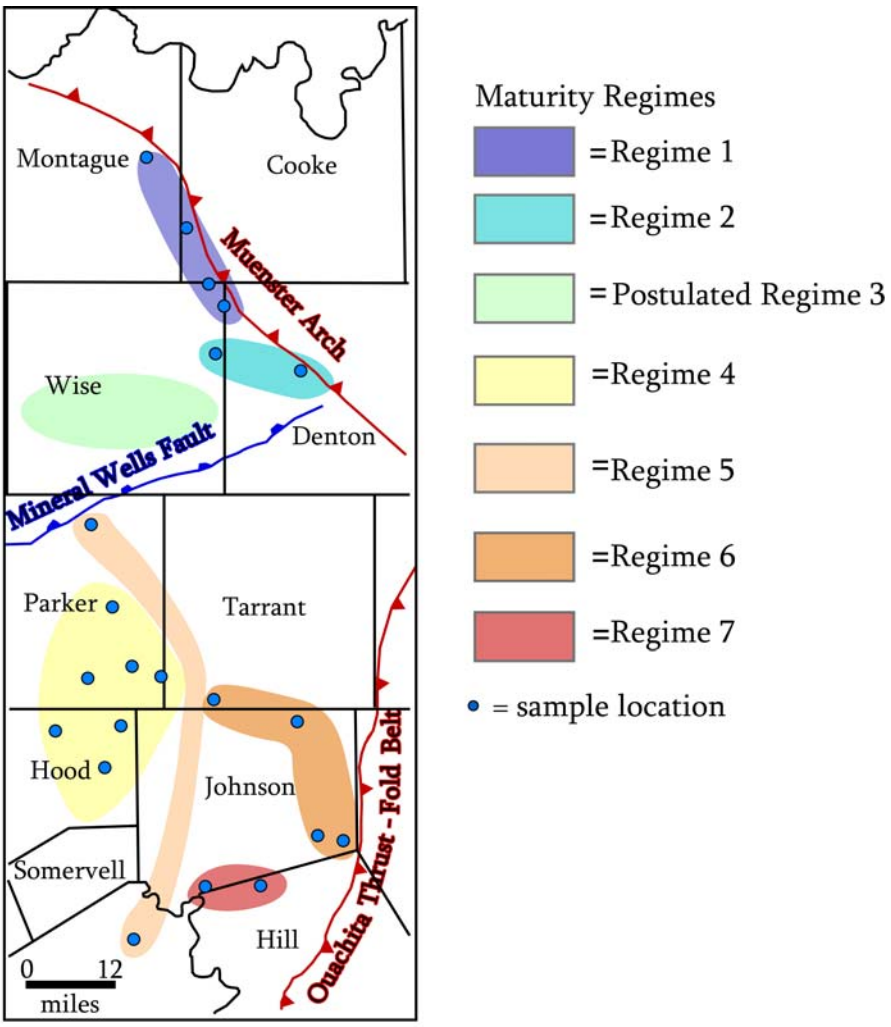

Figure 18: Maturity regimes map. The seven maturity regimes are color coordinated to the 7 depth-maturity profiles in Figure 17 (Depth-vitrinite reflectance Profile 1 corresponds to maturity Regime 1 and so on). Thermal maturity regimes increase in maturity from north to south; warmer colors indicate a more thermally mature regime.

the northern area of the Barnett Shale (above the Mineral Wells Fault) should have a general regional geothermal gradient and the southern area (below the Mineral Wells Fault) should have a separate general regional geothermal gradient. Because the geographic area of the proposed depth-maturity profile lies north of the Mineral Wells Fault it is proposed to have a similar geothermal gradient to depth-maturity profiles 1 and 2. Therefore, proposed Depth-maturity Profile 3 is parallel to depth-maturity profiles 1 and 2 but is hypothesized to have undergone slightly more burial because it is further south than Regimes 1 and 2. As a result, it is offset to the right of Regimes 1 and 2.

In the southern part of the basin four Thermal Maturity Regimes have been identified. These Regimes have increasingly higher vitrinite reflectance for a given present day burial depth indicating successively deeper burial histories. Interestingly, these depth-maturity profiles define slightly steeper slopes than the Thermal Maturity Regimes in the northern part of the basin, suggesting that the geothermal gradients were somewhat higher in the northern part of the Fort Worth Basin.

Regime 4 is the only regime that has a regression line that does not fall sub-parallel to the others. There are two possibilities that could explain such a different slope: 1) the data does not have a good depth range as the other maturity regimes and therefore the regression line is poorly constrained, or 2) there may be another heat source to the west, possibly the Bend Arch, causing the geothermal gradient to be higher in this area.

In summary, six Thermal Maturity Regimes and one Postulated Thermal Maturity Regime (Regime 3) have been identified in the Fort Worth Basin. These Regime areas are based on the relationship between vitrinite reflectance and present day burial depth. Equations describing the best fit line of the depth-maturity profiles of each Thermal Maturity Regime permit quantification of thermal maturity (in terms of vitrinite reflectance) at any depth within a particular Thermal Maturity Regime. For Example, Regime 1 is represented by Equation 1 which states that:

Eq. 1: $D = -9131.7\ln(VR) - 7200.5$

D = present day burial depth (sub sea)

VR = Vitrinite Reflectance (Ro (%))

Accordingly, the best fit line for the depth-maturity profile in Thermal Maturity Regime 1 predicts a vitrinite reflectance of 1.02 Ro (%) for a present day burial depth of 7000 feet. The slopes of these equations represent the geothermal gradient (the steeper the slope the smaller the geothermal gradient) and the y-intercept represents burial history (larger y-intercepts represent deeper burial depths).

The vitrinite reflectance of the Thermal Maturity Regimes are summarized below: 1) Maturity Regime 1 ranges from 0.83 to 1.06 Ro (%) and averages 0.96 Ro (%), it is located in Montague, Cooke, northeast Wise and northwest Denton Counties, 2) Regime 2 ranges from 1.00 to 1.28 Ro (%) and averages 1.17 Ro (%), it is located in east-central Wise and west-central Denton Counties, 3) Postulated Regime 3 is located in central Wise County, 4) Regime 4 ranges from 1.28 to 1.53 Ro (%) and

averages 1.44 Ro (%), it is located in central Parker County, southeast Parker County and northeast Hood County, 5) Regime 5 ranges from 1.44 to 1.66 Ro (%) and averages 1.60 Ro (%), it represents two wells that have highly correlated linear relationships between vitrinite reflectance and burial depth even though they are geographically farther apart, one of these wells is located in northeast Parker County and the other is located in North Bosque County (Figure 18), 6) Regime 6 has vitrinite reflectance that ranges from 1.81 to 2.35 Ro (%) and averages 2.17 Ro (%), it is located in southwest Johnson and north Hill Counties, and 7) Regime 7 ranges from 2.10 to 2.37 Ro (%) and averages 2.29 Ro (%), it is located in north Johnson County and east Johnson County. The thermal maturity regimes identified by vitrinite reflectance show a general trend of increasing thermal maturity from north to south in the Fort Worth Basin.

$\delta^{13}C$ of Produced Methane

The isotopic composition of carbon in methane can be used as an indicator of thermal maturity. Biogenic or thermogenic formation of methane from organic matter results in extremely negative carbon isotope ratios ($\delta^{13}C_{CH4}$ of -80‰ or less in the gas) (Hoefs, 2004). This is because the bonds between ^{12}C atoms in organic matter are slightly weaker than the bonds made by ^{13}C atoms, and as a result, methane gas becomes enriched in ^{12}C as these bonds are preferentially broken during methanogenesis. More importantly, the isotopic composition of this methane gas is

subsequently modified as is undergoes thermal cracking to CO_2 and this can be used as an indicator of thermal maturity. During cracking of methane, molecules with the light isotope of carbon are once again preferentially destroyed. As higher temperatures cause more of the methane to react, the carbon isotopic composition of the remaining gas becomes more positive (Stahl, 1977). In addition to the degradation of methane, overcooked sapropelic source material also generates isotopically heavier methane (up to -30‰) (Stahl, 1977).

It is much easier and less expensive to measure the carbon isotopic composition of produced methane than to measure the vitrinite reflectance of cuttings. Therefore, if a relationship between the isotopic composition of methane and coeval vitrinite reflectance is determined, it would enhance the number of control points used for determining the geographic range of the thermal maturity regime areas (areas of similar burial history) (Stahl and Carey, 1975; Stahl et al., 1977; Faber, 1987; Berner and Faber, 1988; Shen Ping et al., 1988; all in Rooney et al., 1995).

The Barnett Shale has $\delta^{13}C_{CH4}$ values ranging from -55.2 to -35.7 and averaging about -42.8 (Appendix D). Figure 19 is a graph of $\delta^{13}C_{CH4}$ verses subsea depth. When the $\delta^{13}C_{CH4}$ is plotted against present day burial depth, the northern and southern parts of the basin are once again easily differentiated. The isotopic composition of methane from the northern part of the basin has more negative $\delta^{13}C_{CH4}$ values indicating a lower thermal maturity. Furthermore, the data can be subdivided into

the previously identified Thermal Maturity Regimes using the gas samples proximity to the Regime areas and its $\delta^{13}C_{CH4}$ value and sub sea depth.

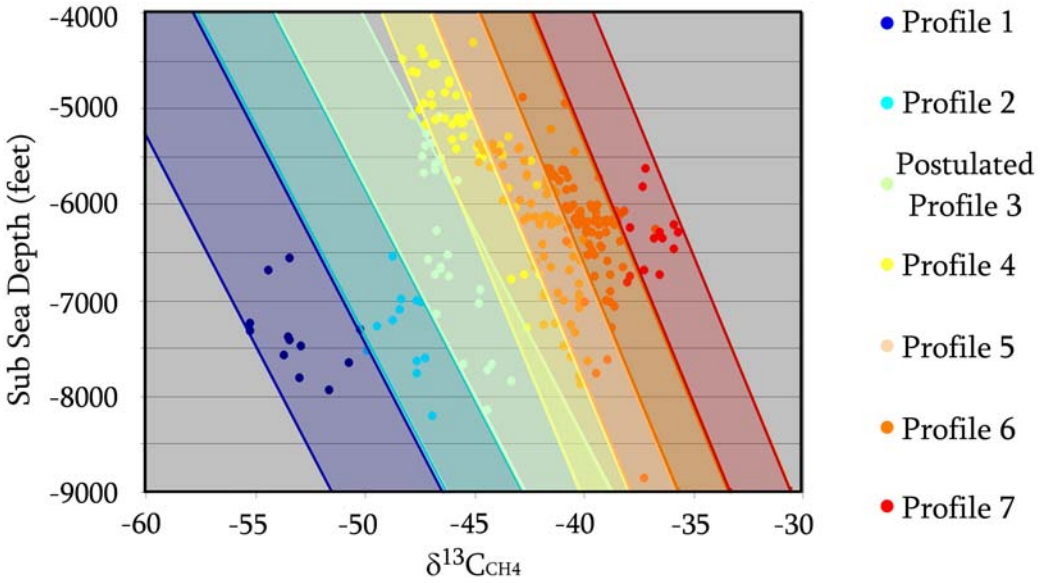

Figure 19: Produced $\delta^{13}C_{CH4}$ data plotted against sub sea depth. The seven depth-$\delta^{13}C_{CH4}$ profiles correspond to the seven depth-vitrinite reflectance profiles.

Because each Thermal Maturity Regime has an established thermal maturity for a given present day burial depth, it is now possible to assign a thermal maturity (in terms of vitrinite reflectance) to any methane sample if the depth of production is known. For example, methane from McMurrey Ranch (API# 42121326520000) well has a $\delta^{13}C_{CH4}$ of -51.6 ‰ and is produced from a depth of -7939 feet. Because this well falls in the Thermal Maturity Regime 1, Equation 1 describes the depth-maturity profile for this geographic area and thus can be used to assign a thermal maturity (in terms of vitrinite reflectance) to the depth from which the gas is produced. The result of this calculation yields a vitrinite reflectance value of 1.08 Ro (%) for a $\delta^{13}C_{CH4}$ of -

51.6 ‰. Using the $\delta^{13}C_{CH4}$ data as a proxy for vitrinite reflectance increases the data set from 21 sample locations to 236 sample locations.

Proxy vitrinite reflectance data was checked and further refined by comparing the $\delta^{13}C$ of methane against the proxy vitrinite reflectance (Figure 20). Proxy vitrinite reflectance points that did not fall on or near the resulting best fit trend line were moved to another thermal maturity regime until the best relationship between $\delta^{13}C_{CH4}$ and proxy vitrinite reflectance was achieved. The only data points that could not be brought onto the best fit line are from Regime 1. This geographic region has been influenced by hydrothermal events (discussed later in the chapter) that have affected the maturity of the uppermost zones of the Barnett Shale. This is consistent with the data points falling to the more thermally mature side of the best fit trend line. Proxy vitrinite reflectance and the $\delta^{13}C_{CH4}$ is highly correlated with a regression coefficient of 0.87. This relationship supports the theory that the $\delta^{13}C$ of produced methane is a good surrogate for measured vitrinite reflectance.

Figure 21 is a Thermal Maturity Regime map constructed from vitrinite reflectance and proxy vitrinite reflectance data. The maturity regime map defines the boundaries of all seven of the geographic areas that have undergone different burial histories. This map shows the thermal maturity of the basin to increase from the north (least mature) to the south and east (most mature).

Maturity Regime 1 ranges from 0.93 to 1.08 proxy Ro (%) and averages 1.02% proxy Ro. It is located in Montague, Cooke, north Wise, east-central Wise and

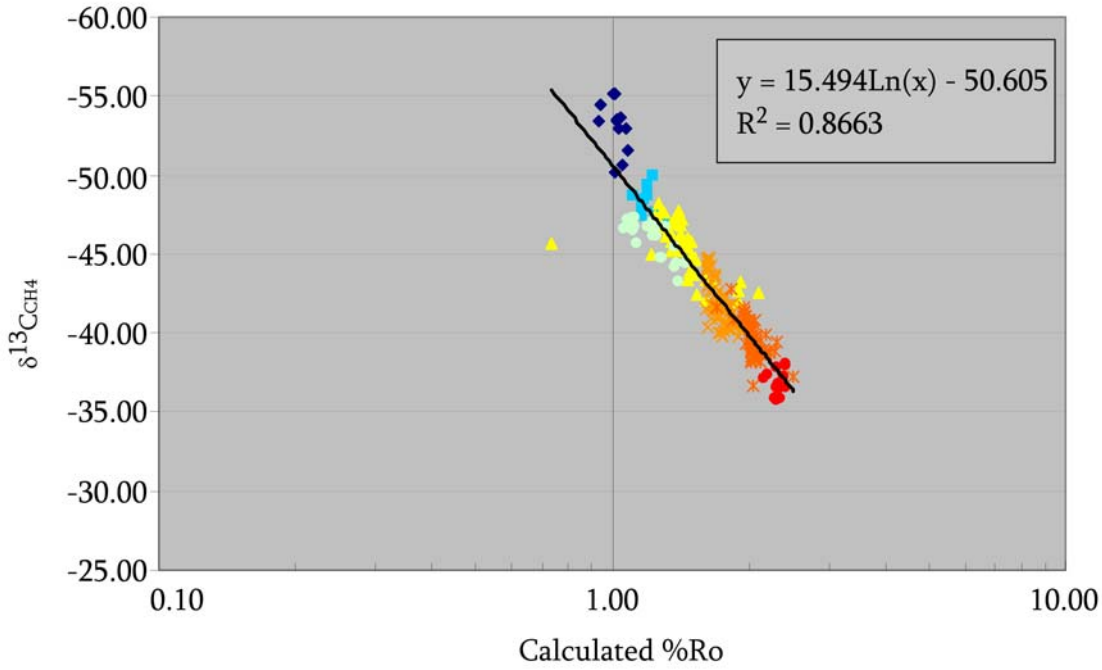

Figure 20: Proxy vitrinite reflectance verses the carbon isotopic composition of methane.

northwest Denton Counties. Regime 2 ranges from 1.11 to 1.32 proxy Ro (%) and averages 1.21 proxy Ro (%). It is located in east-central Wise and west-central Denton Counties. Regime 3 ranges from 1.06 to 1.45 proxy Ro (%) and averages 1.22 proxy Ro (%). It is located in central Wise County, east Wise County and east Denton County. Regime 4 ranges from 0.74 to 2.10 proxy Ro (%) and averages 1.45 proxy Ro (%). It is located in southeast Wise County, part of southwest Wise County, part of southeast Denton County, central Parker County, south Parker County, east Hood County and northeast Johnson County. Regime 5 ranges from 1.60 to 1.93

proxy Ro (%) and averages 1.74 proxy Ro (%). It is located in southeast Wise County,

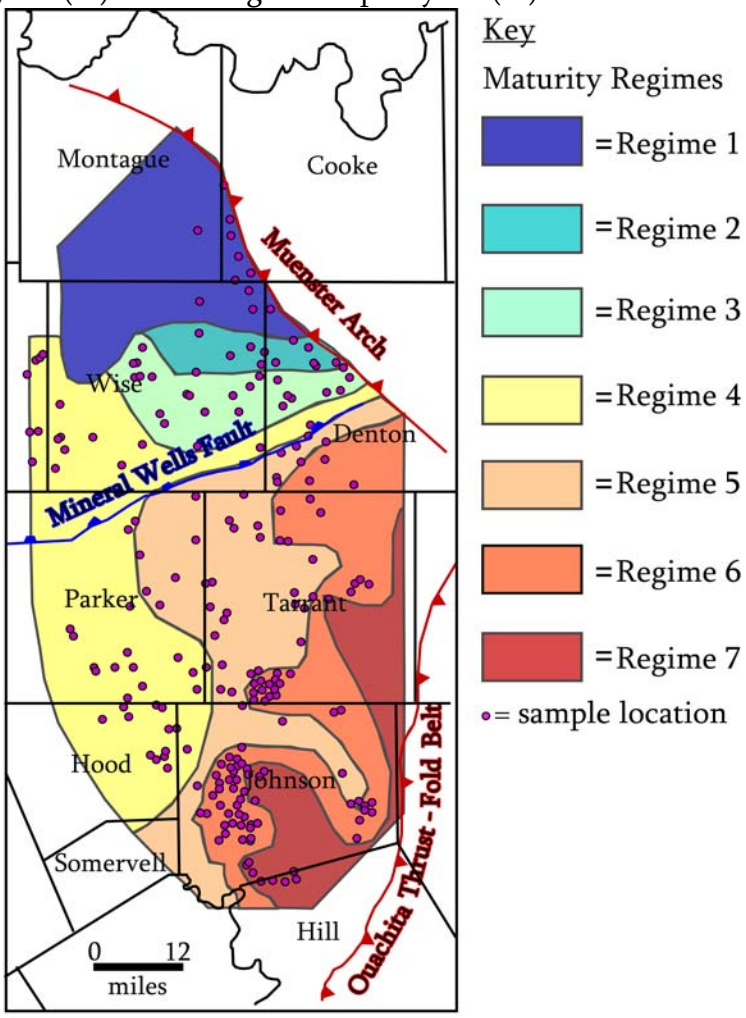

Figure 21: Expanded maturity regimes map. Warmer colors indicate more mature regimes.

part of southwest Denton County, northeast Parker County, west Tarrant County, central Tarrant County, north Johnson County, and west Johnson County. Regime 6 ranges from 1.70 to 2.51 proxy Ro (%) and averages 2.05 proxy Ro (%). It is located in areas of central Johnson County, east Johnson County, south-central Tarrant County, northeast Tarrant County and south Denton County. Regime 7 ranges from 2.17 to 2.42 proxy Ro (%) and averages 2.33 proxy Ro (%). It is located in east Tarrant

County, central Johnson County, east Johnson County and north Hill County. Above the Mineral Wells Fault maturity regimes trend north to south (as they did in vitrinite reflectance data shown in Figure 18). North being the least mature and the further south (or closer to the Mineral Wells Fault) the more mature the regimes become. South of the Mineral Wells Fault the maturity regimes trend slightly different. Regimes increase in thermal maturity in a southeastern direction with proximity to the Ouachita Fold and Thrust Belt and Hill County.

Figure 22 represents the final thermal maturity map of the Barnett Shale made from the proxy vitrinite reflectance values. Figure 23 shows the published thermal maturity map from Pollastro et al., 2004, and Figure 24 illustrates the differences between the two thermal maturity maps. The thermal maturity map constructed in this study (Figure 22) demonstrates that the Barnett is least mature in the north and increases in thermal maturity to the southeast. The thermal maturity map generated in this study differs significantly in both the orientation of maturation contours and the level of maturation from Pollastro's 2004 map. The vitrinite reflectance from Pollastro's map ranges from approximately 0.5 to 2.0 Ro (%) and the thermal maturity gradient trends west (least mature) to east (most mature) (Figure 23). There are also two areas of higher maturity located in Tarrant and Bosque Counties that are supported by only 15 data points in Tarrant County and only two data points in Bosque County.

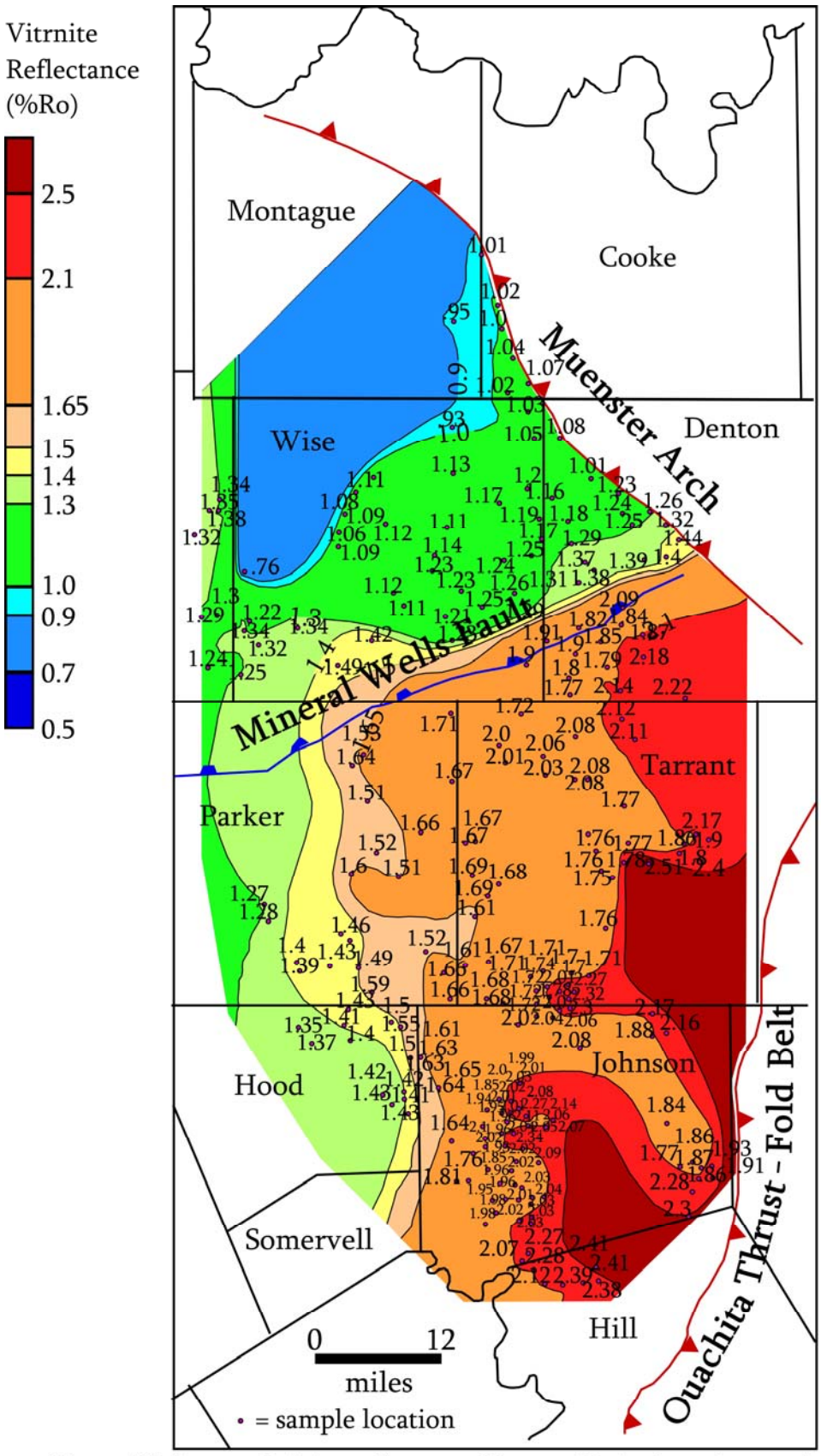

Figure 22: Proxy vitrinite reflectance Barnett Shale themal maturity map.

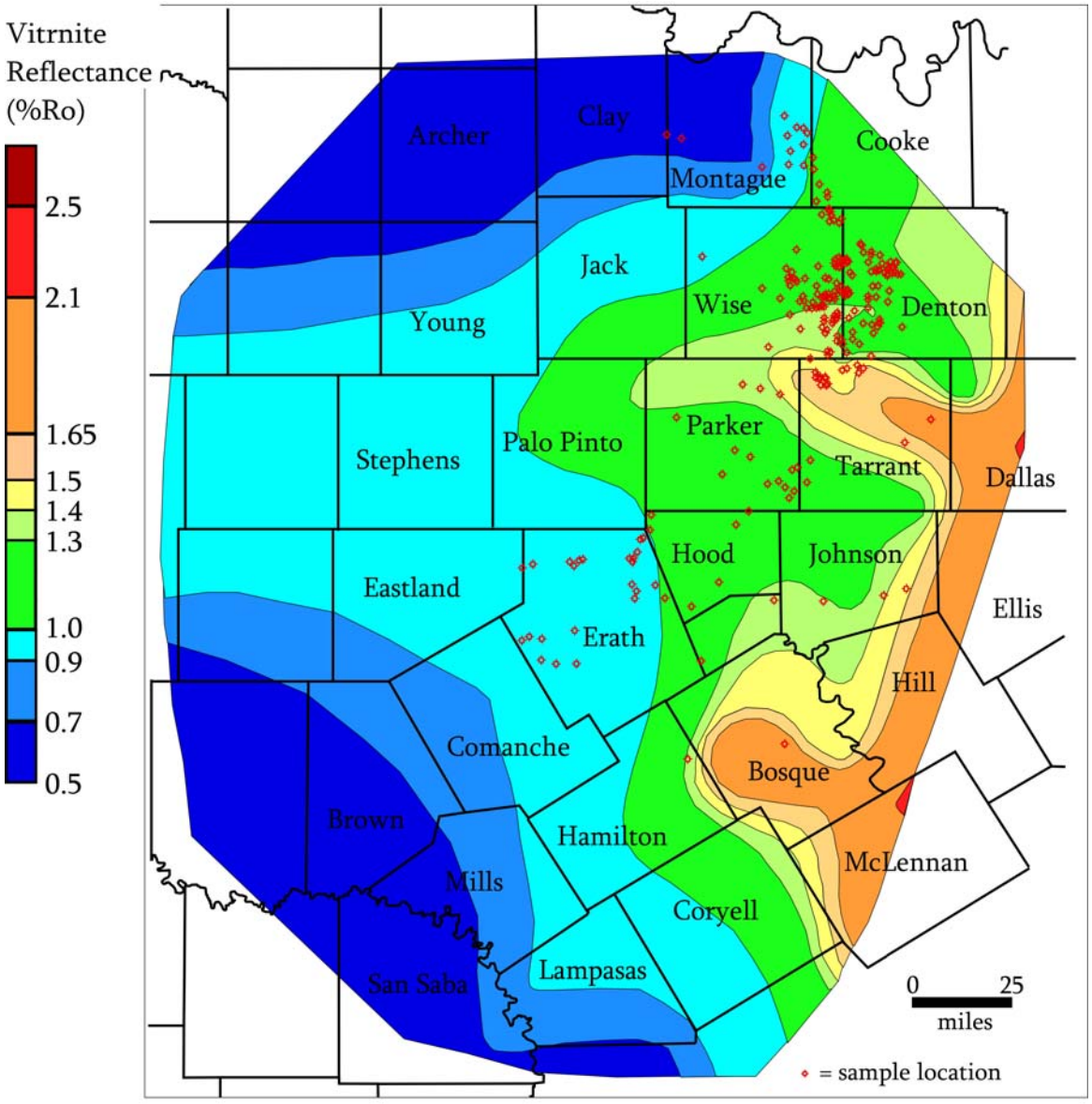

Figure 23: Published Barnett Shale thermal maturity map from Humble Geochemical (Pollastro et al., 2004)

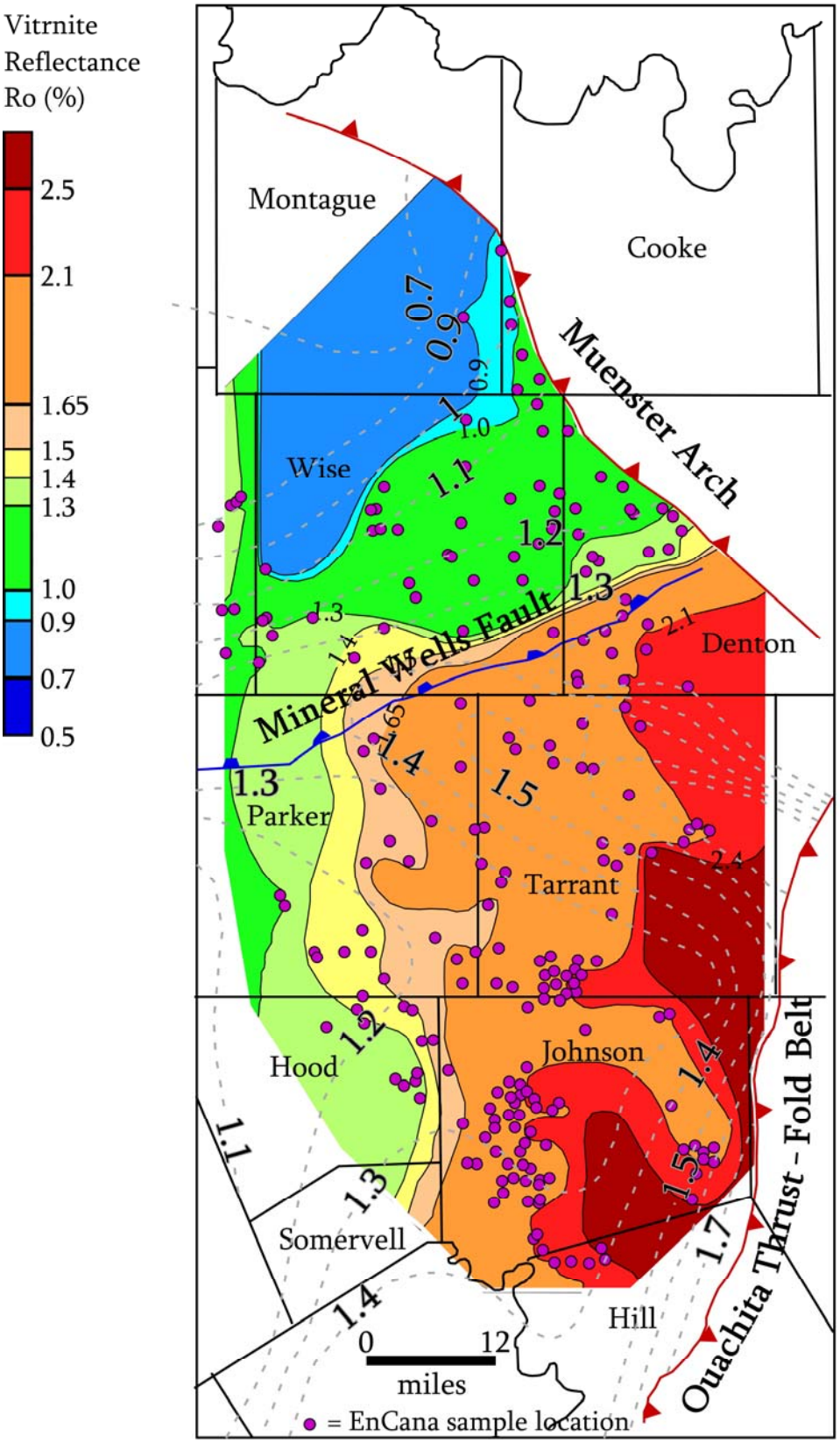

Figure 24: EnCana Barnett Shale proxy vitrinite reflectance thermal maturity map overlain by the published thermal maturity contours (dashed) (Pollastro et al., 2004).

Thermal Maturity of the Basin

Previous studies have suggested that the main controls on the thermal maturity of the Barnett Shale are hydrothermal fluids sourced from the Ouachita structural front and other prominent structural features in the basin (Benthke and Marshak, 1990; Kupecz and Land, 1991; Pollastro et al., 2003; Pollastro et al., 2004; Pollastro et al., 2007; Montgomery et al., 2005, 2006; Jarvie et al., 2007). The published maturity map shown in Figure 23 supports this suggestion; irregularities in this map are explained by structural features that enhance the flow of hydrothermal fluids. There seems, however, to be several differences with Pollastro's map compared to the one generated in this study. First, much of the data from Pollastro's maturity map is clustered within Denton and Wise Counties whereas the amount of control in this study is much greater. Secondly, it is not known if vitrinite reflectance was measured over a range of depths in one well (a depth maturity profile) or if a single vitrinite reflectance measurement was recorded for each well. Depth maturity profiles give a much better representation of the geothermal gradient than one single vitrinite reflectance measurement does. Generating depth maturity profiles also allows for the assessment of depth verses maturity profile trends which aids in locating areas of similar/dissimilar burial history or heat flow (maturity regimes). Measuring only one sample per well inhibits any comparison between different geographic areas. Lastly, measuring vitrinite reflectance is highly dependent upon the skill of the organic petrographer making the measurements. The fact that gas

isotope data, methane abundance and the HI independently support the measured vitrinite reflectance measurements used in this study lends confidence to the maturation assessments.

This study suggests that the burial history has the greatest impact on the thermal maturity of the Barnett Shale (as seen in Figure 17). As the depth-maturity profiles become progressively more mature they keep relatively similar slopes (geothermal gradients). This indicates that the different burial depths that occurred during the Barnett Shales history is the main influence on its thermal maturity. The similar geothermal gradients of the maturity regimes also indicate that the heat flow from the Ouachita structural front generally affects the entire study region as a whole; otherwise the slopes would increase much more with proximity to the Ouachita structural front. Though the geothermal gradient may be slightly higher, the more proximal the Barnett Shale Strata are to the Ouachita Structural front (seen in Figure 17 as the geothermal gradient slightly increases from Profiles 5 to 7) it is not the largest influence on the Thermal Maturity of the basin. If the heat flow from the Ouachita structural front was the main control on thermal maturity, as previously believed, the geothermal gradient of the depth-maturity profiles would increase from Profile 1 to 7. However, the small variations seen between the seven depth-maturity profile slopes are most likely caused by one or both of the following: 1) the Ouachita Fold and Thrust Belt and the Muenster Arch (the two main known sources of heat aside from burial depth) have produced different geothermal gradients causing the

northern area (north of the Mineral Wells Fault) and the southern area (south of the Mineral Wells Fault) to have different geothermal gradients which is expressed in the measured vitrinite reflectance values and 2) some of the depth-maturity profiles have more samples than others, this allows some of the depth-maturity profiles to be very tightly constrained while others may skew.

Thermal Maturity Controls on Production

Knowledge of the regional thermal maturity allows for the assessment of hydrocarbons in the following ways: 1) it allows one to know if the area is thermally mature enough to produce hydrocarbons and 2) it allows one to assess the type of hydrocarbons present. It is understood that areas with a vitrinite reflectance greater than 0.6 Ro (%) will be mature enough to produce hydrocarbons, areas with a vitrinite reflectance from 0.6 to 1.0 Ro (%) will produce oil, 1.0 to 1.4 Ro (%) will produce condensate/wet gas, and 1.4 to 2.1 Ro (%) will produce dry gas (Jarvie, 2004, Tobey, 2007). Any rock with a vitrinite reflectance value greater than 2.1 Ro (%) could have high levels of CO_2 and risk reduced porosity and permeability due to such high levels of thermal maturity (Table 4) (Tobey 2007). In mudrocks that have very low permeability (such as the Barnett Shale), the hydrocarbon phase has a huge impact on the deliverability (the ability for hydrocarbons to be produced from the well during the completion process) of the well.

Table 4: Vitrinite reflectance production information (Jarvie, 2004)

	Vitrinite Reflectance Break-down
%Ro	Hydrocarbon Generation
< 0.6	Immature
0.6 - 1.0	Oil Generation Window
1.0 - 1.4	Condensate/ Wet Gas Generation Window
1.4 - 2.1	Dry Gas Generation Window
> 2.1	Reservior Destruction, CO_2 Risk

Figure 25 illustrates the relationship between thermal maturity and the daily average during the first month of hydrocarbon production in mcfe (thousand cubic feet equivalent, using oil to gas ratio of 6:1) for all wells with measured or proxy vitrinite reflectance. The R^2 for this relationship is equal to 0.32; this is a fairly robust relationship when considering there are many other factors influencing production besides thermal maturity. A comparison between initial production and vitrinite reflectance allows for the recognition of high hydrocarbon productivity at specific levels of thermal maturity. In this case, the highest hydrocarbon production is generally within a vitrinite reflectance range of 1.65 to 2.08 Ro (%) (shown by the orange rectangle). This vitrinite reflectance range encompasses Thermal Maturity Regimes 5 and 6. This optimal hydrocarbon production range (1.65 to 2.08 Ro (%)) is also supported by Figures 26 and 27 which show the average initial production (IP) of

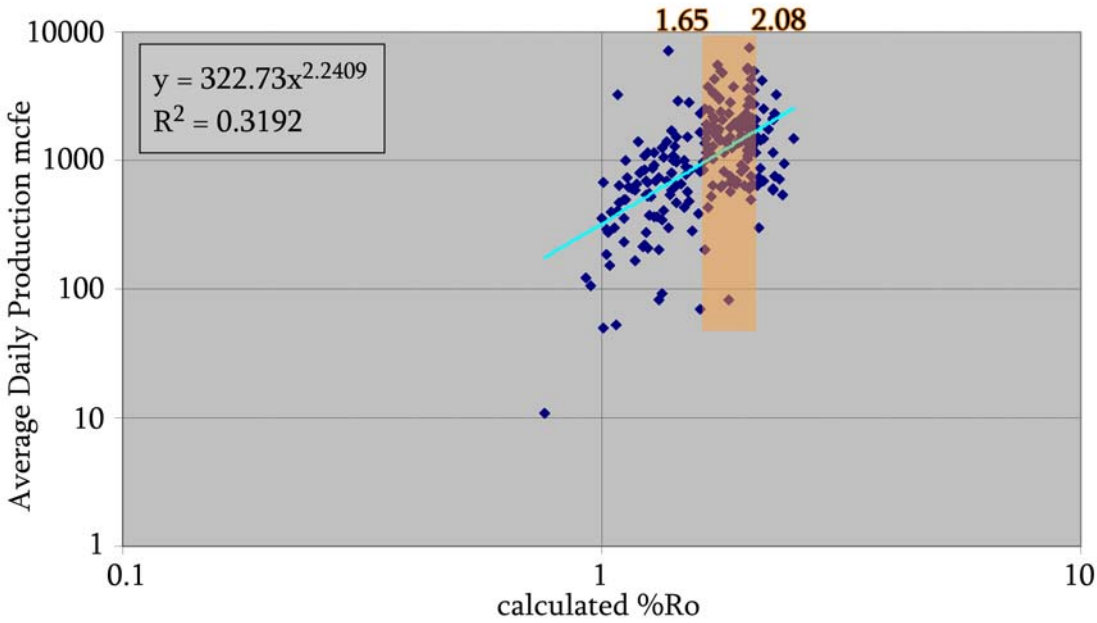

Figure 25: Daily average of the first month of procuction in mcfe (thousand cubic foot equivalent using 6:1 oil to gas ratio) verses the proxy vitrinite reflectance. The orange box highlights optimal production within a vitrinite reflectance range.

the maturity regimes (with Regimes 5 and 6 grouped). The optimal range occurs well within the dry gas hydrocarbon generation window (Table 4). Figures 26 and 27 demonstrate how the regime areas compare in regard to production. After combining Regimes 5 and 6, which represents a range of vitrinite reflectance that has the highest hydrocarbon production of all Thermal Maturity Regimes, an equation was used to rate the average production from the other maturity regimes with respect to combined Regimes 5 and 6 (Production Comparison Equation = [mean IP of Regime n/(mean IP of Regime n + mean IP of Regimes 5 and 6)]×2). The second best producing regime is Regime 7 producing at 80% the level of combined Regimes 5 and

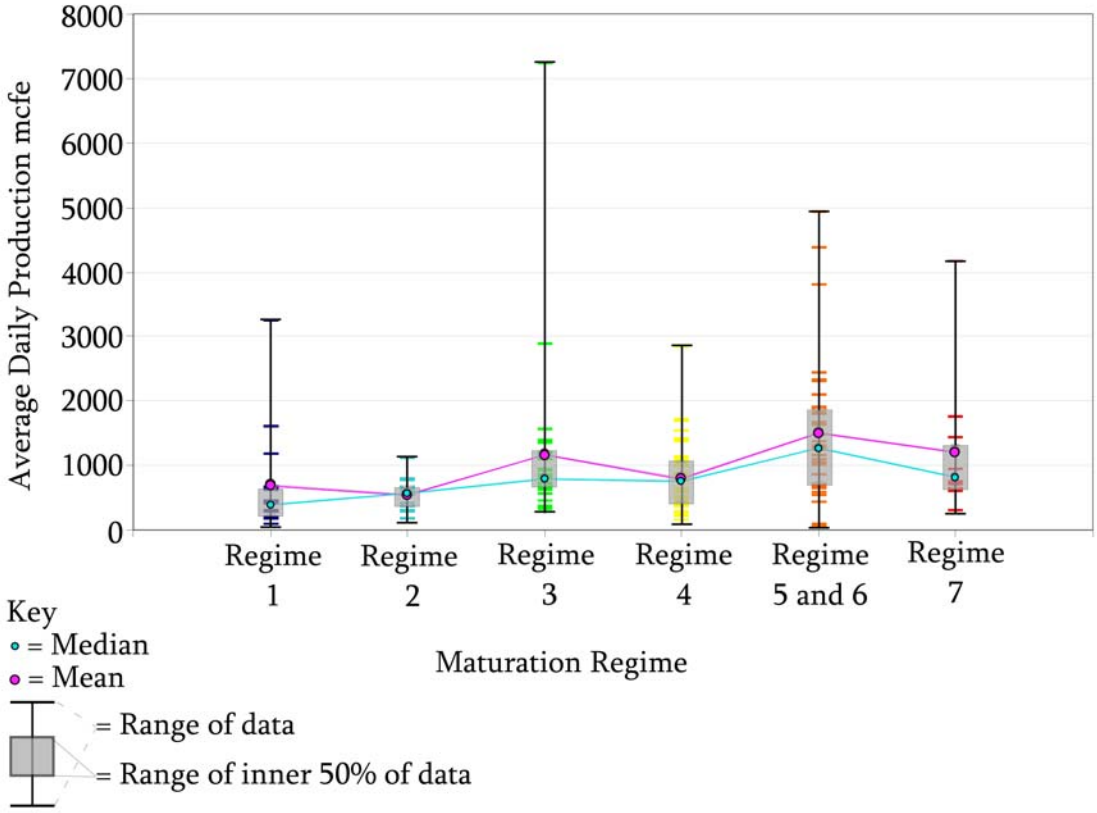

Figure 26: Regime area comparison of hydrocarbon production. This figure shows the range of average daily production for the first month of production mcfe (using 6:1 oil to gas ratio) within the geographic limits of Regimes 1 through 7 (Regimes 5 and 6 are grouped).

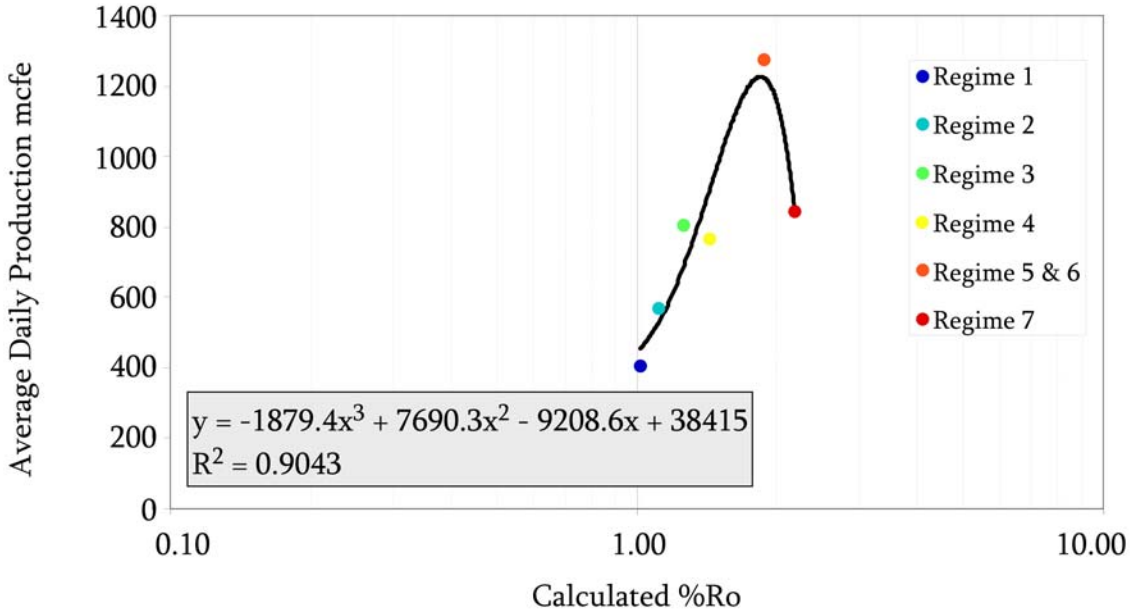

Figure 27: Median average daily production for first month of production (thousand cubic feet equivalent, using 6:1 oil to gas ratio) verses median calculated vitrinite reflectance of regime area; regime areas 5 and 6 are grouped.

6. Regime 3 produces at 77% the level of combined Regimes 5 and 6. Regime 4 produces at 75% the level of Regimes 5 and 6. Regimes 2 and 1 produce at 62% and 48% respectively in comparison with combined Regimes 5 and 6.

The optimal producing vitrinite reflectance range (including Regimes 5 and 6) indicates the dry gas hydrocarbon generation window. The optimal producing vitrinite reflectance range most likely occurs in the dry gas generation window because the deliverability (ability to produce hydrocarbons) of dry methane gas is much better than condensate and wet gas. In an extremely low permeability reservoir dry methane gas is much more deliverable than condensate/wet gas because of its smaller molecular size. Larger condensate/wet gas molecules are not as easily

transported through low permeability mudrocks. Deliverability is also affected by the fluid viscosity (measure of fluid friction). Dry methane gas is less viscous, and therefore has much less internal resistance to flow and will flow easier than condensate and wet gas.

In order to analyze the production potential of each maturity regime, all maturity regimes are compared to the optimal producing range of vitrinite reflectance (Maturity Regimes 5 and 6); the maturity regimes are in order from best to worst hydrocarbon production. Regime 7 is slightly less productive than the optimal producing range of vitrinite reflectance because high thermal maturity has broken down methane gas into CO_2, reducing the production potential of the area. Also, thermal maturity levels exceeding 2.1 Ro (%) have shown the ability to reduce porosity and permeability within the rock itself (Tobey, 2007); this would reduce the deliverability of Regime 7. Regime 3 is not as productive as the optimal producing range of vitrinite reflectance because it is still in the wet gas generation window and thus likely does not have as good deliverability. Also, Regime 3 (located in a less mature area) may still have organic matter that has not completely converted to hydrocarbon. Regime 4 is not as productive as the optimal producing range of vitrinite reflectance due to some areas that occur within the condensate/wet gas generation window and due to methane depletion (an anomaly that will be discussed later in the chapter) affecting portions of the area. It is also possible that not all organic matter in Regime 4 has been converted into hydrocarbons; this is supported

by TOC maps having highest values in the western portion of the study area. Regimes 1 and 2 do not produce as well because they are in the oil and wet gas/condensate generation windows. Though the area may be hydrocarbon rich, liquid hydrocarbons are not easily delivered because of the very low permeability of the reservoir and the large size of hydrocarbon molecules. Also, the northern area of the basin is known to be less mature and therefore will only have oil-associated gases generated, not thermogenic gases derived from the cracking of oil (as does the southern area of the basin). Thermogenic gases create higher reservoir pressures and abundantly more gas, therefore increasing the amount of gas and the deliverability of the area.

Anomalies Found in Production and the Thermal Maturity

The HI and thermal maturity maps of the Barnett Shale illustrate areas where anomalous production occurs. These include: 1) areas of vitrinite reflectance greater than 1.4 Ro (%) that are producing condensate (liquid mixture of pentane and higher hydrocarbons) and wet gas (natural gas having significant amounts of heavier hydrocarbons in gasoline range) and 2) an area north of the Mineral Wells Fault in Barnett Shale zones 1 and 2 that is much more thermally mature than indicated by the thermal maturity map.

The first anomaly is illustrated in Figure 28 which compares cumulative oil production verses proxy vitrinite reflectance. This plot highlights a number of wells

that are producing liquid hydrocarbons even though they are in the Dry Gas Generation Window (1.4 to 2.1 Ro (%)) (Table 4) (shown by the red box labeled A).

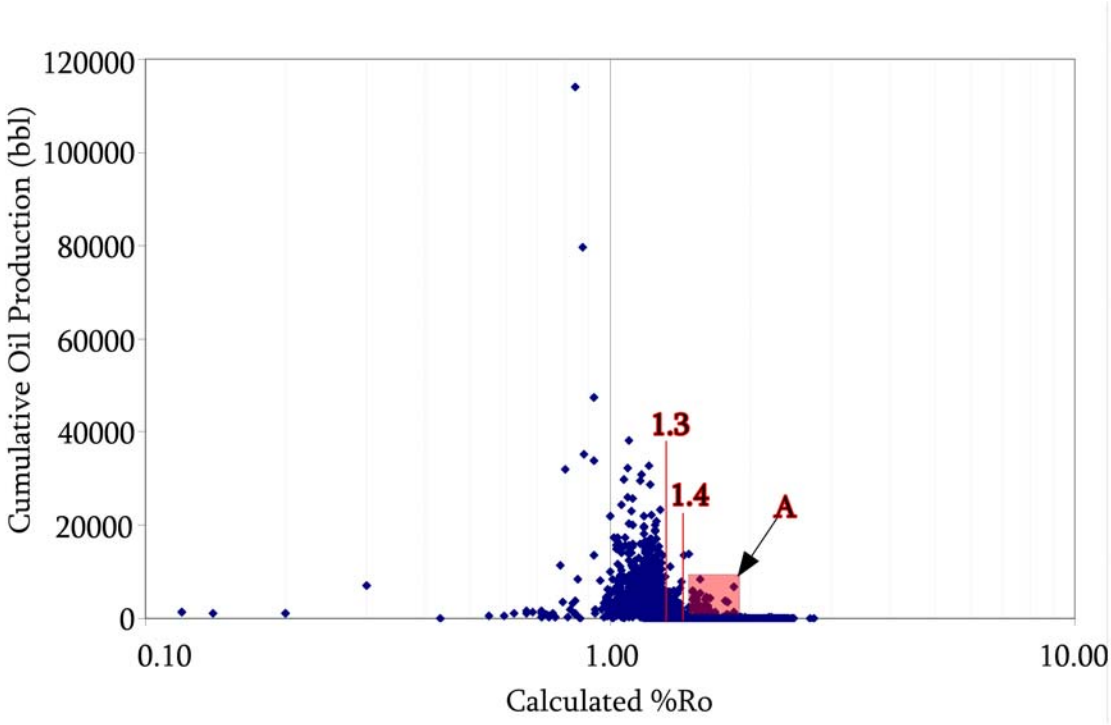

Figure 28: Cumulative oil and condensate production verses calculated vitrinite reflectance. A) Highlights the wells that have liquid production and a vitrinite reflectance higher than 1.4.

Figure 29 shows the irregular sample points on the thermal maturity map. All of these sample locations lie to the west or very close to the Viola Limestone erosional limit. To the west of the Viola Limestone erosional limit the Barnett Shale lies directly over the brine-bearing Ellenberger Formation. Figure 30 illustrates the relationship between the methane abundance in the hydrocarbon gases present and the corresponding vitrinite reflectance. It is known that as maturity increases, and the hydrocarbon molecules continue to break down into smaller molecules, the

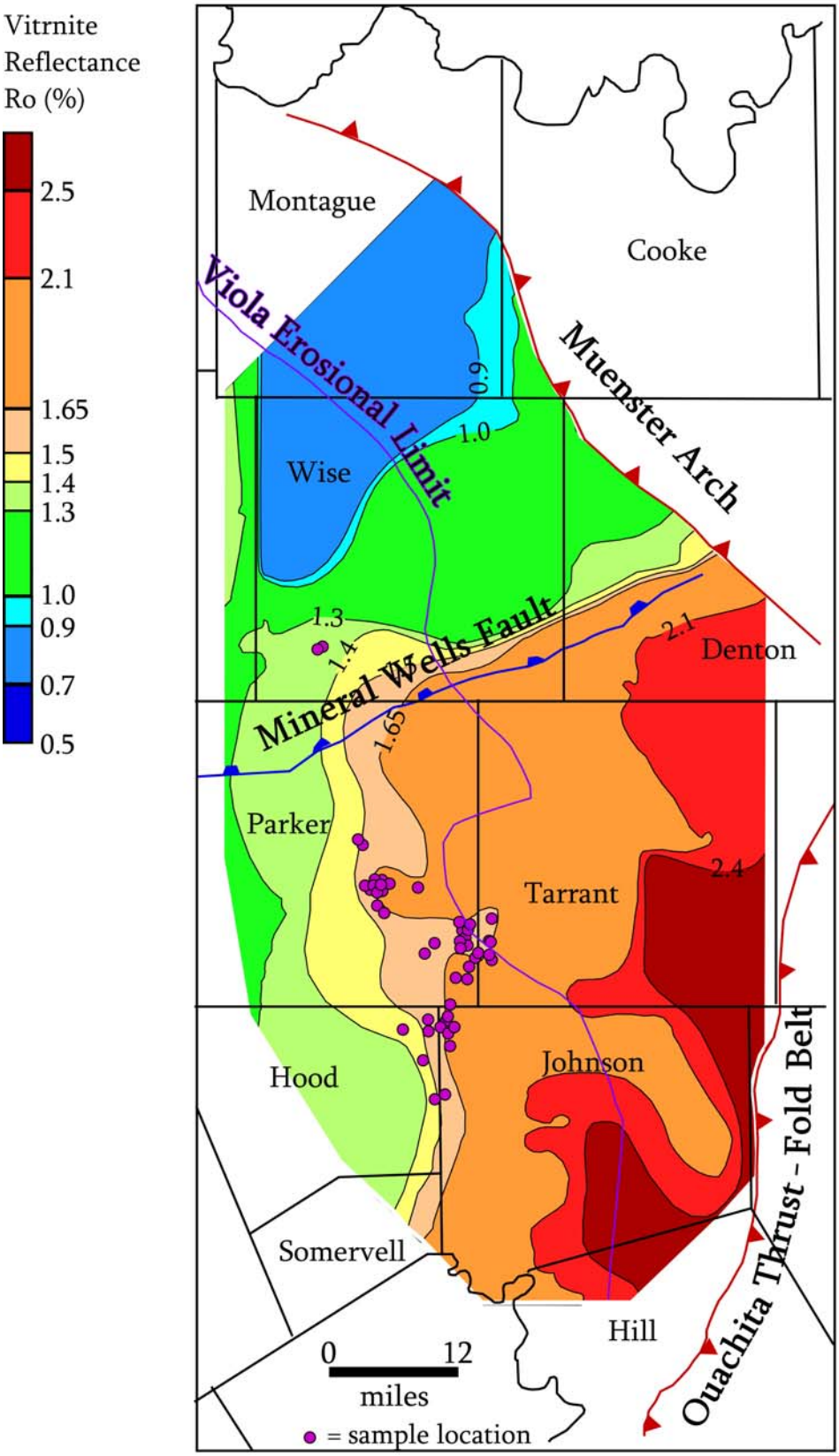

Figure 29: Thermal Maturity map showing wells that have a greater vitrinite reflectance than 1.4 Ro (%) and have produced oil and/or condensate.

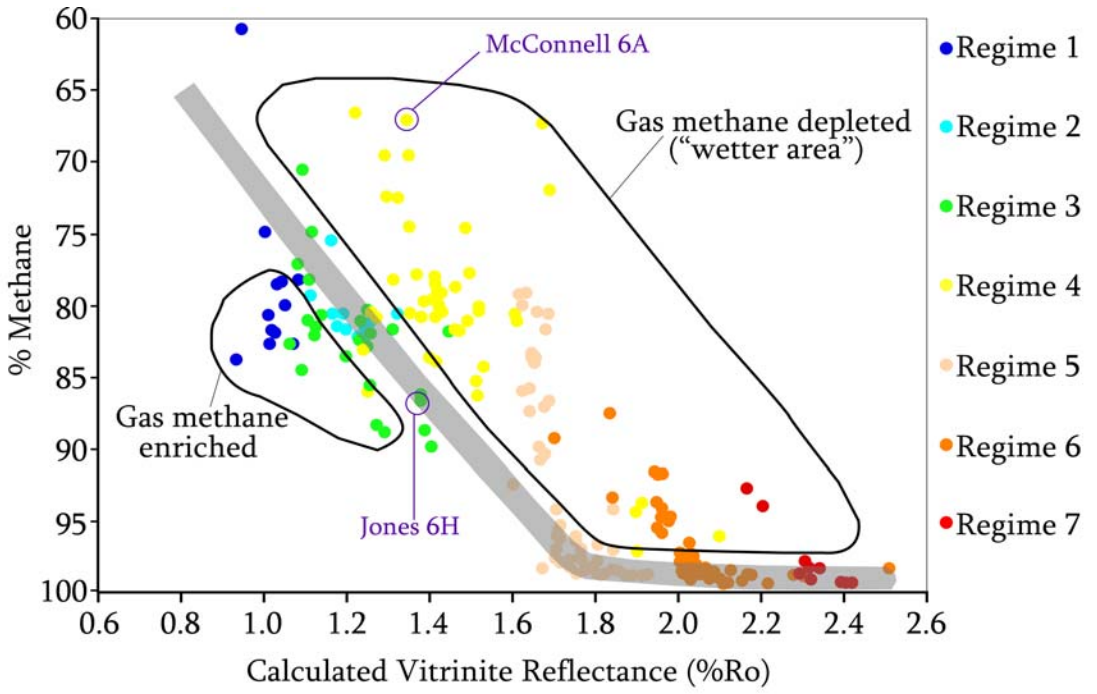

Figure 30: Relationship between methane abundance and proxy vitrinite reflectance in order to recognize gas wetness and anomalous areas. The wells Jones 6H and McConnell 6A will be used as an example to explain the effects of methane depletion. Jones 6H has not been effected by methane depletion whereas the McConnell 6A has been heavily effected by methane depletion.

methane abundance concurrently increases (conversation with Mark Tobey, July 2008; Barker and Pollock, 1984; Stahl, 1977). This relationship is illustrated by the gray shaded area shown in Figure 30. Areas outside the gray figure are anomalous. Any data falling above the shaded area are "wetter" than expected (meaning the ratio of wet gases to dry gases is higher than expected) and any data occurring below the shaded area are "drier" than expected (meaning the ratio of wet gases to dry gases is lower than expected).

It is probable that over geologic time the Ellenberger formation waters incorporated methane gas from the Barnett due to natural equilibrium processes.

Equilibrium is known as the condition in which all acting influences are balanced or canceled by equal opposing forces, resulting in a stable system (Drever, 1997). The most likely cause for the area being "wetter", as represented by the presence of condensate and wet gas production in a dry gas maturation window (1.4 – 2.1 Ro (%)) (Figures 28 and 30), is by methane depletion via water dissolution (conversation with Mark Tobey, July 2008). Dissolution is the process of attraction and association of solvent molecules with molecules or ions of a solute. As ions dissolve in a solvent they diffuse and become surrounded by solvent molecules (Drever, 1997). The most soluble molecules that will proceed through equilibrium processes first are the smallest molecules, as molecular size affects the solubility. The larger the molecule or the higher its molecular weight the less soluble the substance will be. This is because larger molecules are more difficult to surround with solvent molecules in order to solvate the substance (Martin, 1997). Therefore, the most soluble molecules are methane (CH_4) which are accordingly the first depleted from the Barnett Shale into the underlying Ellenberger formation waters.

Though it is probable that error within the vitrinite reflectance proxy has created the anomalous "wetter" area it is unlikely. Methane abundance data in Figure 30 illustrates that many of the samples do not follow the normal relationship between vitrinite reflectance and methane abundance; the vast majority of the samples that do not follow this relationship fall to the west of the Viola Limestone erosional limit. It is very unlikely that the vitrinite reflectance proxy, which has a regression coefficient

of 0.87, would cause such a large error margin [± 0.5 Ro (%)]. It is much more likely that the area west of the Viola Limestone erosional limit has been affected by methane depletion via water dissolution in the Ellenberger Formation.

When methane depletion is occurring it will affect an area negatively in the following ways: 1) lessen the reservoir pressure because of a reduction of methane gas in the reservoir, 2) reduce the total amount of hydrocarbons present and 3) possibly reduce the deliverability of the area because it reduces the amount of dry gasses present. For example, two wells from the methane isotope data were chosen at random, one that has undergone methane depletion via water dissolution and one of similar vitrinite reflectance that has not (Figure 30). The well McConnell 6A has undergone methane depletion. It has a proxy vitrinite reflectance of 1.34 Ro (%) which would normally correspond to a methane abundance of 85%, however, its methane abundance is 67%. The Estimated Ultimate Recovery (EUR) of the well is 0.18 bcfe (billion cubic feet equivalent) (EUR calculated by Leonard Biemer). If the area had not experienced methane depletion, at 85% methane abundance the EUR would be 0.23 bcfe ($\frac{67\%}{0.18 bcfe} = \frac{85\%}{x}, x = 0.23\ bcfe$). However, an EUR of 0.23 bcfe does not take into consideration the affects of a lower reservoir pressure, a reduction of the deliverability of the area or depletion of any other hydrocarbon molecules (eg, ethane, propane, butane and so on). The second well, Jones 6H, has not experienced methane depletion. It has a proxy vitrinite reflectance of 1.38% and

a methane abundance of 86%. The EUR of Jones 6H is 0.97 bcfe (EUR calculated by Leonard Biemer), approximately five times the EUR of McConnell 6A. Although many factors influence the production of a well, methane depletion via water dissolution has a strong negative affect on the hydrocarbon production potential of an area.

The second anomaly is seen in the HI maps within the upper 2 zones of the Barnett Shale. Zones 1 and 2 of the Barnett Shale, in the northern portion of the study area (Montague County, Cooke County, northeast Wise County and northwest Denton County), are much more thermally mature than Barnett Shale zones 3 through 8. The northern area is suggested to be less mature than the southern area of the basin by the thermal maturity map created in this study and by previous studies (Jarvie, 2004, Montgomery et al., 2005).

The anomaly occurring in the HI maps within zones 1 and 2 seems to be related to hydrothermal activity that has occured in the Marble Falls Limestone and along the Mineral Wells Fault system. This is probable because geothermal processes have been known to affect many other portions of the basin (Bowker, 2007, Pollastro et al., 2007). There is also data in Figure 30 that suggests geothermal processes have matured the northern areas of Barnett Shale zones 1 and 2. Many of the samples from Thermal Maturity Regimes 1, 2, and 3 show the area to be methane enriched or "dryer" than expected. It is possible that this area is methane enriched because

hydrothermal activity has thermally matured the northern strata of Barnett Shale in zones 1 and 2 only (the more mature the area the higher the methane abundance).

CHAPTER FOUR

Mineralogy

One of the attributes of the Barnett Shale that has an affect on production is mineralogical composition. The goal of mapping the mineralogy within the Barnett Shale is to find the relationships between mineral abundance and production. Whereas most shales are composed of greater than 60% clay minerals, the Barnett Shale has a mineral assemblage that is dominated by quartz and carbonate minerals (Jarvie et al., 2007). Quartz abundance has the potential to affect fracture stimulation. The higher the quartz abundance, the more brittle the shale should be because of a reduction in Poisson's ratio. Conversely, the higher the clay abundance the more ductile the shale. Higher clay content increases Poisson's ratio and reduces the proportion of artificial fractures.

The Barnett Shale also differs from many producing unconventional gas shales in that it does not have many natural fractures. Most natural fractures in the Barnett Shale are filled with calcite cement (Bowker, 2007). Therefore, the Barnett Shale should not be evaluated as a fractured-shale play but rather as a shale-that-can-be-fractured play. There are two main working hypotheses concerning how "healed" fractures (fratures that have been filled with a cement; eg. calcite cement) influence production: 1) healed fractures may enhance the effectiveness of artificial fracture

treatments by acting as zones of weakness that serve to deflect the growing induced fracture. The deflection of the growing induced fractures results in a larger fracture network that is created which provides more fractured surface area to produce from and results in more hydrocarbon production. 2) The presence of open natural fractures may inhibit the growth of artificial fractures because the healed fractures are zones of weakness that serve to eliminate the stress point at the tip of the fracture. If the stress point is eliminated the fractures do not continue to propagate throughout the rock and result in a smaller fracture network and less surface area to produce hydrocarbons from (Bowker, 2007).

Results

The average mineral abundances for all the samples of Barnett Shale analyzed in this study are: 35% clay minerals (illite and kaolinite), 32% quartz, 15% calcite, 10% dolomite/ankerite, 5% pyrite, 2% feldspar and 1% siderite. Mineral abundance for individual samples is presented in Appendix E.

Mineralogical Controls on Production

Quartz and carbonate abundance influence hydrocarbon production. Quartz abundance has a positive affect on production whereas calcite and dolomite abundance has a negative affect. Figures 31 and 32 illustrate these relationships. Figure 31 suggests a weak positive relationship between increasing quartz abundance

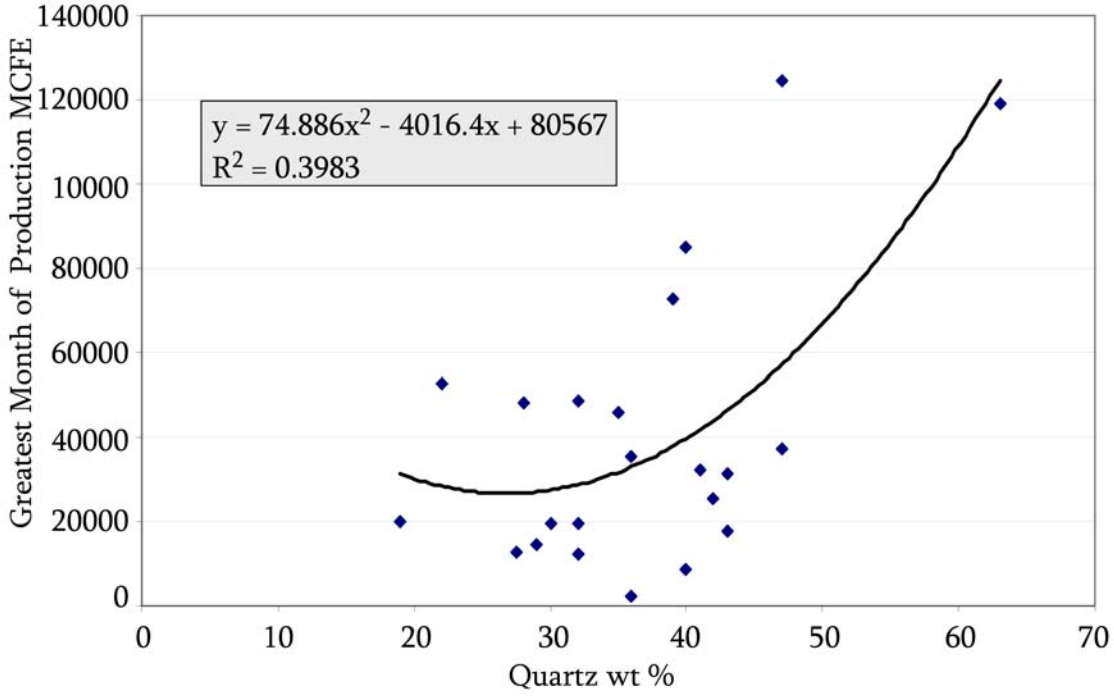

Figure 31: Semiquantitative quartz abundance of the production zone verses greatest month of production MCFE (thousand cubic feet equivalent, using 6:1 oil to gas ratio).

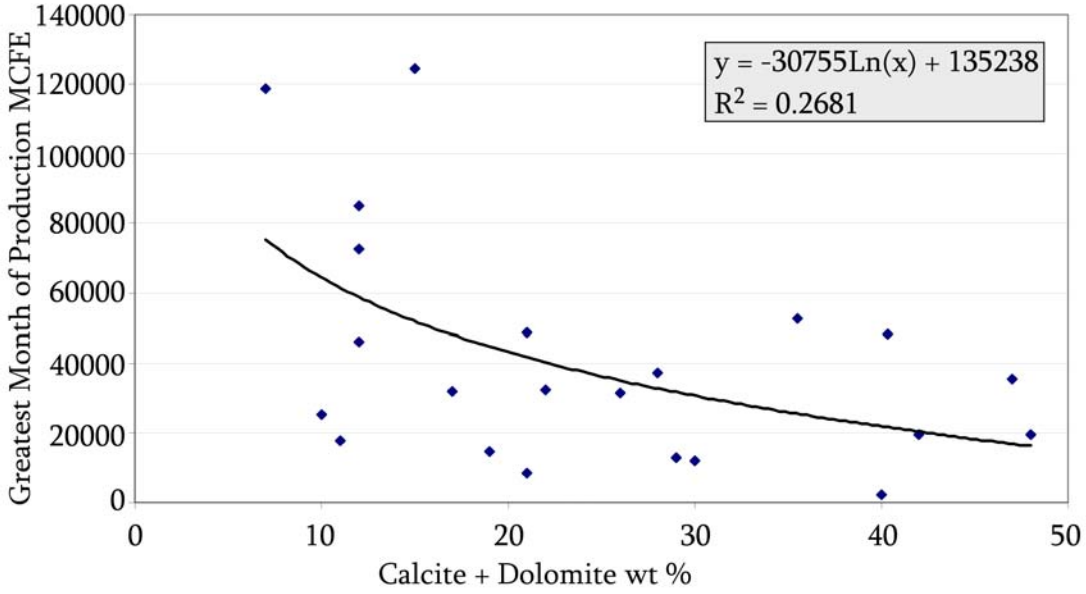

Figure 32: Semiquantitative calcite and dolomite abundance of the production zone verses greatest month of production MCFE (thousand cubic feet equivalent, using 6:1 oil to gas ratio).

and increasing production. There does not seem to be a noticeable increase in production unless quartz abundance is greater than 40%. Figure 32 illustrates the negative relationship between carbonate (calcite + dolomite) abundance and hydrocarbon production. Hydrocarbon production decreases when calcite and dolomite abundance exceeds 15%.

Mineralogy of the Barnett Shale Zones

Figure 33 illustrates how the average mineral abundance changes throughout the 8 zones of the Barnett Shale (Table 5). Many of the zones tend to have very similar mineral abundances. However, zones 1 and 8 have the highest abundance of calcite and dolomite. Zone seven has the greatest abundance of both clay minerals and pyrite. Zones 2 and 6 have the greatest abundance of quartz where as zone 8 has the least abundance of quartz.

Figures 34 and 35 show the overall distribution of quartz and carbonate minerals throughout the eight zones in the Barnett Shale. On average quartz is most abundant in zones 2, 4 and 6, with slightly lower concentrations in zones 1, 3 and 5, while zones 7 and 8 have the least abundance of quartz. Calcite and dolomite are most abundant in zones 1 and 8 followed by zones 5, 2, 3 and 4, and zones 6 and 7 have the least abundance of calcite and dolomite. Figures 36 through 39 show the spatial distribution of quartz abundance as well as calcite and dolomite abundance within all zones of the study area.

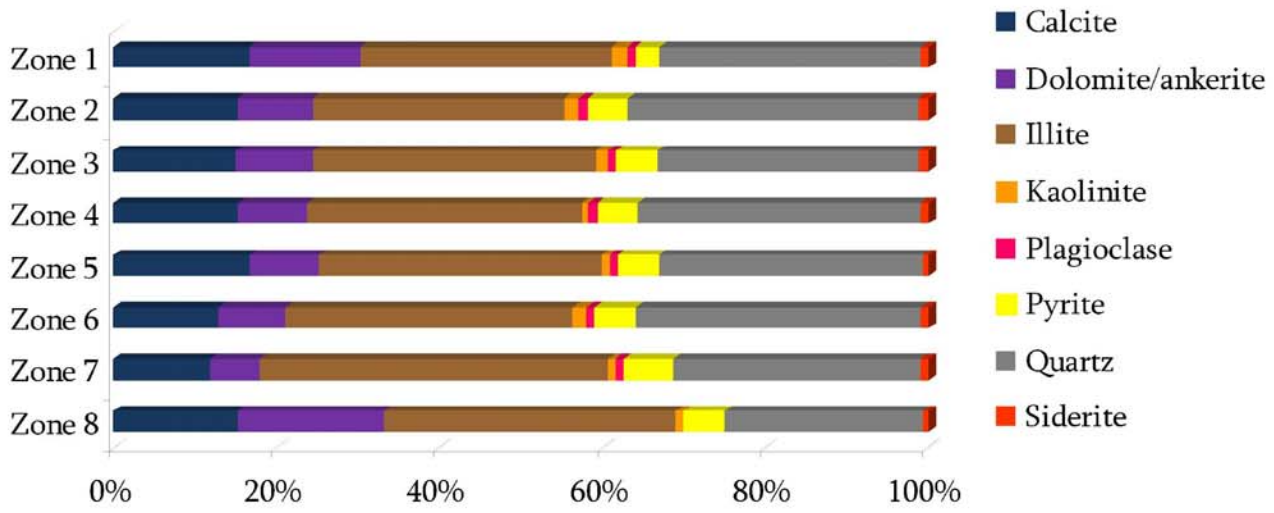

Figure 33: Stacked bar chart of the mineral abundance within Barnett Shale zones 1 through 8.

Table 5: Average mineral abundance, minimum mineral abundance and maximum mineral abundance in the 8 zones of the Barnett Shale (*Plag.= Plagioclase)

Zone	Eq.	Calcite	Dolomite	Illite	Kaolinite	*Plag.	Pyrite	Quartz	Siderite
Zone 1	Avg	17	13	31	2	1	3	32	1
	min	0	3	0	0	0	0	12	0
	max	58	39	58	11	4	9	58	6
Zone 2	Avg	15	9	31	2	1	5.0	35	1
	min	2	3	0	0	0	0	8	0
	max	63	22	45	13	6	9	66	3
Zone 3	Avg	15	9	34	2	1	4.8	32	1
	min	3	3	15	0	1	0	22	0
	max	43	32	50	10	4	8	45	3
Zone 4	Avg	15	8	33	1	1	5.4	34	1
	min	4	0	0	0	0	0	18	0
	max	48	24	47	7	5	13	64	4
Zone 5	Avg	17	8	34	1	1	4.7	32	1
	min	3	3	16	0	0	0	11	0
	max	61	19	58	7	7	7	49	3
Zone 6	Avg	13	8	35	2	1	4.6	35	1
	min	2	3	11	0	0	0	23	0
	max	44	22	57	10	4	8	52	3
Zone 7	Avg	12	6	42	1	1	5.7	30	1
	min	3	3	17	0	0	2	20	0
	max	40	10	60	5	5	8	46	3
Zone 8	Avg	15	18	35	1	0	4.8	24	1
	min	2	3	0	0	0	0	9	0
	max	61	69	57	4	3	9	45	3

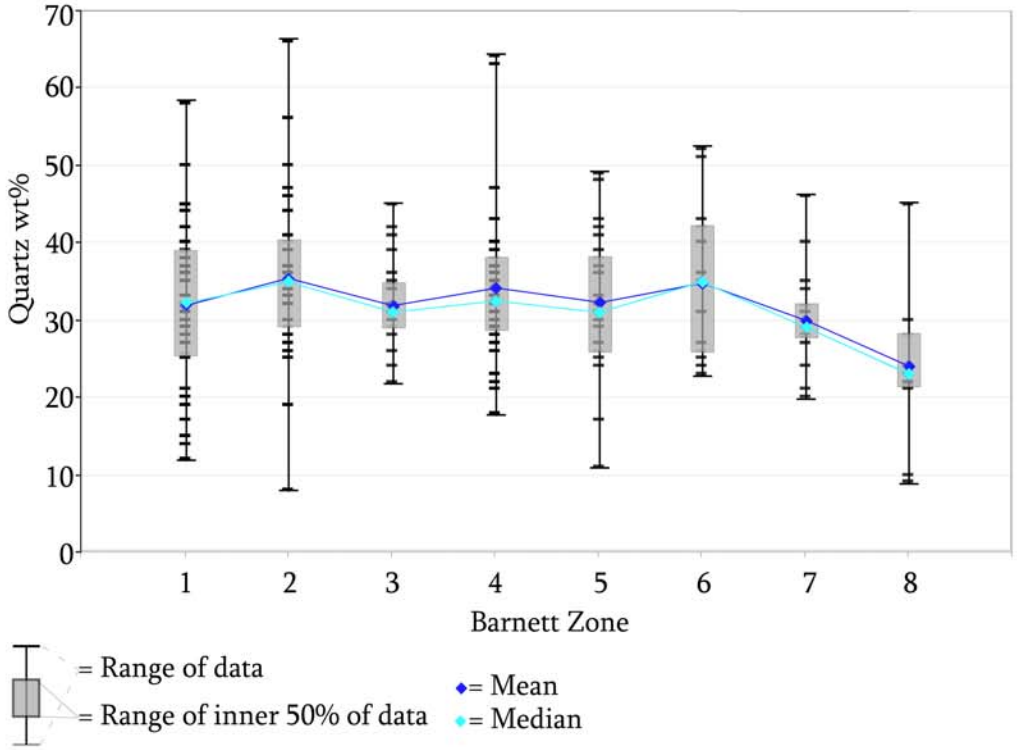

Figure 34: Box and whisker plots of qualitative quartz abundance by Barnett Shale zone.

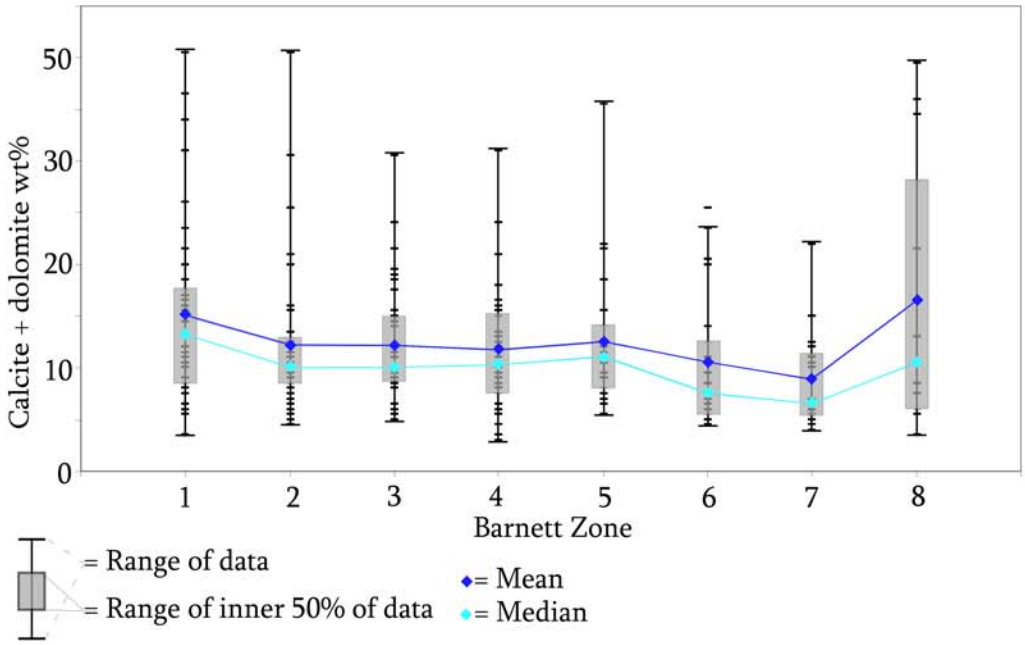

Figure 35: Box and whisker plots of qualitative calcite and dolomite abundance by Barnett Shale zone.

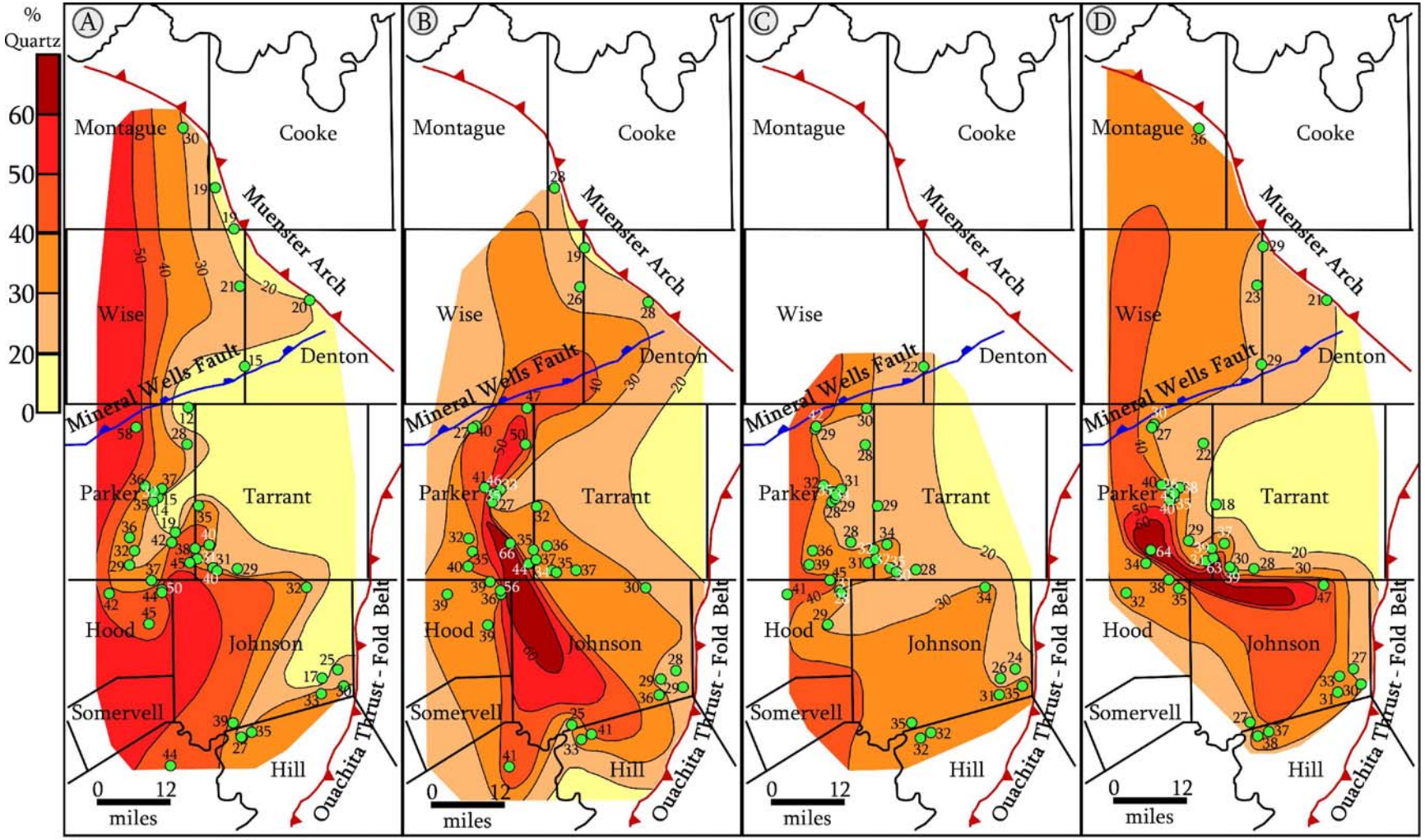

Figure 36: Quartz abundance maps. A) Barnett Shale zone 1, B) Barnett Shale zone 2, C) Barnett Shale zone 3, D) Barnett Shale zone 4.

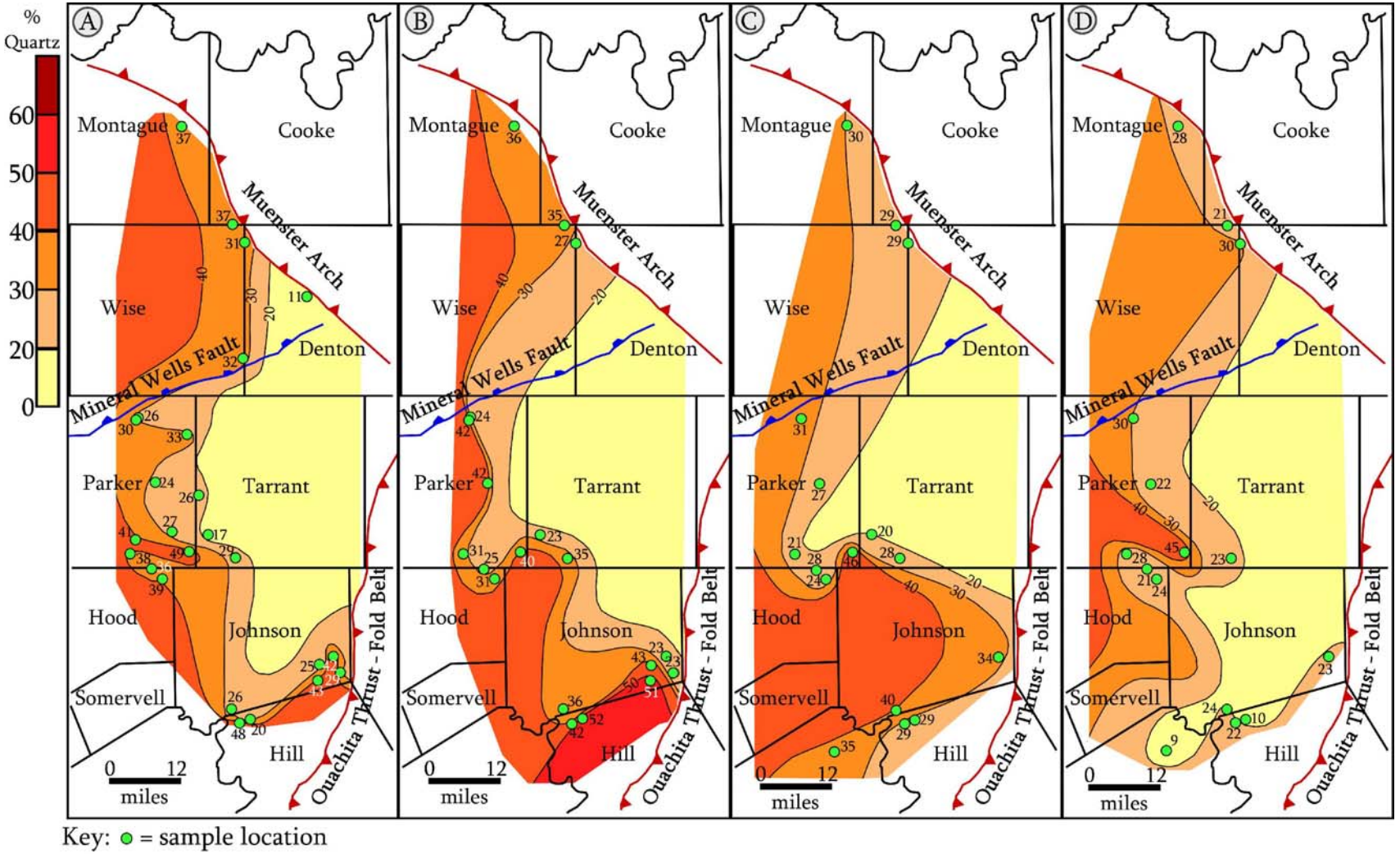

Figure 37: Quartz abundance maps. A) Barnett Shale zone 5, B) Barnett Shale zone 6, C) Barnett Shale zone 7, D) Barnett Shale zone 8.

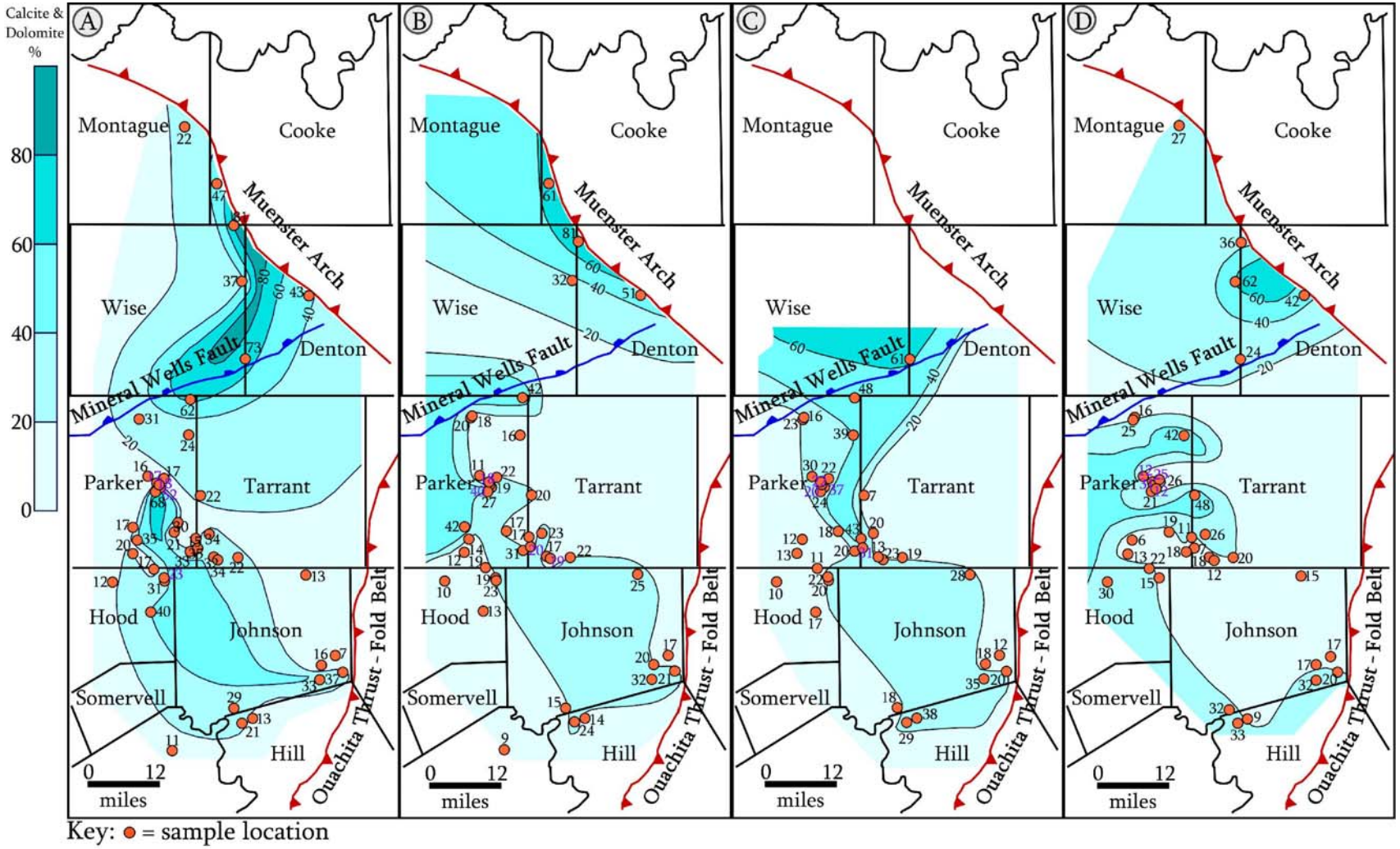

Figure 38: Calcite and dolomite abundance maps. A) Barnett Shale zone 1, B) Barnett Shale zone 2, C) Barnett Shale zone 3, D) Barnett Shale zone 4.

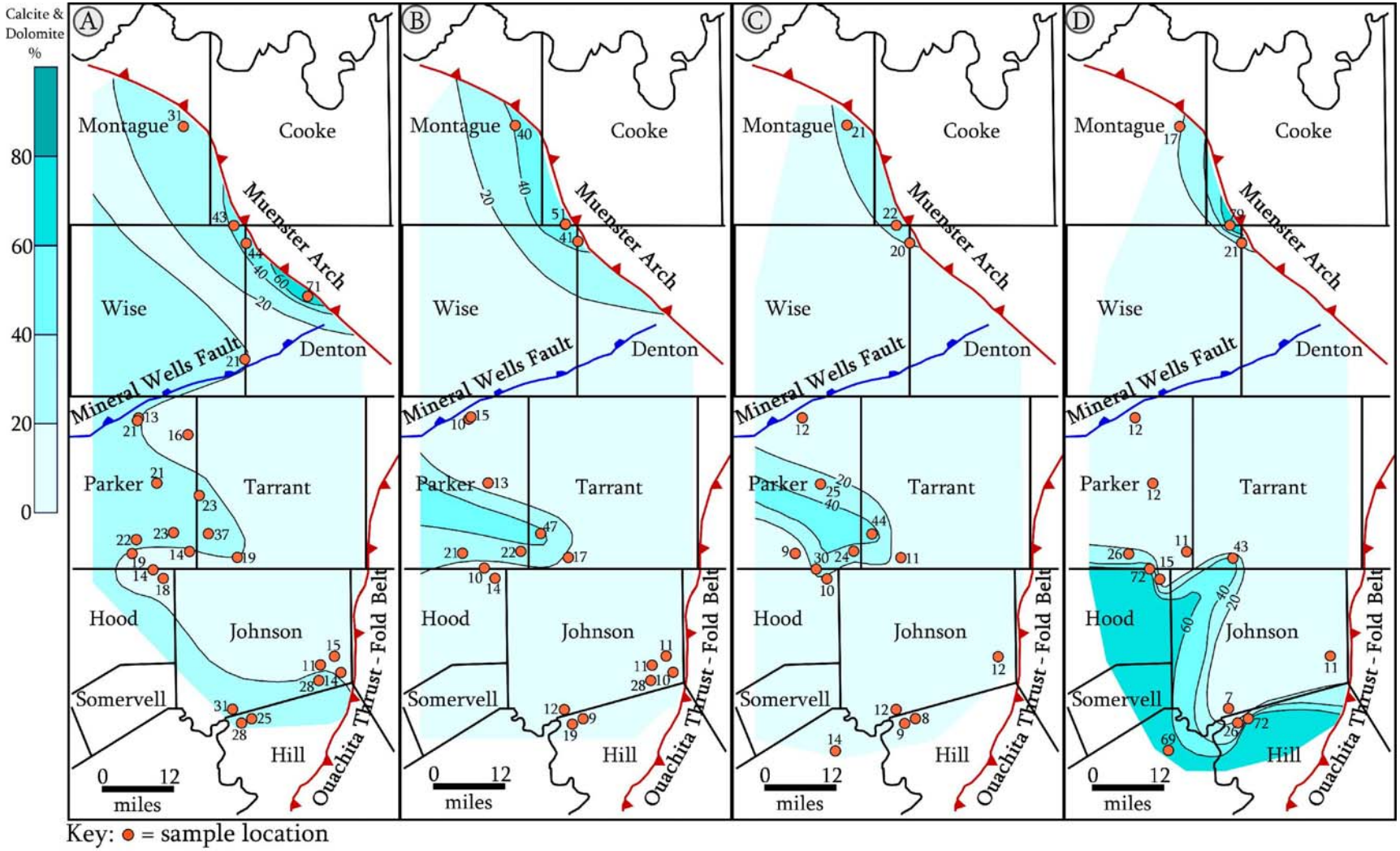

Figure 39: Calcite and dolomite abundance maps. A) Barnett Shale zone 5, B) Barnett Shale zone 6, C) Barnett Shale zone 7, D) Barnett Shale zone 8.

Barnett Shale zone 1. The greatest abundance of quartz in Barnett Shale zone 1 is located in the southwestern portion of the study area in north Parker, southeast Parker, southwest Tarrant, Hood and north Bosque Counties. The greatest abundance of calcite and dolomite is located in Cooke, northeast Wise, southeast Wise, west Denton, northeast Parker and southeast Parker Counties.

*Barnett Shale zone 2. T*he greatest abundance of quarts in Barnett Shale zone 2 is located in east Parker, east Hood and Bosque Counties. The greatest abundance of calcite and dolomite is located in Cooke, northeast Wise, northwest Denton, and central Parker.

Barnett Shale zone 3. The greatest abundance of quartz in Barnett Shale zone 3 is located in central Parker, and north Hood. The greatest abundance of calcite and dolomite is located in southeast Wise, east Parker, south Johnson and north Hill Counties.

Barnett Shale zone 4. The greatest abundance of quartz in Barnett Shale zone 4 is located in southeast Parker, southwest Tarrant, and north Johnson Counties. The greatest abundance of calcite and dolomite is located in northeast Wise, northwest Denton, areas of Parker, south Johnson and north Hill Counties.

Barnett Shale zone 5. The greatest abundance of quartz in Barnett Shale zone 1 is located in southeast Parker, north Hill and southeast Johnson Counties. The

greatest abundance of calcite and dolomite is located in northeast Wise, and north Denton Counties.

Barnett Shale zone 6. The greatest abundance of quartz in Barnett Shale zone 6 is located in central Parker, southeast Johnson, and northwest Hood Counties. The greatest abundance of calcite and dolomite is located in northeast Wise, and northwest Denton Counties.

Barnett Shale zone 7. The greatest abundance of quartz in Barnett Shale zone 7 is located in southeast Parker and southwest Johnson Counties. The greatest abundance of calcite and dolomite is located in southeast Parker, and southwest Tarrant Counties.

Barnett Shale zone 8. The greatest abundance of quartz in Barnett Shale zone 1 is located in the southeast Parker County. The greatest abundance of calcite and dolomite is located in northeast Wise, southwest Tarrant, Hood, north Bosque and north Hill Counties.

Discussion

The average mineral abundance in this study compares very well to the average mineral abundance reported by Loucks and Ruppel (2007). Loucks and Ruppel subdivide the Barnett into five sublithofacies through the use of XRD and polished thin sections prepared from core. The average mineralogy recorded in their

study is as follows: 34.3% quartz, 24.2% clay minerals, 16.1% calcite, 9.7% pyrite, 6.6% feldspar, 5.6% dolomite/ankerite, 3.3% phosphate, and 0.3% siderite. The largest difference between the data from Loucks and Ruppel (2007) and those presented here is clay abundance. This difference may be due to the types of material studied (core verses cuttings). Loucks and Ruppels' study utilized samples based on the five sublithofacies they identified in core. This study however utilized samples from drilling cuttings and therefore no preferential selection method was used. Additionally, the sublithofacies recurring most often (22 of the 35 samples) in Loucks and Ruppels' study is the siliceous mudstone which has the highest proportion of clays relative to the remaining sublithofacies. This study is likely a better representation of the overall mineral abundance in the Barnett Shale as it has seven times the number of samples.

Mineral abundance and spatial distribution may be influenced by many factors. Quartz abundance and distribution is dependent on the following: 1) locations of radiolarian "blooms" within the basin, 2) changing sedimentation rate within the basin, 3) the source of density flows and 4) the presence or absence of deep water contour currents. Variations in calcite and dolomite abundance and distribution are most likely caused by: 1) post depositional cementation originating from hydrothermal fluids, 2) detrital carbonate sediment plumes or density flows sourced from the Chappell Shelf and/or 3) the presence or absence of deep water contour currents.

The correlation found between production and quartz abundance supports the hypothesis regarding Poisson's ratio and the ability of the unit to artificially fracture. Figure 31 illustrates that production increases with greater than 40% quartz abundance. However, a negative relationship between increasing total clay abundance and decreasing production did not occur within the data to further support this hypothesis. Two possible explanations for a relationship not occuring are 1) the clay abundance does not affect the ability of the unit to artificially fracture to the degree of which quartz abundance does and 2) the clays present in the Barnett Shale are non-swelling clays which may have less of an influence on the rocks ductile qualities (therefore not affecting Poisson's ratio or the ability of the rock to artificially fracture).

The negative correlation between production and total carbonate abundance provides support that the presence of healed natural fractures inhibits the growth of stimulated fractures during completion processes. The general consensus is that the greatest calcite and dolomite concentrations in the Barnett Shale correspond to areas that have been remineralized by hydrothermal fluids; this is also supported by HI data and Methane abundance data from Chapter 3 of this study (Bethke and Marshak, 1990 found in Bowker, 2007; Hill et al., 2007). The areas with greatest calcite and dolomite concentration, shown in figures 35, 38 and 39, correlate to areas of known hydrothermal influence within the Marble Falls Limestone, the Ellenberger Formation and along the Mineral Wells Fault line. The areas of highest calcite and

dolomite concentration occur in Barnett Shale zones 1 and 8 which are adjacent to the hydrothermally effected Marble Falls Limestone and Ellenberger Formation. Also, all eight of the Barnett Shale zones have higher calcite and dolomite abundance west of the Viola Limestone erosional contact. Methane abundance data in Chapter 3 suggest that waters from the Ellenberger Formation are influencing the hydrocarbon production of the Barnett Shale where the Barnett Shale and the Ellenberger Formation are not separated by the Viola Limestone.

CHAPTER FIVE

Conclusions

1. The geochemical variables that have a relationship with production in the Barnett Shale are TOC, thermal maturity, quartz content and carbonate (calcite + dolomite) content. TOC contents greater than 2 wt.%, thermal maturity within the range 1.65 to 2.08 Ro (%), and quartz content greater than 40% correspond to higher gas production. Carbonate content greater than 15% corresponds to lower gas production.
2. The basin has experienced relatively uniform heat flow but has undergone differential burial and uplift. The degree of burial and corresponding vitrinite reflectance value relates directly to the quantity of hydrocarbon production.
3. An area of methane depletion via water dissolution is located west of the Viola Limestone erosional limit and corresponds to an overall reduction of hydrocarbon production in affected areas.
4. An area in Barnett Shale zones 1 and 2 in the northern portion of the basin is found to be affected by hydrothermal events and correlate to higher CO_2 production.

APPENDICES

APPENDIX A

Mineral Standard Data

Table A1: Standard sample JS-1

Minerals	%	mg	avg. peak area
Apatite	3.38	0.007	496
Calcite	0	0	0
Dolomite	0	0	0
Plagioclase	1.88	0.0039	1071
Pyrite	9.12	0.0189	2354
Quartz	6.37	0.0132	3073
Siderite	7.82	0.0162	12578
Illite	66.12	0.137	3867
Kaolinite	5.31	0.011	824
Smectite	0	0	0
Total	100	0.2072	

Table A2: Standard sample JS-2

Minerals	%	mg	avg. peak area
Apatite	3.84	0.008	132
Calcite	10.83	0.0226	4200
Dolomite	10.83	0.0226	2192
Plagioclase	3.98	0.0083	2066
Pyrite	5.80	0.0121	530
Quartz	17.16	0.0358	6718
Siderite	6.42	0.0134	3683
Illite	26.89	0.0561	1751
Kaolinite	14.24	0.0297	1395
Smectite	0	0	0
Total	100.00	0.2086	

Table A3: Standard sample JS-3

Minerals	%	mg	avg. peak area
Apatite	6.58	0.0136	272
Calcite	19.68	0.0407	8652
Dolomite	19.68	0.0407	3990
Plagioclase	6.33	0.0131	2220
Pyrite	4.26	0.0088	106
Quartz	3.48	0.0072	1718
Siderite	3.82	0.0079	2338
Illite	36.17	0.0748	1988
Kaolinite	0	0	0
Smectite	0	0	0
Total	100	0.2068	

Table A4: Standard sample JS-4

Minerals	%	mg	avg. peak area
Apatite	8.07	0.0164	204
Calcite	34.40	0.0699	16447
Dolomite	34.40	0.0699	6566
Plagioclase	7.97	0.0162	3691
Pyrite	2.12	0.0043	53
Quartz	0.94	0.0019	949
Siderite	2.21	0.0045	895
Illite	9.89	0.0201	467
Kaolinite	0	0	0
Smectite	0	0	0
Total	100	0.2032	

Table A5: Standard sample JS-5

Minerals	%	avg. peak area
Apatite	0	0
Calcite	50	44013
Dolomite	50	10572
Plagioclase	0	0
Pyrite	0	0
Quartz	0	0
Siderite	0	0
Illite	0	0
Kaolinite	0	0
Smectite	0	0
Total	100	

Table A6: Standard sample JS-6

Minerals	%	avg. peak area
Apatite	0	0
Calcite	0	0
Dolomite	0	0
Plagioclase	0	0
Pyrite	0	0
Quartz	40	16439
Siderite	0	0
Illite	0	0
Kaolinite	60	10804
Smectite	0	0
Total	100	

Table A7: Standard sample JS-7

Minerals	%	avg. peak area
Apatite	0	0
Calcite	90	48215
Dolomite	10	1892
Plagioclase	0	0
Pyrite	0	0
Quartz	0	0
Siderite	0	0
Illite	0	0
Kaolinite	0	0
Smectite	0	0
Total		

Table A8: Standard sample JS-8

Minerals	%	mg	avg. peak area
Apatite	0	0	0
Calcite	0	0	0
Dolomite	0	0	0
Plagioclase	0	0	0
Pyrite	0	0	0
Quartz	5.37	0.0108	1605
Siderite	0	0	0
Illite	0	0	0
Kaolinite	94.63	0.1905	13902
Smectite	0	0	0
Total	100	0.2013	

Table A9: Standard sample JS-9

Minerals	%	mg	avg. peak area
Apatite	0	0	0
Calcite	0	0	0
Dolomite	0	0	0
Plagioclase	0	0	0
Pyrite	0	0	0
Quartz	10.66	0.0215	6349
Siderite	0	0	0
Illite	0	0	0
Kaolinite	89.34	0.1802	14062
Smectite	0	0	0
Total	100	0.2017	

Table A10: Standard sample JS-10

Minerals	%	mg	avg. peak area
Apatite	0	0	0
Calcite	0	0	0
Dolomite	0	0	0
Plagioclase	0	0	0
Pyrite	0	0	0
Quartz	7.39	0.0149	2146
Siderite	0	0	0
Illite	0	0	0
Kaolinite	92.61	0.1867	14740
Smectite	0	0	0
Total	100	0.2016	

Table A11: Standard sample JS-11

Minerals	%	avg. peak area
Apatite	0	0
Calcite	0	0
Dolomite	0	0
Plagioclase	0	0
Pyrite	0	0
Quartz	8.82	4801
Siderite	0	0
Illite	91.18	6133
Kaolinite	0	0
Smectite	0	0
Total	100	

Table A12: Standard sample JS-12

Minerals	%	mg	avg. peak area
Apatite	50.10	0.1005	2002
Calcite	0	0	0
Dolomite	0	0	0
Plagioclase	0	0	0
Pyrite	0	0	0
Quartz	0	0	0
Siderite	0	0	0
Illite	0	0	0
Kaolinite	0	0	0
Smectite	49.90	0.1001	4949
Total	100.00	0.2006	

Table A13: Standard sample JS-13

Minerals	%	mg	avg. peak area
Apatite	15.75	0.0318	425
Calcite	0.00	0	0
Dolomite	0.00	0	0
Plagioclase	0.00	0	0
Pyrite	0.00	0	0
Quartz	0.00	0	0
Siderite	0.00	0	0
Illite	0.00	0	0
Kaolinite	0.00	0	0
Smectite	84.25	0.1701	*
Total	100.00	0.2019	

Table A14: Standard sample JS-14

Minerals	%	mg	avg. peak area
Apatite	5.45	0.0110	336
Calcite	0.00	0	0
Dolomite	0.00	0	0
Plagioclase	0.00	0	0
Pyrite	0.00	0	0
Quartz	0.00	0	0
Siderite	0.00	0	0
Illite	0.00	0	0
Kaolinite	0.00	0	0
Smectite	94.55	0.1910	*
Total	100.00	0.2020	

Table A15: Standard sample JS-15

Minerals	%	mg	avg. peak area
Apatite	2.04	0.0041	88
Calcite	0.00	0	0
Dolomite	0.00	0	0
Plagioclase	0.00	0	0
Pyrite	0.00	0	0
Quartz	0.00	0	0
Siderite	0.00	0	0
Illite	0.00	0	0
Kaolinite	0.00	0	0
Smectite	97.96	0.1969	*
Total	100.00	0.2010	

Table A16: 100 % Mineral Peak Heights

Sample	Mineral	Average peak area
JS-16	Apatite	6527
JS-17	Plagioclase	96493
JS-18	Pyrite	2227
JS-19	Quartz	62838
JS-20	Siderite	88040
JS-21	Kaolinite	12973
JS-22	Smectite	9969

Note: an * present means the mineral was used as a filler and not for calibration curves

APPENDIX B

Rock Eval Data

Table B1: Rock Eval data

Well API	Sample ID	Measured Depth (ft)	TOC %	HI
42035301100100	J1-1	6080	2.53	10
42035301100100	J1-2	6100	2.38	12
42035301100100	J1-7	6170	3.69	12
42035301100100	J1-8	6200	0.67	27
42097335490000	J2-1	7110	0.63	19
42097335490000	J2-2	7120	0.68	43
42121331370000	J3-2	7870	1.23	62
42121331370000	J3-4	8570	2.86	117
42121331370000	J3-5	8640	2.61	122
42121331370000	J3-6	8690	2.50	124
42121331370000	J3-7	8970	3.51	111
42121331370000	J3-8	9040	5.96	117
42121331590100	J4-1	8080	0.69	36
42121331590100	J4-2	8090	0.85	44
42121332170000	J5-1	7610	0.80	32
42121332170000	J5-2	7630	3.68	20
42121332170000	J5-3	7700	1.70	25
42121332170000	J5-4	8020	3.35	19
42121332170000	J5-5	8230	4.27	20
42217303780100	J7-1	7230	1.20	1
42217303780100	J7-2	7250	1.32	8
42217303780100	J7-3	7270	1.81	1
42217303780100	J7-4	7290	1.72	8
42217303780100	J7-5	7370	4.29	2
42217303780100	J7-6	7400	4.24	7
42217303780100	J7-7	7480	3.71	3

Table B1: Rock Eval data continued

Well API	Sample ID	Measured Depth (ft)	TOC %	HI
42217303780100	J7-8	7550	0.88	0
42217303950100	J8-1	6860	1.30	11
42217303950100	J8-2	6880	1.63	3
42217303950100	J8-3	6900	1.72	8
42217303950100	J8-4	6920	1.87	1
42217303950100	J8-5	6970	2.45	11
42217303950100	J8-6	7000	4.75	3
42217303950100	J8-7	7060	3.93	6
42217303950100	J8-8	7140	2.88	3
42221310680100	J9-1	6340	3.16	34
42221310680100	J9-2	6350	3.03	35
42221310680100	J9-3	6410	3.16	40
42221310680100	J9-4	6450	3.69	38
42221310680100	J9-5	6510	3.89	35
42221310680100	J9-7	6550	5.43	38
42221310680100	J9-8	6610	1.30	34
42221310700000	J10-1	5690	4.09	57
42221310700000	J10-2	5730	4.40	74
42221310700000	J10-3	5772	4.35	75
42221310700000	J10-4	5900	3.08	77
42221311050000	J11-1	6090	2.50	119
42221311050000	J11-2	6150	3.69	72
42221311050000	J11-3	6240	4.56	68
42221313510000	J13-1	6530	2.74	35
42221313510000	J13-2	6560	3.56	38
42221313510000	J13-3	6630	1.71	31
42221314600100	J14-1	6430	2.94	40
42221314600100	J14-2	6450	2.84	44
42221314600100	J14-3	6500	3.23	52
42221314600100	J14-4	6540	3.33	43

Table B1: Rock Eval data continued

Well API	Sample ID	Measured Depth (ft)	TOC %	HI
42221314600100	J14-5	6600	3.46	43
42221314600100	J14-6	6640	3.64	47
42221314600100	J14-7	6680	5.35	47
42221314600100	J14-8	6730	4.36	43
42251304840100	J15-1	6920	1.13	11
42251304840100	J15-2	6940	1.71	6
42251304840100	J15-3	6950	1.75	7
42251304840100	J15-4	7000	1.71	3
42251304840100	J15-5	7050	1.70	4
42251304840100	J15-6	7070	2.42	7
42251304840100	J15-7	7150	1.98	10
42251304840100	J15-8	7220	3.23	8
42251306370000	J16-1	8140	1.26	16
42251306370000	J16-2	8200	1.28	7
42251306370000	J16-3	8250	2.31	11
42251306370000	J16-4	8390	2.56	9
42251306370000	J16-5	8510	1.75	19
42251306370000	J16-6	8600	2.22	9
42251307310000	J17-1	8280	0.84	21
42251307310000	J17-2	8310	1.24	1
42251307310000	J17-3	8330	1.19	8
42251307310000	J17-4	8370	2.22	7
42251307310000	J17-5	8390	2.95	5
42251307310000	J17-6	8420	1.94	6
42251307310000	J17-7	8490	2.50	8
42251307310000	J17-8	8580	3.04	8
42251307330000	J18-1	8580	1.81	9
42251307330000	J18-2	8630	2.09	12
42251307330000	J18-3	8670	4.24	6
42251307330000	J18-4	8710	2.99	10

Table B1: Rock Eval data continued

Well API	Sample ID	Measured Depth (ft)	TOC %	HI
42251307330000	J18-5	8770	2.47	8
42251307330000	J18-6	8800	1.73	13
42251308510000	J19-1	8210	1.54	18
42251308510000	J19-2	8250	1.68	12
42251308510000	J19-3	8290	1.63	7
42251308510000	J19-4	8390	2.41	20
42251308510000	J19-5	8480	3.02	11
42251308510000	J19-6	8510	3.18	11
42251308760000	J20-1	7630	4.82	9
42251308760000	J20-2	7670	3.63	7
42251308760000	J20-3	7720	3.57	7
42251308760000	J20-4	7770	9.66	5
42337335070000	J22-1	6790	0.65	35
42337335070000	J22-6	7520	2.04	188
42337335070000	J22-8	8040	3.28	102
42367337990000	J24-1	6590	4.78	22
42367337990000	J24-3	6660	3.32	16
42367337990000	J24-4	6730	3.18	19
42367337990000	J24-5	6840	3.75	37
42367338250000	J25-1	6450	2.19	31
42367338510100	J26-1	6390	3.58	37
42367338510100	J26-2	6410	3.79	34
42367338510100	J26-3	6440	3.55	33
42367338510100	J26-4	6480	3.32	33
42367338510100	J26-5	6520	3.07	33
42367338510100	J26-6	6560	3.24	30
42367338510100	J26-7	6600	4.29	32
42367338510100	J26-8	6620	4.89	29
42367338570000	J27-1	6360	3.32	28
42367338570000	J27-2	6380	5.54	37

Table B1: Rock Eval data continued

Well API	Sample ID	Measured Depth (ft)	TOC %	HI
42367338570000	J27-3	6430	3.41	40
42367338570000	J27-4	6500	4.51	45
42367339260100	J28-1	6160	2.04	46
42367339260100	J28-2	6180	4.25	58
42367339260100	J28-3	6230	4.22	50
42367339260100	J28-4	6260	2.99	58
42367339260100	J28-5	6310	3.28	56
42367339260100	J28-6	6350	3.01	56
42367339260100	J28-7	6380	5.91	60
42367339260100	J28-8	6420	4.26	52
42367340100000	J29-1	6440	3.93	59
42367340100000	J29-2	6460	4.25	90
42367340100000	J29-3	6540	2.97	30
42367340100000	J29-4	6590	2.92	27
42367340100000	J29-5	6720	3.02	24
42367340100000	J29-6	6800	4.72	38
42367340630000	J30-1	6360	1.17	16
42367340630000	J30-2	6380	3.84	37
42367340630000	J30-3	6440	3.56	35
42367340700000	J31-1	6870	1.28	45
42367340700000	J31-2	6900	2.75	22
42367340700000	J31-3	6990	2.40	##
42367340950000	J32-1	6550	1.49	41
42367340950000	J32-2	6570	2.93	46
42367340950000	J32-3	6630	3.39	42
42367340950000	J32-4	6690	4.38	39
42367341310000	J33-1	6530	4.03	68
42367341310000	J33-2	6540	3.95	64
42367341310000	J33-3	6560	4.52	49
42367341610000	J35-1	6700	3.45	49

Table B1: Rock Eval data continued

Well API	Sample ID	Measured Depth (ft)	TOC %	HI
42367341610000	J35-2	6760	2.12	25
42367342610000	J36-1	6620	2.44	18
42367342610000	J36-2	6690	5.48	21
42367342610000	J36-3	6780	3.09	28
42367342610000	J36-4	6860	4.06	8
42367342610000	J36-5	8660	4.01	18
42367343250000	J37-1	6450	4.27	59
42367343250000	J37-2	6490	4.23	75
42367343250000	J37-3	6560	4.22	69
42367343250000	J37-4	6600	3.76	76
42367343250000	J37-5	6770	4.14	48
42367343600000	J38-1	6620	4.40	36
42367343600000	J38-2	6660	4.22	36
42367343600000	J38-3	6770	4.54	35
42367343600000	J38-4	6900	3.74	26
42367345380100	J39-2	6470	3.28	29
42367345380100	J39-3	6500	2.22	27
42367345380100	J39-4	6540	2.48	31
42367345380100	J39-5	6590	2.69	39
42367345380100	J39-6	6610	3.29	22
42367345380100	J39-7	6660	3.19	30
42367345380100	J39-8	6680	4.31	33
42439312750100	J42-2	6470	2.93	27
42439312750100	J42-3	6510	4.24	36
42439312750100	J42-4	6550	4.40	37
42439312750100	J42-5	6610	3.59	31
42439312750100	J42-6	6660	3.66	30
42439312750100	J42-8	6790	4.84	33
42439313620100	J43-1	6910	3.62	19
42439313620100	J43-2	6930	3.60	13

Table B1: Rock Eval data continued

Well API	Sample ID	Measured Depth (ft)	TOC %	HI
42439313620100	J43-3	6960	3.60	18
42439313620100	J43-4	6990	3.62	19
42439313620100	J43-5	7090	3.65	15
42439313620100	J43-6	7170	3.60	10
42439313620100	J43-8	7240	2.21	16
42439315510000	J44-1	6550	3.91	35
42439315510000	J44-2	6580	3.77	41
42439315510000	J44-3	6610	2.93	35
42439315510000	J44-4	6700	4.46	40
42439316840000	J45-1	6820	4.84	35
42439316840000	J45-2	6850	3.36	24
42439316840000	J45-3	6900	4.18	28
42439316840000	J45-4	7280	3.70	28
42439316870000	J46-2	6710	2.46	26
42439316870000	J46-3	6780	3.22	36
42439316870000	J46-4	6880	3.38	28
42439317030000	J47-1	6650	3.22	33
42439317030000	J47-2	6680	3.53	39
42439317030000	J47-3	6730	3.42	32
42439317030000	J47-4	6900	3.87	33
42439317980000	J48-1	6870	1.56	19
42439317980000	J48-2	6900	3.55	18
42439317980000	J48-3	6950	3.46	23
42439317980000	J48-4	7100	3.92	5
42439319920100	J49-1	6690	1.95	31
42439319920100	J49-2	6710	4.66	29
42439319920100	J49-3	6740	1.75	37
42439319920100	J49-4	6780	4.37	30
42439319920100	J49-5	6830	2.03	33
42439319920100	J49-6	6880	2.21	52

Table B1: Rock Eval data continued

Well API	Sample ID	Measured Depth (ft)	TOC %	HI
42439319920100	J49-7	6930	2.07	38
42439319920100	J49-8	6990	1.81	39
42497357250000	J52-1	7420	0.98	34
42497357250000	J52-2	7440	1.20	28
42497357250000	J52-3	8000	2.05	84
42497362610000	J53-2	7700	0.85	19
42497362610000	J53-4	8290	1.93	90
42497362610000	J53-5	8450	2.85	142
42497362610000	J53-6	8490	1.55	108
42497362610000	J53-7	8830	4.59	145
42497362610000	J53-8	8880	0.93	70

APPENDIX C

Vitrinite Reflectance Data

Table C1: Vitrinite reflectance data

Well Name	Sample	Depth (ft)	V.R. (%Ro)
J&L Partners 101H	J1-0A	-3674	1.44
J&L Partners 101H	J1-0B	-3974	1.48
J&L Partners 101H	J1-0C	-4364	1.53
J&L Partners 101H	J1-0D	-4754	1.56
J&L Partners 101H	J1-1A	-5244	1.64
J&L Partners 101H	J1-8A	-5364	1.65
J&L Partners 101H	J1-8B	-5504	1.64
J&L Partners 101H	J1-8C	-5654	1.66
Settle 1	J2-0A	-5905	0.83
Settle 1	J2-0B	-6035	0.88
Settle 1	J2-0C	-6185	0.84
Settle 1	J2-2A	-6265	0.88
McMurrey Ranch Unit A 7	J3-0A	-5849	NA
McMurrey Ranch Unit A 7	J3-0B	-6329	0.92
McMurrey Ranch Unit A 7	J3-2A	-6929	1.04
McMurrey Ranch Unit A 7	J3-4A	-7619	1.04
McMurrey Ranch Unit A 7	J3-5A	-7689	1.05
McMurrey Ranch Unit A 7	J3-6A	-7739	1.05
McMurrey Ranch Unit A 7	J3-8A	-8089	1.06
McMurrey Ranch Unit A 7	J3-8B	-8269	1.03
Baker Ranch 5H	J4-0A	-5299	1.08
Baker Ranch 5H	J4-0B	-6289	1.15
Baker Ranch 5H	J4-0C	-6799	1.20
Baker Ranch 5H	J4-2A	-7429	1.24
Baker Ranch 5H	J4-4A	-7669	1.28

Table C1: Vitrinite reflectance data continued

Well Name	Sample	Depth (ft)	V.R. (%Ro)
Baker Ranch 5H	J4-5A	-7799	1.27
Baker Ranch 5H	J4-5B	-8229	1.24
Baker Ranch 5H	J4-5C	-8599	1.25
Bullard 101H	J6-0A	-6264	2.18
Bullard 101H	J6-2A	-6714	2.37
Bullard 101H	J6-4A	-6774	2.35
Bullard 101H	J6-6A	-6864	2.37
Mills 5H	J10-0A	-4532	1.30
Mills 5H	J10-0B	-4721	1.28
Mills 5H	J10-4A	-4864	1.36
Mills 5H	J10-4B	-4866	1.39
Mills 5H	J10-4C	-4862	1.37
Mills 5H	J10-4D	-4864	1.37
Mills 5H	J10-4E	-4859	1.40
Mills 5H	J10-4F	-4864	1.37
Stewart Unit 1H	J11-0A	-4649	1.31
Stewart Unit 1H	J11-1A	-5084	1.35
Stewart Unit 1H	J11-3A	-5130	1.34
Stewart Unit 1H	J11-3B	-5155	1.35
Slocum 5H	J14-0A	-4941	1.42
Slocum 5H	J14-4A	-5481	1.46
Slocum 5H	J14-5A	-5541	1.50
Slocum 5H	J14-6A	-5581	1.47
Lore Levin 101H	J15-0A	-5113	2.10
Lore Levin 101H	J15-0B	-5413	2.13
Lore Levin 101H	J15-0C	-5713	2.25
Lore Levin 101H	J15-1A	-6143	2.34
Lore Levin 101H	J15-4A	-6223	2.35
Lore Levin 101H	J15-5A	-6273	2.34
Lore Levin 101H	J15-6A	-6293	2.33
Lore Levin 101H	J15-8A	-6443	2.33
Angus 1H	J16-1A	-7396	2.32
Angus 1H	J16-4A	-7526	2.32

Table C1: Vitrinite reflectance data continued

Well Name	Sample	Depth (ft)	V.R. (%Ro)
Angus 1H	J16-5A	-7564	2.34
Angus 1H	J16-6A	-7581	2.33
Kenneth Pipes 101H	J18-0A	-7730	2.31
Kenneth Pipes 101H	J18-0B	-7859	2.25
Kenneth Pipes 101H	J18-1A	-7974	2.34
Kenneth Pipes 101H	J18-2A	-8010	2.35
Kenneth Pipes 101H	J18-4A	-8063	2.34
Kenneth Pipes 101H	J18-5A	-8096	2.30
Kenneth Pipes 101H	J18-6A	-8104	2.31
Kenneth Pipes 101H	J18-6B	-8126	2.31
Classic Oaks Unit 1H	J20-0A	-5682	1.93
Classic Oaks Unit 1H	J20-0B	-6382	1.98
Classic Oaks Unit 1H	J20-4A	-6976	2.14
Classic Oaks Unit 1H	J20-4B	-6992	2.10
Nunneley A29 1	J22-0A	-5219	0.90
Nunneley A29 1	J22-1A	-5539	0.96
Nunneley A29 1	J22-1B	-5939	0.93
Nunneley A29 1	J22-4A	-6269	0.97
Nunneley A29 1	J22-5A	-6369	0.95
Nunneley A29 1	J22-6A	-6409	0.97
Nunneley A29 1	J22-8A	-6789	0.95
Nunneley A29 1	J22-8B	-6899	0.93
Willow Park Ranch 1H	J26-0A	-5125	1.57
Willow Park Ranch 1H	J26-0B	-5275	1.61
Willow Park Ranch 1H	J26-1A	-5425	1.64
Willow Park Ranch 1H	J26-4A	-5515	1.63
Willow Park Ranch 1H	J26-5A	-5555	1.60
Willow Park Ranch 1H	J26-6A	-5595	1.63
Willow Park Ranch 1H	J26-8A	-5655	1.64
Willow Park Ranch 1H	J26-8B	-5765	1.65
R Fellers 3H	J29-0A	-4492	1.38
R Fellers 3H	J29-0B	-4892	1.41
R Fellers 3H	J29-1A	-5337	1.49

Table C1: Vitrinite reflectance data continued

Well Name	Sample	Depth (ft)	V.R. (%Ro)
R Fellers 3H	J29-4A	-5464	1.49
R Fellers 3H	J29-5A	-5516	1.53
R Fellers 3H	J29-6A	-5532	1.51
R Fellers 3H	J29-6B	-5551	1.49
R Fellers 3H	J29-6C	-5546	1.50
Highland Ranch 2H	J33-1A	-5429	1.49
Highland Ranch 2H	J33-4A	-5488	1.50
Highland Ranch 2H	J33-5A	-5498	1.51
Highland Ranch 2H	J33-5B	-5524	1.49
Floyd Ranch 5H	J37-0A	-4314	1.48
Floyd Ranch 5H	J37-1A	-5230	1.52
Floyd Ranch 5H	J37-4A	-5323	1.53
Floyd Ranch 5H	J37-5A	-5368	1.49
Sewell Unit 2H	J43-0A	-4417	1.81
Sewell Unit 2H	J43-0B	-5317	1.97
Sewell Unit 2H	J43-1A	-6037	2.03
Sewell Unit 2H	J43-4A	-6117	2.06
Sewell Unit 2H	J43-5A	-6167	2.05
Sewell Unit 2H	J43-6A	-6217	2.05
Sewell Unit 2H	J43-8A	-6367	2.04
Sewell Unit 2H	J43-8B	-6457	NA
Virginia Richardson 1H	J44-0A	-5184	1.44
Virginia Richardson 1H	J44-1A	-5704	1.47
Virginia Richardson 1H	J44-3A	-5744	1.47
Virginia Richardson 1H	J44-4A	-5791	1.50
MT Cole 14AH	J52-0A	-5893	1.00
MT Cole 14AH	J52-0B	-6381	1.04
MT Cole 14AH	J52-1A	-6590	1.19
MT Cole 14AH	J52-2A	-6651	1.16
MT Cole 14AH	J52-2B	-6821	1.13
MT Cole 14AH	J52-2C	-7004	1.16
MT Cole 14AH	J52-4A	-7123	1.13
MT Cole 14AH	J52-4B	-7183	1.17

Table C1: Vitrinite reflectance data continued

Well Name	Sample	Depth (ft)	V.R. (%Ro)
Forman B 1	J53-4A	-7320	0.98
Forman B 1	J53-5A	-7480	0.99
Forman B 1	J53-6A	-7530	0.99
Forman B 1	J53-8A	-7910	0.96

APPENDIX D

Produced Methane Gas Isotope Data

Table D1: Produced Methane Gas Isotope Data

API	Mean Perf. (SSTVD ft.)	Calculated Maturation (%Ro)	$\delta^{13}C_{CH4}$	% Methane
42097335490000	-7245	1.00	-55.20	0.75
42337335210000	-7317	1.01	-55.20	0.83
42337335310000	-6691	0.95	-54.40	0.61
42097336020000	-7579	1.04	-53.70	0.78
42097336040000	-7379	1.02	-53.50	0.82
42097336520000	-7422	1.02	-53.40	0.82
42497348960000	-6561	0.93	-53.40	0.84
42097336050000	-7807	1.07	-53.00	0.83
42497347260000	-7486	1.03	-52.90	0.79
42121326520000	-7939	1.08	-51.60	0.78
42497347320000	-7652	1.05	-50.70	0.80
42497318690000	-1521	0.74	-45.69	0.57
42121309090000	-7306	1.01	-50.20	0.81
42121311850000	-7530	1.23	-49.90	0.82
42497359380000	-7218	1.19	-48.70	0.81
42121309570000	-7094	1.18	-48.40	0.81
42497345650000	-6984	1.16	-48.30	0.75
42121309290000	-7644	1.25	-47.60	0.82
42121317250000	-7760	1.26	-47.60	0.81
42497348190000	-7004	1.17	-47.60	0.81
42121320390000	-7615	1.24	-47.20	0.81
42121331590000	-8212	1.32	-46.89	0.81
42497346660000	-6740	1.26	-46.80	0.82
42121319610000	-7142	1.31	-46.70	0.82

Table D1: Produced Methane Gas Isotope Data Continued

API	Mean Perf. (SSTVD ft.)	Calculated Maturation (%Ro)	$\delta^{13}C_{CH4}$	% Methane
42497341590000	-6281	1.20	-46.70	0.84
42497346520000	-6654	1.24	-46.50	0.83
42497355850000	-6673	1.25	-46.50	0.80
42497340120000	-6526	1.23	-46.18	0.82
42497341790000	-6746	1.26	-46.10	0.86
42497332560000	-5333	1.47	-45.99	0.82
42497336360000	-5111	1.41	-45.72	0.84
42121326640000	-7666	1.38	-45.50	0.86
42121318270000	-7036	1.29	-44.80	0.89
42497343360000	-6892	1.28	-44.70	0.88
42121313790000	-7728	1.39	-44.40	0.89
42121324290000	-8143	1.45	-44.40	0.82
42121307670000	-7671	1.38	-44.18	0.87
42121313010000	-7845	1.40	-43.30	0.90
42497336510000	-5585	1.12	-46.77	0.75
42497329670000	-5638	1.12	-46.76	0.82
42497337710000	-5096	1.06	-46.61	0.83
42497337560000	-5512	1.11	-46.51	0.81
42497359270000	-7270	1.20	-49.40	0.82
42497340110000	-5761	1.14	-45.73	0.81
42497346320000	-6553	1.11	-48.70	0.79
42497354520000	-7027	1.17	-47.40	0.50
42497334370000	-5511	1.11	-47.33	0.78
42497338470000	-5677	1.13	-47.26	0.82
42497338150000	-5390	1.09	-47.20	0.70
42497340140000	-5260	1.08	-47.13	0.77
42497354070000	-6574	1.23	-47.10	0.81
42497342320000	-5365	1.09	-46.93	0.85
42237370730000	-4861	1.35	-46.97	0.69

Table D1: Produced Methane Gas Isotope Data Continued

API	Mean Perf. (SSTVD ft.)	Calculated Maturation (%Ro)	$\delta^{13}C_{CH4}$	% Methane
42237374510000	-4970	1.38	-46.93	0.81
42367342070000	-5167	1.43	-47.20	0.79
42221309890000	-4948	1.37	-47.30	0.78
42497333160000	-4441	1.25	-47.26	0.86
42237379770000	-4380	1.24	-47.39	0.83
42221311050000	-5146	1.42	-45.60	0.80
42221311560000	-5109	1.41	-45.60	0.81
42221311810000	-5156	1.43	-45.60	0.79
42221310700000	-4868	1.35	-45.80	0.75
42221311570000	-5429	1.50	-45.78	0.78
42221313120000	-5174	1.43	-46.00	0.80
42237379270000	-4740	1.32	-46.14	0.73
42497335350000	-4713	1.32	-46.13	0.78
42367338180000	-4486	1.26	-48.23	0.80
42367341900000	-5075	1.40	-47.80	0.80
42237381060000	-4610	1.29	-47.79	0.70
42237379720000	-4639	1.30	-47.61	0.72
42367344690000	-5008	1.39	-47.50	0.80
42367342570000	-4535	1.27	-46.90	0.81
42221310060000	-5119	1.42	-46.80	0.78
42237384390000	-4831	1.34	-46.31	0.67
42221309960000	-5115	1.41	-46.30	0.78
42367341580000	-5156	1.43	-45.50	0.80
42367341610000	-5304	1.46	-45.50	0.79
42497343480000	-4865	1.35	-45.27	0.81
42221312000000	-5069	1.40	-45.20	0.84
42251311140000	-5642	1.65	-40.90	0.83
42251312830000	-5384	1.62	-44.76	0.79
42367341310000	-5510	1.52	-44.70	0.80

Table D1: Produced Methane Gas Isotope Data Continued

API	Mean Perf. (SSTVD ft.)	Calculated Maturation (%Ro)	$\delta^{13}C_{CH4}$	% Methane
42251312840000	-5445	1.63	-44.59	0.79
42251312850000	-5462	1.63	-44.30	0.79
42251311170000	-5612	1.65	-44.25	0.83
42367343250000	-5389	1.49	-43.80	0.75
42251311180000	-5596	1.64	-43.66	0.84
42221310680000	-5299	1.46	-43.40	0.82
42221310020000	-5430	1.63	-43.00	0.86
42367339340000	-5414	1.62	-42.90	0.80
42367335220000	-5559	1.64	-42.70	0.86
42367338270000	-5694	1.66	-42.60	0.84
42367340100000	-5554	1.53	-42.40	0.84
42439315510000	-5811	1.61	-42.10	0.81
42367339210000	-5733	1.66	-41.70	0.80
42497335080000	-4310	1.22	-45.03	0.66
42497336640000	-5410	1.49	-44.84	0.81
42251302460000	-5560	1.64	-44.79	0.87
42367338570000	-5502	1.52	-44.60	0.80
42367336850000	-5488	1.51	-43.74	0.86
42367340950000	-5482	1.51	-43.70	0.85
42439319480000	-5957	1.69	-43.70	0.81
42439315550000	-5924	1.68	-43.50	0.82
42439318840000	-5839	1.61	-43.40	0.81
42497345090000	-6781	1.91	-43.30	0.94
42439319920000	-6035	1.67	-43.10	0.67
42251302140000	-4879	1.84	-42.80	0.88
42121311080000	-6736	1.90	-42.70	0.94
42439317860000	-6161	1.71	-42.70	0.96
42121309030000	-7296	2.10	-42.60	0.96
42367341570000	-5701	1.66	-42.60	0.84

Table D1: Produced Methane Gas Isotope Data Continued

API	Mean Perf. (SSTVD ft.)	Calculated Maturation (%Ro)	$\delta^{13}C_{CH4}$	% Methane
42439313390000	-6133	1.71	-42.50	0.96
42439313430000	-6002	1.69	-42.40	0.87
42439314740000	-6553	1.76	-42.40	0.96
42439312600000	-6652	1.77	-42.20	0.98
42439315460000	-6610	1.76	-42.20	0.97
42439311420000	-6219	1.72	-42.01	0.95
42497345410001	-6738	1.90	-42.00	0.97
42439314460000	-6413	1.74	-41.90	0.98
42121311760000	-7264	1.85	-41.82	0.94
42121322450000	-6955	1.81	-41.80	0.97
42439315180000	-6552	1.76	-41.80	0.97
42439309160000	-6919	1.80	-41.73	0.98
42439317500000	-6114	1.70	-41.70	0.98
42439317980000	-5904	1.68	-41.70	0.90
42439320720000	-5812	1.67	-41.70	0.91
42439320970000	-5772	1.67	-41.70	0.90
42251308130000	-5622	1.95	-41.69	0.92
42251305350000	-3924	1.70	-41.60	0.89
42251312870000	-5629	1.95	-41.58	0.92
42367336340000	-5219	1.60	-41.50	0.93
42367336820000	-6133	1.71	-41.50	0.94
42439301870000	-6212	1.72	-41.50	0.98
42439315140000	-6658	1.77	-41.50	0.98
42251305740000	-5678	1.95	-41.43	0.95
42367342610000	-5840	1.67	-41.40	0.98
42251310360000	-5701	1.96	-41.39	0.95
42121311010000	-7248	1.84	-41.30	0.97
42439313330000	-5889	1.68	-41.20	0.87
42439317260000	-6183	1.71	-41.20	0.96

Table D1: Produced Methane Gas Isotope Data Continued

API	Mean Perf. (SSTVD ft.)	Calculated Maturation (%Ro)	$\delta^{13}C_{CH4}$	% Methane
42439318170000	-6160	1.71	-41.17	0.97
42121307860000	-6934	1.80	-41.13	0.97
42251301850000	-5752	1.97	-41.10	0.92
42251304300000	-5647	1.95	-41.00	0.96
42439313140000	-7008	1.81	-40.94	0.99
42251312030000	-7488	1.87	-40.90	0.99
42251305060000	-5649	1.95	-40.88	0.94
42251305580000	-4946	1.85	-40.86	0.93
42251310330000	-5667	1.95	-40.85	0.94
42251310170000	-5859	1.98	-40.80	0.95
42251305770000	-6021	2.01	-40.75	0.98
42251301280000	-6241	2.04	-40.72	0.98
42251306240000	-5729	1.96	-40.70	0.94
42251306900000	-6062	2.01	-40.69	0.98
42439317300000	-6686	1.77	-40.63	0.98
42251302800000	-6041	2.01	-40.60	0.98
42251307010000	-7263	1.85	-40.60	0.98
42439310680000	-6413	1.74	-40.60	0.98
42251310610000	-7589	1.89	-40.59	0.99
42251305610000	-5840	1.98	-40.47	0.95
42251307430000	-6003	2.01	-40.45	0.97
42121320140000	-7343	1.86	-40.40	0.99
42251310100000	-6144	2.03	-40.40	0.97
42251311950000	-6173	2.03	-40.36	0.98
42121314740000	-6834	1.79	-40.20	0.98
42251306230000	-6948	1.81	-40.20	0.99
42439312610000	-7002	1.81	-40.20	0.99
42251308040000	-6094	2.02	-40.19	0.98
42251311780000	-7798	1.92	-40.19	0.99

Table D1: Produced Methane Gas Isotope Data Continued

API	Mean Perf. (SSTVD ft.)	Calculated Maturation (%Ro)	$\delta^{13}C_{CH4}$	% Methane
42121307170000	-6598	1.76	-40.10	0.98
42251312650000	-7875	1.93	-40.10	0.99
42251312690000	-6080	2.02	-40.10	0.98
42251302000000	-6181	2.03	-40.03	0.98
42439315300000	-6376	1.74	-40.00	0.98
42439310660000	-6185	1.71	-39.97	0.98
42439317510000	-6198	2.04	-39.90	0.98
42251303920000	-6531	1.75	-39.80	0.99
42251304170000	-6176	2.03	-39.80	0.98
42251310560000	-6533	2.09	-39.80	0.99
42251314150000	-7636	1.89	-39.80	0.99
42251311200000	-6004	2.01	-39.70	0.98
42439305480000	-6043	2.01	-39.60	0.98
42439321520000	-6482	2.08	-39.60	0.99
42251311560000	-6182	2.03	-39.50	0.98
42439308840000	-6032	2.01	-39.50	0.99
42439313620000	-6169	2.03	-39.50	0.97
42439319570100	-6532	2.09	-39.50	0.99
42251309510000	-6091	2.02	-39.40	0.98
42251302470000	-6005	2.01	-39.33	0.98
42251303380000	-5725	1.96	-39.30	0.96
42439302690000	-6319	2.06	-39.30	0.99
42439323310000	-6183	2.03	-39.30	0.99
42251311100000	-6171	2.03	-39.26	0.98
42439317230000	-6262	2.05	-36.70	0.98
42251312890000	-5631	2.17	-37.14	0.93
42251311400000	-6160	2.03	-38.74	0.98
42251310290000	-6219	2.04	-38.56	0.99
42251310660000	-6182	2.03	-38.47	0.98

Table D1: Produced Methane Gas Isotope Data Continued

API	Mean Perf. (SSTVD ft.)	Calculated Maturation (%Ro)	$\delta^{13}C_{CH5}$	% Methane
42251306350000	-6100	2.02	-38.30	0.98
42439315400000	-6300	2.05	-39.00	0.99
42251305920000	-5824	2.21	-37.32	0.94
42439303180000	-6443	2.08	-39.20	0.99
42439313890000	-7081	1.82	-40.20	0.99
42439318770000	-7028	2.17	-39.93	0.99
42251304470000	-7761	2.30	-39.40	0.99
42251308760000	-6999	2.17	-39.00	0.99
42439316400000	-6300	2.31	-35.70	0.99
42251306370000	-7624	2.28	-38.90	0.99
42121324020000	-6918	2.15	-38.80	0.99
42251312470000	-7018	2.17	-38.80	0.99
42439316690000	-6358	2.32	-36.41	0.98
42439315690000	-8852	2.51	-37.20	0.98
42439306290000	-6731	2.12	-38.80	0.99
42121324810000	-7289	2.22	-38.70	0.99
42439313940000	-6666	2.11	-38.20	0.99
42121315230000	-7073	2.18	-38.60	0.99
42251301780000	-6212	2.04	-40.27	0.99
42251301420000	-6244	2.04	-39.90	0.98
42251307560000	-6300	2.05	-39.85	0.99
42251310320000	-6414	2.07	-39.74	0.98
42251307180000	-6300	2.05	-39.60	0.99
42251301490000	-6753	2.13	-39.50	0.99
42251310310000	-6394	2.07	-38.34	0.98
42251303260000	-6446	2.08	-39.14	0.99
42217303760000	-6821	2.42	-38.00	0.99
42217303680000	-6758	2.41	-37.90	0.99
42251302600000	-6242	2.30	-37.86	0.99

Table D1: Produced Methane Gas Isotope Data Continued

API	Mean Perf. (SSTVD ft.)	Calculated Maturation (%Ro)	$\delta^{13}C_{CH6}$	% Methane
42217304090000	-6694	2.39	-37.20	0.99
42251304840000	-6363	2.32	-36.80	0.99
42217303780000	-6739	2.40	-36.50	1.00
42251311670000	-6206	2.04	-38.95	0.99
42217304080000	-6599	2.10	-38.91	0.99
42251306660000	-6388	2.07	-40.80	0.98
42251301560000	-6469	2.34	-35.90	0.98

APPENDIX E

Mineral Abundance Data

Table E1: Barnett Shale Zone 1 Mineral Composition

ID	UWI (APINum)	Calc.	Dol.	Illite	Kao.	Plag.	Pyrite	Qtz.	Sid.
J1	42035301100100	6	5	40	3	1	0	44	0
J2	42097335490000	34	13	29	3	1	0	19	0
J4	42121331590100	35	8	33	4	0	0	20	0
J5	42121332170000	46	27	11	0	0	0	15	0
J7	42217303780100	5	8	38	9	3	2	35	0
J8	42217303950100	6	15	44	8	0	0	27	0
J9	42221310680100	9	7	40	0	2	5	37	0
J10	42221310700000	6	6	36	0	1	6	42	2
J11	42221311050000	16	24	0	0	0	9	45	5
J13	42221313510000	20	11	18	0	0	7	44	0
J14	42221314600100	12	11	26	0	1	0	50	0
J15	42251304840100	10	19	26	4	2	0	39	0
J16	42251306370000	3	13	58	4	4	0	17	0
J17	42251307310000	0	7	54	8	0	0	25	6
J18	42251307330000	5	32	26	6	1	0	30	0
J19	42251308510000	7	26	16	11	2	5	33	0
J20	42251308760000	7	6	48	0	2	5	32	2
J22	42337335070000	18	3	37	7	2	0	30	2
J24	42367337990000	11	6	38	0	1	6	37	2
J25	42367338250000	19	11	45	0	1	5	19	0
J26	42367338510100	10	7	44	0	1	5	32	1
J27	42367338570000	12	4	40	0	1	5	36	2
J28	42367339260100	13	7	44	1	1	0	29	4
J29	42367340100000	21	10	0	0	1	9	58	0
J30	42367340630000	42	25	18	0	0	0	14	0
J45	42439316840000	11	12	33	0	1	6	35	1

Table E1: Barnett Shale Zone 1 Mineral Composition continued

ID	UWI (APINum)	Calc.	Dol.	Illite	Kao.	Plag.	Pyrite	Qtz.	Sid.
J46	42439316870000	14	19	24	0	4	7	31	1
J47	42439317030000	14	21	21	0	2	7	31	4
J48	42439317980000	9	24	18	0	2	6	40	0
J49	42439319920100	16	18	20	3	1	2	40	0
J52	42497357250000	27	11	38	4	1	0	21	0
J53	42497362610000	58	22	0	0	1	0	19	0

Table E2: Barnett Shale Zone 2 Mineral Composition

ID	UWI (APINum)	Calc.	Dol.	Illite	Kao.	Plag.	Pyrite	Qtz.	Sid.
J1	42035301100100	6	4	42	4	4	0	41	0
J2	42097335490000	43	18	8	3	0	0	28	0
J3	42121331370000	63	17	0	0	0	0	19	0
J4	42121331590100	40	12	21	0	0	0	28	0
J7	42217303780100	8	6	30	7	2	6	41	1
J8	42217303950100	9	16	38	4	1	0	33	0
J9	42221310680100	11	8	34	0	1	6	39	1
J10	42221310700000	6	4	41	0	2	7	39	1
J11	42221311050000	9	4	38	0	1	7	39	1
J13	42221313510000	6	16	15	0	0	5	56	2
J14	42221314600100	11	8	36	0	1	6	36	1
J15	42251304840100	9	6	45	6	3	4	25	2
J16	42251306370000	5	14	34	13	2	0	29	2
J17	42251307310000	2	15	38	9	4	1	28	0
J18	42251307330000	8	13	37	8	2	2	29	1
J19	42251308510000	11	21	19	6	2	6	36	0
J20	42251308760000	18	8	37	0	1	6	30	1
J24	42367337990000	15	7	34	0	3	6	33	2
J26	42367338510100	9	9	24	0	2	7	46	3
J27	42367338570000	7	3	39	0	1	6	41	3
J28	42367339260100	8	3	39	0	2	6	40	2
J29	42367340100000	14	6	32	0	0	7	40	0

Table E2: Barnett Shale Zone 2 Mineral Composition continued

ID	UWI (APINum)	Calc.	Dol.	Illite	Kao.	Plag.	Pyrite	Qtz.	Sid.
J30	42367340630000	18	10	37	0	1	6	27	2
J31	42367340700000	31	11	0	0	0	9	47	2
J32	42367340950000	30	10	40	0	1	9	8	3
J46	42439316870000	11	6	40	0	1	6	34	2
J47	42439317030000	10	9	35	0	1	6	37	2
J48	42439317980000	10	8	36	0	1	7	35	3
J49	42439319920100	11	12	34	1	2	2	36	1
J52	42497357250000	23	9	32	7	1	0	26	3

Table E3: Barnett Shale Zone 3 Mineral Composition

ID	UWI (APINum)	Calc.	Dol.	Illite	Kao.	Plag.	Pyrite	Qtz.	Sid.
J5	42121332170000	43	18	16	0	1	0	22	0
J7	42217303780100	6	32	21	4	1	5	32	0
J8	42217303950100	10	19	31	3	1	5	32	0
J9	42221310680100	8	3	34	0	2	6	45	1
J10	42221310700000	6	4	40	0	2	7	41	0
J11	42221311050000	11	6	43	0	1	6	29	3
J13	42221313510000	9	11	39	0	2	6	31	1
J14	42221314600100	18	4	41	0	1	6	28	0
J15	42251304840100	11	6	38	8	1	0	35	0
J16	42251306370000	8	10	49	6	1	0	26	0
J17	42251307310000	3	9	50	10	4	0	24	0
J18	42251307330000	9	11	32	2	3	6	35	1
J19	42251308510000	7	29	26	3	3	0	31	1
J20	42251308760000	16	12	29	0	2	7	34	0
J24	42367337990000	10	12	37	0	2	7	31	1
J26	42367338510100	16	6	34	0	2	8	35	0
J27	42367338570000	24	5	26	0	3	8	32	2
J28	42367339260100	9	4	37	0	2	6	39	2
J29	42367340100000	15	8	37	0	2	6	29	3
J30	42367340630000	19	5	36	0	3	6	28	3

Table E3: Barnett Shale Zone 3 Mineral Composition

ID	UWI (APINum)	Calc.	Dol.	Illite	Kao.	Plag.	Pyrite	Qtz.	Sid.
J31	42367340700000	33	14	15	4	1	3	30	0
J32	42367340950000	31	6	22	0	2	8	29	3
J33	42367341310000	14	5	43	0	1	7	28	2
J36	42367342610000	24	15	25	0	1	7	28	0
J37	42367343250000	4	9	44	0	4	3	36	1

Table E4: Barnett Shale Zone 4 Mineral Composition

ID	UWI (APINum)	Calc.	Dol.	Illite	Kao.	Plag.	Pyrite	Qtz.	Sid.
J3	42121331370000	23	13	27	0	0	7	29	2
J4	42121331590100	23	19	31	0	0	5	21	1
J5	42121332170000	15	9	39	0	0	6	29	1
J7	42217303780100	7	2	47	7	1	0	37	0
J8	42217303950100	9	24	19	4	3	2	38	0
J9	42221310680100	16	6	30	0	2	7	38	1
J10	42221310700000	25	5	27	0	3	8	32	1
J14	42221314600100	10	5	41	0	3	6	35	0
J15	42251304840100	11	22	35	3	2	0	27	0
J16	42251306370000	5	12	43	2	1	4	33	0
J17	42251307310000	7	10	42	7	2	5	27	1
J18	42251307330000	5	15	39	3	1	5	30	1
J19	42251308510000	14	18	34	2	2	0	31	0
J20	42251308760000	10	5	30	0	1	6	47	2
J22	42337335070000	20	7	34	1	1	0	36	1
J24	42367337990000	13	11	26	0	3	8	38	0
J26	42367338510100	25	6	32	0	2	7	26	2
J27	42367338570000	7	5	37	0	3	7	40	1
J28	42367339260100	7	6	44	0	2	6	34	1
J29	42367340100000	16	9	37	0	3	6	27	1
J30	42367340630000	14	8	28	0	3	7	40	1
J32	42367340950000	6	7	45	0	2	5	35	0
J33	42367341310000	15	4	42	0	2	7	29	2

Table E4: Barnett Shale Zone 4 Mineral Composition continued

ID	UWI (APINum)	Calc.	Dol.	Illite	Kao.	Plag.	Pyrite	Qtz.	Sid.
J36	42367342610000	42	0	21	0	2	8	22	4
J37	42367343250000	4	2	22	0	3	3	64	2
J52	42497357250000	48	14	0	0	2	13	23	0

Table E5: Barnett Shale Zone 5 Mineral Composition

ID	UWI (APINum)	Calc.	Dol.	Illite	Kao.	Plag.	Pyrite	Qtz.	Sid.
J3	42121331370000	30	14	17	0	1	6	31	0
J4	42121331590100	61	11	17	0	0	0	11	0
J5	42121332170000	13	8	37	0	3	6	32	1
J7	42217303780100	22	4	31	2	7	4	29	1
J8	42217303950100	11	16	23	0	2	0	48	0
J9	42221310680100	7	6	39	0	2	6	36	3
J14	42221314600100	13	5	33	0	3	7	39	0
J15	42251304840100	25	6	32	0	2	7	26	2
J16	42251306370000	4	7	58	6	0	0	25	0
J17	42251307310000	5	10	34	2	1	6	42	0
J18	42251307330000	3	11	45	7	0	4	29	1
J19	42251308510000	9	19	20	0	3	5	43	1
J22	42337335070000	24	7	31	1	0	0	37	0
J26	42367338510100	6	14	47	0	2	5	24	1
J28	42367339260100	12	7	32	1	3	7	38	0
J29	42367340100000	17	8	36	0	3	6	30	0
J33	42367341310000	16	7	38	0	3	6	27	2
J36	42367342610000	11	6	41	1	4	2	33	1
J37	42367343250000	15	7	28	0	1	7	41	0
J39	42367345380100	7	6	53	2	1	5	26	1
J42	42439312750100	8	6	28	0	1	6	49	1
J43	42439313620100	12	7	42	1	2	6	29	0
J45	42439316840000	16	7	40	0	3	6	26	1

Table E5: Barnett Shale Zone 5 Mineral Composition continued

ID	UWI (APINum)	Calc.	Dol.	Illite	Kao.	Plag.	Pyrite	Qtz.	Sid.
J49	42439319920100	33	3	40	0	1	7	17	0
J53	42497362610000	35	9	16	0	1	3	37	1

Table E6: Barnett Shale Zone 6 Mineral Composition

ID	UWI (APINum)	Calc.	Dol.	Illite	Kao.	Plag.	Pyrite	Qtz.	Sid.
J3	42121331370000	29	12	25	0	0	6	27	0
J7	42217303780100	3	5	29	3	1	5	52	1
J8	42217303950100	7	12	31	0	1	6	42	0
J9	42221310680100	5	4	57	0	4	2	25	1
J14	42221314600100	6	8	45	0	2	6	31	1
J15	42251304840100	5	7	39	7	1	5	36	0
J16	42251306370000	4	6	41	2	0	0	43	3
J17	42251307310000	3	9	55	6	1	4	23	1
J18	42251307330000	2	7	56	10	0	0	23	0
J19	42251308510000	6	22	14	1	2	2	51	1
J22	42337335070000	31	9	17	0	0	7	36	0
J26	42367338510100	6	7	33	0	3	7	42	2
J28	42367339260100	11	10	38	0	3	6	31	1
J29	42367340100000	5	5	38	0	3	7	42	1
J39	42367345380100	10	5	51	2	1	5	24	1
J42	42439312750100	14	8	27	0	4	8	40	0
J43	42439313620100	11	5	37	0	3	6	35	3
J49	42439319920100	44	3	22	1	1	3	23	1
J53	42497362610000	40	11	11	0	1	2	35	0

Table E7: Barnett Shale Zone 7 Mineral Composition

ID	UWI (APINum)	Calc.	Dol.	Illite	Kao.	Plag.	Pyrite	Qtz.	Sid.
J1	42035301100100	6	8	39	2	2	5	35	2
J3	42121331370000	11	8	45	0	1	6	29	0
J7	42217303780100	4	3	48	4	3	7	29	2
J8	42217303950100	4	5	52	3	4	2	29	1
J9	42221310680100	25	5	33	0	5	3	28	1
J14	42221314600100	6	5	56	0	3	5	24	1
J15	42251304840100	8	3	39	0	2	6	40	2
J17	42251307310000	3	9	42	5	2	5	34	0
J22	42337335070000	11	10	41	0	1	5	30	2
J26	42367338510100	18	7	39	0	2	7	27	0
J28	42367339260100	5	5	60	0	2	6	21	3
J39	42367345380100	7	5	47	1	1	6	31	1
J42	42439312750100	17	8	17	0	4	8	46	0
J43	42439313620100	4	8	50	0	4	6	28	1
J49	42439319920100	40	4	29	0	0	7	20	0
J53	42497362610000	19	3	40	0	1	7	29	1

Table E8: Barnett Shale Zone 8 Mineral Composition

ID	UWI (APINum)	Calc.	Dol.	Illite	Kao.	Plag.	Pyrite	Qtz.	Sid.
J1	42035301100100	4	65	19	3	0	0	9	0
J3	42121331370000	15	7	39	0	2	7	30	0
J7	42217303780100	2	69	13	1	0	3	10	1
J8	42217303950100	3	23	44	2	3	2	22	1
J9	42221310680100	42	30	0	0	0	7	21	0
J14	42221314600100	9	5	54	0	2	6	24	1
J15	42251304840100	3	4	57	4	2	5	24	1
J17	42251307310000	3	8	55	4	2	4	23	0
J22	42337335070000	11	6	49	0	0	5	28	0
J26	42367338510100	8	4	57	0	2	5	22	1
J28	42367339260100	12	15	36	0	3	7	28	0
J39	42367345380100	7	5	47	0	1	6	30	3
J42	42439312750100	8	3	36	0	2	6	45	0
J43	42439313620100	36	7	23	0	0	9	23	2
J53	42497362610000	61	18	0	0	0	0	21	0

REFRENCES

Ball, M. M., and W. J. Perry, 1996, Bend Arch – Fort Worth Basin Province, *in* Jarvie, D. M., R. J. Hill, T. E. Ruble and R. M. Pollastro, 2007, Unconventional Shale-Gas Systems: The Mississippian Barnett Shale of North-Central Texas as one Model for Thermogenic Shale-Gas Assessment: AAPG Bulletin, v. 91, no. 4, p. 475-499

Barker, J. F. and S. J. Pollock, 1984, The Geochemistry and Origin of Natural Gases in Southern Ontario: Bulletin of Canadian Petroleum Geology, v.32, no. 3, p. 313-326

Benthke, C. M. and S. Marshak, 1990, Brine Migrations across North America -The Plate Tectonics of Groundwater in Bowker, K. A., 2007, Barnett Shale Gas Production, Fort Worth Basin: Issues and Discussion: AAPG Bulletin, v. 91, no. 4, p. 523-533

Berner, U. and E. Faber, 1998, Matruity Related Mixing Model for Methane, Ethane, and Propane, Based on Carbon Isotopes *in* Rooney, M. A., G. E. Claypool and H. M. Chung, 1995, Modeling Thermogeinic Gas Generation Using Carbon Isotope Ratios of Natural Gas Hydrocarbons: Chemical Geology, 126:219-232

Berner, U., E. Faber and W. Stahl, 1992, Mathematical Simulation of the Carbon Isotopic Fractionation between Huminitic Coals and Related Methane: Chemical Geology, 94: 315-319

Blakey, R. C., 2006, Regional Paleogeographic Views of Earth History: Department of Geology, Northern Arizona University

Bowker, K. A., 2003, Recent Development of the Barnett Shale Play, Fort Worth Basin *in* Hill, R. J., E. Zhang, B. J. Katz and Y. Tang, 2007, Modeling of Gas Generation from the Barnett Shale, Fort Worth Basin, Texas: AAPG Bulletin, v. 91, no. 4, p. 501-521

Bowker, K. A., 2007, Barnett Shale Gas Production, Fort Worth Basin: Issues and Discussion: AAPG Bulletin, v. 91, no. 4, p. 523-533

Drever, James I., 1997, The Geochemistry of Natural Waters: Surface and Groundwater Environments Third Edition: University of Wyoming, p. 17-19, 107-125

EIA (Energy Information Administration), 2006, U.S. Crude Oil, Natural Gas, and Natural Gas Liquids Reserves 2005 annual report *in* Jarvie, D. M., R. J. Hill, T. E. Ruble and R. M. Pollastro, 2007, Unconventional Shale-Gas Systems: The Mississippian Barnett Shale of North-Central Texas as one Model for Thermogenic Shale-Gas Assessment: AAPG Bulletin, v. 91, no. 4, p. 475-499

Faber, E., 1987, Zur Isotopengeochemie Gasförmiger Kohlenwasserstoffe *in* Rooney, M. A., G. E. Claypool and H. M. Chung, 1995, Modeling Thermogeinic Gas Generation Using Carbon Isotope Ratios of Natural Gas Hydrocarbons: Chemical Geology, 126:219-232

Gas Research Institute, 1991, Formation Evaluation Technology for Production Inhancement: Log, Core Geochemical Analysis in Barnett Shale, Topical Report for Mitchell Energy Corp, Chicago, Illinois

Gutshick, R. and C. Sandberg, 1983, Mississippian Continental Margins on the Conterminous United States *in* Loucks, R. G. and S. C. Ruppel, 2007, Mississippian Barnett Shale: Lithofacies and Depositional Setting of a Deep-Water Shale-Gas Succession in the Fort Worth Basin, Texas: AAPG Bulletin, v. 91, no. 4, p. 579-601

Henk, F., 2005, Sublithofacies of the Barnett Formation from Outcrop to Subsurface (abs.) *in* Jarvie, D. M., R. J. Hill, T. E. Ruble and R. M. Pollastro, 2007, Unconventional Shale-Gas Systems: The Mississippian Barnett Shale of North-Central Texas as one Model for Thermogenic Shale-Gas Assessment: AAPG Bulletin, v. 91, no. 4, p. 475-499

Henk, F., J. T. Breyer, and D. M. Jarvie, 2000, Lithofacies, Petrography, and Geochemistry of the Barnett Shale in Conventional Core and Barnett Shale Outcrop Geochemistry (abs.) *in* Jarvie, D. M., R. J. Hill, T. E. Ruble and R. M. Pollastro, 2007, Unconventional Shale-Gas Systems: The Mississippian Barnett Shale of North-Central Texas as one Model for Thermogenic Shale-Gas Assessment: AAPG Bulletin, v. 91, no. 4, p. 475-499

Hickey, J. and F. Henk, 2006, Barnett Shale, Fort Worth Basin: Lithofacies and Implications (abs.) *in* Jarvie, D. M., R. J. Hill, T. E. Ruble and R. M. Pollastro, 2007, Unconventional Shale-Gas Systems: The Mississippian Barnett Shale of North-Central Texas as one Model for Thermogenic Shale-Gas Assessment: AAPG Bulletin, v. 91, no. 4, p. 475-499

Hickey, J. J. and B. Henk, 2007, Lithofacies Summary of the Mississippian Barnett Shale, Mitchell 2 T.P. Sims Well, Wise County, Texas: AAPG Bulletin, v. 91, no. 4, p. 437-443

Hill, R. J., D. M. Jarvie, J. Zumberge, M. Henry and R. M. Pollastro, 2007, Oil and Gas Geochemistry and Petroleum Systems of the Fort Worth Basin: AAPG Bulletin, v. 91, no. 4, p. 445-473

Hill, R. J., E. Zhang, B. J. Katz and Y. Tang, 2007, Modeling of Gas Generation from the Barnett Shale, Fort Worth Basin, Texas: AAPG Bulletin, v. 91, no. 4, p. 501-521

Hoefs, Jochen, 2004, Stable Isotope Geochemistry: Fifth Revised and Updated Edition. Institute of Geochemistry University of Göttingen, p. 44

Jarvie, D. M., 2004, Assessment of the Gas Potential and Yields from Shales: the Barnett Shale Model, Presentation to OGS-DOE Unconventional Energy Resources Confrence March 9-10, 2004

Jarvie, D. M., R. J. Hill, T. E. Ruble and R. M. Pollastro, 2007, Unconventional Shale-Gas Systems: The Mississippian Barnett Shale of North-Central Texas as one Model for Thermogenic Shale-Gas Assessment: AAPG Bulletin, v. 91, no. 4, p. 475-499

Klug, H. P., and L. E. Alexander, 1974, X-Ray Diffraction Proceedures: For Polycrystaline and Amorphous Materials (2d ed.): Wiley, New York

Kupecz, J. A. and L. S. Land, 1991, Late-Stage Dolomitization fo the Lower Ordovician Ellenberger Group, West Texas *in* Bowker, K. A., 2007, Barnett Shale Gas Production, Fort Worth Basin: Issues and Discussion: AAPG Bulletin, v. 91, no. 4, p. 523-533

Loucks, R. G. and S. C. Ruppel, 2007, Mississippian Barnett Shale: Lithofacies and Depositional Setting of a Deep-Water Shale-Gas Succession in the Fort Worth Basin, Texas: AAPG Bulletin, v. 91, no. 4, p. 579-601

Marble, W., 2004, Johnson County - Activity and Update (abs.) *in* Jarvie, D. M., R. J. Hill, T. E. Ruble and R. M. Pollastro, 2007, Unconventional Shale-Gas Systems: The Mississippian Barnett Shale of North-Central Texas as one Model for Thermogenic Shale-Gas Assessment: AAPG Bulletin, v. 91, no. 4, p. 475-499

Marble, W., 2006, Attributes of a Successful Unconventional Gas Project *in* Jarvie, D. M., R. J. Hill, T. E. Ruble and R. M. Pollastro, 2007, Unconventional Shale-Gas Systems: The Mississippian Barnett Shale of North-Central Texas as one Model for Thermogenic Shale-Gas Assessment: AAPG Bulletin, v. 91, no. 4, p. 475-499

Martin, Seth, 1997, Solubility of Solutes and Aqueous Solutions: Factors Affecting Solubility. Louisiana State University, Department of Chemistry

Montgomery, S. L., D. M. Jarvie, K. A. Bowker and R. M. Pollastro, 2005, Mississippian Barnett Shale, Fort Worth Basin, North-Central Texas: Gas-Shale Play with Multi-trillion Cubic Foot Potential: AAPG Bulletin, v. 89, no. 2, p. 155-175

Montgomery, S. L., D. M. Jarvie, K. A. Bowker and R. M. Pollastro, 2006, Mississippian Barnett Shale, Fort Worth Basin, North-Central Texas: Gas-Shale Play with Multi-trillion Cubic Foot Potential: Reply: AAPG Bulletin, v. 90, no. 6, p. 967-969

Papizis, P. K., 2005, Petrographic Characterization of the Barnett Shale, Fort Worth Basin, Texas *in* Loucks, R. G. and S. C. Ruppel, 2007, Mississippian Barnett Shale: Lithofacies and Depositional Setting of a Deep-Water Shale-Gas Succession in the Fort Worth Basin, Texas: AAPG Bulletin, v. 91, no. 4, p. 579-601

Pecharsky, V. K. and P. Y. Zavalij, 2005, Fundamentals of Powder Diffraction and Structural Characterization of Materials: Iowa State University and State University of New York at Binghamton, p. 138-146

Pollastro, R. M., D. M. Jarvie, R. J. Hill and C. W. Adams, 2007, Geologic Framework of the Mississippian Barnett Shale, Barnett-Paleozoic Total Petroleum System, Bend Arch-Fort Worth Basin, Texas: AAPG Bulletin, v. 91, no. 4, p. 405-436

Pollastro, R. M., R. J. Hill, D. M. Jarvie and C. Adams, 2004, Geologic and Orgainc Geochemical Framework of the Barnett Total Petroleum System, Bend Arch - Fort Worth Basin Province, Texas *in* Pollastro, R. M., D. M. Jarvie, R. J. Hill and C. W. Adams, 2007, Geologic Framework of the Mississippian Barnett Shale, Barnett-Paleozoic Total Petroleum System, Bend Arch-Fort Worth Basin, Texas: AAPG Bulletin, v. 91, no. 4, p. 405-436

Pollastro, R. M., R. J. Hill, D. M. Jarvie, and M. E. Henry, 2003, Assessing Undiscoverd Resources of the Barnett - Paleozoic Total Petroleum System, Bend Arch - Fort Worth Basin Province, Texas *in* Montgomery, S. L., D. M. Jarvie, K. A. Bowker and R. M. Pollastro, 2005, Mississippian Barnett Shale, Fort Worth Basin, North-Central Texas: Gas-Shale Play with Multi-trillion Cubic Foot Potential: AAPG Bulletin, v. 89, no. 2, p. 155-175

Rice, D. D., 1983, Relation of Natural Gas Composition to Thermal Maturity and Source Rock Type in San Juan Basin, Northwestern New Mexico and Southwestern Colorado: AAPG Bulletin, v. 67, no. 8, p. 1199-1218

Rooney, M. A., G. E. Claypool and H. M. Chung, 1995, Modeling Thermogeinic Gas Generation Using Carbon Isotope Ratios of Natural Gas Hydrocarbons: Chemical Geology, 126:219-232

Ross, C. A., and J. R. P. Ross, 1987, Late Paleozoic Sea Levels and Depositional Sequences *in* Loucks, R. G. and S. C. Ruppel, 2007, Mississippian Barnett Shale: Lithofacies and Depositional Setting of a Deep-Water Shale-Gas Succession in the Fort Worth Basin, Texas: AAPG Bulletin, v. 91, no. 4, p. 579-601

Schmoker, J. W., 1995, Method for Assessing Continuous-Type (unconventional) Hydrocarbon Accumulations *in* Jarvie, D. M., R. J. Hill, T. E. Ruble and R. M. Pollastro, 2007, Unconventional Shale-Gas Systems: The Mississippian Barnett Shale of North-Central Texas as one Model for Thermogenic Shale-Gas Assessment: AAPG Bulletin, v. 91, no. 4, p. 475-499

Senftle, J. T. and C. R. Landis, 1991, Vitrinite Reflectance as a Tool to Access Thermal Maturity (Ch 12): Arco Oil and Gas Company, Plano, Texas, U.S.A

Shen Ping, Shen Qixiang, Wang Xiaubin and Xu Yongchang, 1988, Characteristics of Isotope Composition of Gasiform Hydrocarbon and Identification of Coal-type Gas *in* Rooney, M. A., G. E. Claypool and H. M. Chung, 1995, Modeling Thermogeinic Gas Generation Using Carbon Isotope Ratios of Natural Gas Hydrocarbons: Chemical Geology, 126:219-232

Stahl, W. J. and B. D. Carey, 1975, Source-Rock Identification by Isotope Analyses of Natural Gases from Fields in the Val Verde and Delaware Basins, West Texas *in* Rooney, M. A., G. E. Claypool and H. M. Chung, 1995, Modeling Thermogeinic Gas Generation Using Carbon Isotope Ratios of Natural Gas Hydrocarbons: Chemical Geology, 126:219-232

Stahl, W. J., 1977, Carbon and Nitrogen Isotopes in Hydrocarbon Research and Exploration: Chemical Geology, 20:121-149

Stahl, W. J., H. Boigk and G. Wollanke, 1977, Carbon and Nitrogen Isotope Data of Upper Carboniferous and Rotliegend Natural Gases from North Germany and their Relationship to the Maturity of the Organic Source Material *in* Rooney, M. A., G. E. Claypool and H. M. Chung, 1995, Modeling Thermogeinic Gas Generation Using Carbon Isotope Ratios of Natural Gas Hydrocarbons: Chemical Geology, 126:219-232

Thompson, D. M., 1988, Fort Worth Basin *in* Montgomery, S. L., D. M. Jarvie, K. A. Bowker and R. M. Pollastro, 2005, Mississippian Barnett Shale, Fort Worth Basin, North-Central Texas: Gas-Shale Play with Multi-trillion Cubic Foot Potential: AAPG Bulletin, v. 89, no. 2, p. 155-175

Tobey, M. H., 2007, Exploration Organic Geochemistry for Shale Gas Resource Plays: Short Course Prepared for EnCana Oil and Gas (USA), Inc. May, 2007

Tobey, M. H., J. L. Edwards, S. J. Talbert, T. M. Smagala and J. M. Lisowski, 2009, A New Regional Thermal Maturity and Burial History of the Ft. Worth Basin Based on Gas Isotopic and Vitrinite Reflectance Studies (abs.): submitted to AAPG Bulletin Spring 2009

Walpner, J. L., 1982, Plate Tectonic Evolution of the Fort Worth Basin *in* Montgomery, S. L., D. M. Jarvie, K. A. Bowker and R. M. Pollastro, 2005, Mississippian Barnett Shale, Fort Worth Basin, North-Central Texas: Gas-Shale Play with Multi-trillion Cubic Foot Potential: AAPG Bulletin, v. 89, no. 2, p. 155-175

Zhao, H., N. B. Givens and B. Curtis, 2007, Thermal Maturity of the Barnett Shale Determined from Well-Log Analysis: AAPG Bulletin, v. 91, no. 4, p. 535-549